From Lab to Market: Evaluating Performance Metrics for Electrochemical Ammonia Synthesis versus Haber-Bosch

Master Thesis

Alexander C.E. Vlierboom

TUDelft

From Lab to Market: Evaluating Performance Metrics for Electrochemical Ammonia Synthesis versus Haber-Bosch

by

Alexander C.E. Vlierboom

IN PARTIAL FULFILMENT OF MASTER OF SCIENCE SUSTAINABLE ENERGY TECHNOLOGY
to be defended publicly on May 15, 2023 at 13:00

An electronic version of this thesis is available at `http://repository.tudelft.nl/`.

APRIL 30, 2023

FACULTY OF ELECTRICAL ENGINEERING, MATHEMATICS & COMPUTER SCIENCE

TUDelft Delft University of Technology

TU Delft

Delft
University of
Technology

Preface

This thesis represents the end of an incredibly enriching and fulfilling chapter of my academic journey at the Delft University of Technology. Throughout this period, I have not only acquired valuable knowledge and skills in my field of study, but I have also undergone significant personal growth, formed cherished friendships, and discovered my own sense of purpose. Over the past 9 months, I have dedicated my time into researching and writing this thesis, with the aim of shedding light on sustainable ammonia production methods. As I conclude this milestone with great satisfaction, I eagerly anticipate the next steps in my academic and professional career, and am excited to see what comes next.

I am especially grateful to my daily supervisor Boaz Izelaar, whose critical mind and endless discussions have challenged me to think critically and deeply about my research topic. His dedication to pushing me beyond my limits and making me walk through the learning experience of writing this thesis has been truly invaluable. Moreover, I would like to express my gratitude to my thesis committee for their support throughout this research journey. Their guidance, insightful feedback, and willingness to answer my questions and walk through my report have been essential in shaping the final outcome of this thesis. I would also like to extend my appreciation to the people from the Large-Scale Energy Storage department, whose critical questions and solutions have helped me overcome various challenges encountered during the course of my research. At last, I am grateful to my friends and family for their emotional support and encouragement throughout this thesis journey. Their constant understanding and kindness has been a driving force in these last couple of months.

Summary

Ammonia is a bulk commodity chemical known for its large production volumes (175 million tonnes per year) and use for the manufacturing of fertilisers. Ammonia equally has potential as a sustainable energy vector and hydrogen carrier. The industry standard for ammonia production is based on the fossil fuel based Haber-Bosch (HB) process, and is accompanied with high energy intensity and high carbon dioxide emissions (1.67 tonnes CO_2 per tonne NH_3). As of late, there has been scientific interest in developing sustainable ammonia synthesis alternatives, like the electrochemical nitrogen reduction reaction (e-NRR). This reaction requires renewable electricity, and abundant nitrogen and water as reactants to form ammonia.

The goal of this thesis is to investigate the techno-economic feasibility of conceptual process designs based on the e-NRR at different scales (91, 544 and 2055 t d^{-1}), which will be compared with the HB benchmark. Different electrolyzer types for the e-NRR are considered, including the alkaline electrolyzer (AEL), gas-diffusion electrode flow cell (GDE) and solid oxide electrolyzer (SOEL). The techno-economic feasibility analysis will also be used to determine the required electrolyzer performance criteria, such as current density (J), cell voltage (E_{total}) and faradaic efficiency (FE) to reach HB parity.

The conceptual process design primarily aims to include unit operations that are commercially available. The process models are designed in Excel and Aspen Plus V.12. Generally, the processes include air separation units (cryogenic air distillation or pressure swing adsorption) as a pre-treatment step, an electrolyzer, and an ammonia separation step based on distillation or condensation. The process assumptions were formulated in a base case scenario, which are used to calculate the process energy consumption and economic performance. Based on a sensitivity analysis with the base case as a reference, more optimistic assumptions were formulated and used for a second economic analysis.

The energy consumption of the e-NRR with the base case assumptions resulted in 69.0-92.8 GJ t^{-1}, which is considerably higher than the HB benchmark (27.4-31.8 GJ t^{-1}). This can be explained by the low energy efficiency (30-33%) of the electrolyzers in the base case scenario. The pre- and post-treatment significantly increased the process energy consumption too, and caused the high process energy consumption for the SOEL process. The economic analysis of the base case shows that the AEL process has the lowest levelized cost of ammonia (LCOA) at 2055 t d^{-1} (2,311 $ t^{-1}). Nonetheless, it is still 6 times higher than the HB benchmark (339 $ t^{-1}). The analysis indicates that small-scale production (91 t d^{-1}) is more suitable for e-NRR ammonia synthesis because HB is more capital intensive at smaller scales due to the economies of scale. Among the process designs, the GDE process is more favourable than the AEL. Because of the low nitrogen solubility in the AEL, the process requires an electrolyte recycle, which limits the overall process implementation and alters the electrochemical performance.

The sensitivity analysis shows that the electricity price has a significant effect on the LCOA. The cost of the electrolyzer does also significantly impact the LCOA. It was found that the LCOA of the GDE process can be reduced by 37.0%, when the electrolyzer costs are reduced from 11,868 to 2,970 $ m^{-2}. Electrolyzer performance parameters, such as the FE and J, yield optimal economic performance for minimum values of 60% and 0.3 A cm^{-2} respectively.

With the assumptions from the optimised case, the GDE process at 91 t d^{-1} has an LCOA of 398 $ t^{-1}. This is considerably lower than for HB (602 $ t^{-1}). This concludes that the e-NRR, under optimistic technical and economic conditions, is cost competitive at small scale operation. Nonetheless, the optimised assumptions (especially technical) were difficult to validate due to the infancy of the e-NRR technology. Therefore, reliable laboratory-scale demonstrations of the e-NRR at industrially relevant electrolyzer conditions are needed before an accurate assessment of the commercial feasibility can be made.

Keywords: electrochemical nitrogen reduction reaction, ammonia, techno-economic analysis, conceptual process design, energy analysis.

List of Figures

List of Tables

Acronyms and Symbols

Acronyms	
AEL	Alkaline Electrolyzer
AEM	Anion Exchange Membrane
AEMEL	Anion Exchange Membrane Electrolyzer
ASU	Air Separation Unit
ATR	Autothermal Reforming Reaction
BAT	Best Available Technology
CAD	Cryogenic Air Distillation
CAGR	Compound Annual Growth Rate
CAPEX	Capital Expenditure
CCS	Carbon Capture and Storage
CEPCI	Chemical Engineering Plant Cost Index
CF	Cash Flow
CFC	Cost for Consumables
CI	Capital Intensity
COP	Coefficient of Performance
CRF	Capital Recovery Factor
CRL	Commercial Readiness Level
DC	Direct Current
DCF	Discounted Cash Flow
DF	Distillate to Feed Ratio
DFT	Density Functional Theory
DoE	United States Department of Energy
EE	Energy Efficiency
e-HB	Electrified Haber Bosch Process
e-NRR	Electrochemical Nitrogen Reduction Reaction
FE	Faradaic Efficiency
GDE	Gas-Diffusion Electrode Electrolyzer
GHG	Greenhouse Gas
HB	Haber Bosch Process
HER	Hydrogen Evolution Reaction
HHV	Higher Heating Value
IEA	International Energy Agency
LCOA	Levilised Cost of Ammonia
LCOE	Levilised Cost of Electricity
LHV	Lower Heating Value
LOC	Feed stage location
N	Number of stages
NG	Natural Gas
NPV	Net Present Value
O&M	Operation and Maintenance
OER	Oxygen Evolution Reaction
OPEX	Operational Expenditure
OX	Oxidation
PCET	Proton-Coupled Electron Transfer

PEM   Proton Exchange Membrane
PEMEL   Proton Exchange Membrane Electrolyzer
PFD   Process Flow Diagram
PSA   Pressure Swing Adsorption
RED   Reduction
REFUEL   Renewable Energy to Fuels through Utilization of Energy-dense Liquids
RES   Renewable Energy Sources
RR   Reflux Ratio
SF   Split fraction
SHE   Standard Hydrogen Electrode
SMR   Steam Methane Reforming
SMR-HB   Haber-Bosch Process with Steam Methane Reforming
SOEL   Solid Oxide Electrolyzer
STP   Standard Temperature and Pressure (25 °C and 1.01325 bar)
TFB   Tripple-Phase Boundary
TFC   Total Final CAPEX
WGS   Water-Gas Shift Reaction
YSZ   Yttrium Stabilised Zirconia

	Symbols	
a	Activity	$mol \cdot l^{-1}$
A	Pre-exponential factor	[-]
A_e	Electrode area	cm^2
c	Concentration	$mol\%$
C	Cost	\$
E_{cell}^0	Standard reversible cell potential at STP	V
E_{ox}^0	Standard oxidation potential at STP	V_{SHE}
E_{red}^0	Standard reduction potential at STP	V_{SHE}
E_{tn}^0	Thermo-neutral potentia at STP	V
E_a	Activation Energy	$kJ \cdot mol^{-1}$
E_{total}	Total cell potential	V
F	Faraday constant	$C \cdot mol^{-1}$
f_i	Correction factor for component i	[-]
G	Gibbs free energy	$kJ \cdot mol^{-1}$
H	Enthalpy	$kJ \cdot mol^{-1}$
h_f^0	Enthalpy of formation	$kJ \cdot mol^{-1}$
I	Current	A
i	Nominal yearly interest rate	$\%$
J	Current density	$A \cdot cm^{-2}$
J_{lim}	Limiting current density	$A \cdot cm^{-2}$
k	Rate constant	$mol \cdot s^{-1}$
M_i	Scaling factor for component i	[-]
n	Lifetime	$Years$
P_i	Power consumption for component i	W
P	Pressure	bar
Q	Thermal energy	$kJ \cdot mol^{-1}$
R	Universal gas constant	$J \cdot molK^{-1}$
r_i	Reaction rate of component i	$mol \cdot s^{-1}$
S	Entropy	$J \cdot molK^{-1}$
s_f^0	Entropy of formation	$J \cdot mol^{-1} \cdot K^{-1}$
T	Temperature	$°C$
W	Work	W
χ_{N_2}	Single pass conversion	$mol\%$
Y_i	Recovery of component i	$mol\%$
y_i	Purity of component i	$mol\%$
z	Number of electrons	[-]
η_{act}	Activation overpotential	V
η_{Ohm}	Ohmic overpotential	V
$\eta_{Ohm,el}$	Ohmic electrolyte overpotential	V
$\eta_{Ohm,mem}$	Ohmic membrane overpotential	V
η_{con}	Concentration overpotential	V

Contents

Chapter 1

Introduction

1 Background

With a production volume of approximately 175 million metric tonnes per year [1], ammonia (NH_3) is one of the highest produced chemicals in the world. Nitrogen is a vital element for life due to its involvement in nucleotide and amino acid synthesis. Although N_2 is abundant in the earth's atmosphere, only a limited number of microorganisms are able to convert it into usable forms (NH_3 and NO_x^-) through the natural nitrogen cycle. As a result, the large-scale development of artificial methods for capturing and converting N_2 to NH_3 or NO_x^- have significantly contributed to the intensification of agriculture and increasing crop yields. Nowadays, around 80% of NH_3 is used as the nitrogen source for artificial fertilisers like ammonium nitrate (NH_4NO_3) and urea ($CO(NH_2)_2$) [2]. This has played a crucial role in supporting the world's growing population, and this technology is therefore considered one of the most significant inventions of the 20th century [3, 4, 5].

Moreover, recent publications agree that NH_3 has great potential as an emission-free energy storage medium and hydrogen (H_2) carrier [3, 5, 6, 7]. NH_3 has a practical energy density of 18.7 GJ t^{-1} at lower heating value (LHV) and can be liquefied by pressurisation up to 10 bar or cooling to -33 °C [8]. As a liquid, NH_3 has a volumetric energy density of 15.6 GJ m^{-3} at LHV, which is considerably larger than the volumetric energy density of liquid or pressurised H_2 (9.1 GJ m^{-3} for liquid and 5.6 GJ m^{-3} at 700 bar respectively [9]). This, combined with the vast experience and existence of distribution infrastructure make NH_3 easier and cheaper to transport than H_2 [10]. Additionally, the higher energy density makes NH_3 more suitable for mobile applications than H_2, for instance as a replacement for bunker oil in the maritime industry [11]. These characteristics have sparked interest by governmental agencies, such as the International Energy Agency (IEA) [12] and the United States Department of Energy REFUEL program [13], where NH_3 is included in their decarbonisation strategies. It is expected that the NH_3 market will grow from 53 billion $ to 81 billion $ by 2025 (Compound Annual Growth Rate (CAGR) of 5.6%) [14].

NH_3 is currently synthesised via the century-old Haber-Bosch process (HB), which consumes natural gas (NG) as a feedstock. This process is energy-intensive, and produces carbon dioxide (CO_2) indirectly as a by-product at a globally significant scale (1.67 tonnes CO_2 per tonne NH_3 [15]). Evidently, anthropogenic greenhouse gas (GHG) emissions, including CO_2, have resulted in an average global rise of temperatures in the past decades [16] and increase the probability of extreme weather events like droughts, storms, and floods. To prevent this, legislative efforts like the Paris Agreement [17] and the European Green Deal [18] stipulate to keep the average global temperature rise well below 2 °C by curbing anthropogenic CO_2 emissions.

Consequently, there is a growing interest to find a sustainable alternative for the HB process [3, 5, 7, 19]. In an ideal case, renewable electricity is used to power the production of NH_3 consuming N_2 from air and water, which paves the way for a potentially emission-free NH_3 production industry. Several different sustainable production methods exist with varying commercial readiness levels (CRL), and have been researched in several papers, including MacFarlane et al. [3], Smith et al. [5], Wang et al. [7] and Nørskov et al. [19]. A specific approach for sustainable NH_3 synthesis, in which NH_3 is synthesised in an electrolyzer through the electrochemical N_2 reduction reaction (e-NRR), has recently gathered research attention and appears compelling for numerous reasons. Although it is still in the research phase (CRL 1-3 [7]) and state-of-the-art performance falls below commercial relevance, this method can synthesise NH_3 from abundant air and water, and can directly take electricity as input to drive the reaction [3, 20, 21].

2 Motivation

The feasibility of the e-NRR is determined by its cost-effectiveness when compared to the industry standard. Therefore, gaining insight into the techno-economic performance of NH_3 production via e-NRR is relevant. It is interesting to explore if it has the potential to replace the (HB) benchmark, and under what conditions this will be the case.

A small number of recent techno-economic assessments of e-NRR NH_3 production can be found in the literature. Wang et al. [7], Hochman et al. [22] and Fernandez et al. [23], found that this pathway has the potential to be a potentially more cost-effective alternative to HB, although its success depends on the electrolyzer performance and electricity price. In these studies, different e-NRR conceptual process designs were used to estimate the NH_3 production cost. Nevertheless, these papers did not investigate the effect of varying scales, and only considered one type of electrolyzer in their process. Hence, the goal of this thesis is to design conceptual processes with different types of electrolyzers (alkaline electrolyzer, gas diffusion electrode flow cell, solid-oxide electrolyzer) at varying scales (ranging from small (91 tonnes NH_3 per day), medium (544 tonnes NH_3 per day) and large (2055 tonnes NH_3 per day)). These process designs are subsequently used to find the necessary techno-economic conditions under which e-NRR will be an attractive alternative in comparison with HB.

3 Research Question

What performance criteria must be met for NH_3 synthesis via e-NRR to reach cost competitiveness with HB?

Subquestions

- How is the (energetic and economic) performance of the HB benchmark?

- What pre- and post-treatment equipment is required for e-NRR NH_3 synthesis?

- What electrolyzer parameters have the largest influence on e-NRR performance and the NH_3 production cost?

- Under what (energetic and economic) performance conditions would e-NRR NH_3 synthesis be comparable to the SMR-HB benchmark?

- What type of electrolyzer and scale are most applicable for e-NRR NH_3 synthesis?

4 Thesis Outline

The second chapter of the thesis starts with a literature review (Chapter 2), where recent studies about different industrially applied (HB) production methods are discussed (Section 1). This is used as the performance benchmark of the present-day NH_3 industry. Subsequently, the necessary background knowledge for e-NRR will be presented in Section 2. This is followed by an analysis of the required pre- and post-treatment steps in Section 3, which will be used for choosing the required pre- and post-treatment unit operations for the conceptual e-NRR processes.

Chapter 3 will present the developed conceptual processes and describe the methodology and assumptions. Chapter 4 presents the results and discussion of the base-case simulations and sensitivity analysis. At last, Chapter 5 and 6 conclude our findings and provide recommendations for future work.

Chapter 2

Literature Review

1 Current Ammonia Production Methods

This section discusses the latest scientific literature regarding commercially implemented NH_3 production technologies. It aims to give the reader the necessary background information about HB, and it identifies the current energetic and economic benchmark for industrial NH_3 synthesis.

1.1 Haber-Bosch Process

1.1.1 History

N_2 was first successfully converted to NH_3 on an osmium catalyst by Fritz Haber and Robert Le Rossignol [20]. After that, in the early part of the 20th century, Carl Bosch at BASF scaled it up using iron catalysts combined with high operating pressures, which presented HB as a reliable and effective way to fixate N_2 and synthesise large quantities of NH_3 with low production costs [24]. In the first four decades of the 20th century, N_2 fixation was also done via the Birkeland-Eyde process and Frank-Caro process, which interestingly did not produce significant emissions [25]. After the 1940s, HB replaced the other processes due to its lower energy consumption, cheap natural gas (NG) feedstock, and up-scaling potential. At present, approximately 96% of the global NH_3 production is produced via this process, contributing to 1.4% of total anthropogenic CO_2 emissions [5].

1.1.2 Reaction

The HB reaction, which converts N_2 and H_2 to NH_3, is presented in Equation 2.1.

$$N_2 + 3\,H_2 \rightleftharpoons 2\,NH_3 \qquad \Delta H = -91.8 \, kJ \cdot mol^{-1} \tag{2.1}$$
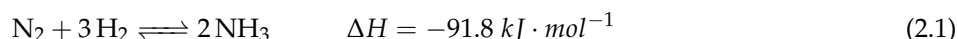
While this reaction is exothermic, it requires breaking of the stable N≡N bond, which has a large ionisation energy and explains the inertness of the N_2 molecule [26]. Hence, HB requires an active, durable, cost-effective and poison resistant catalyst [27], high temperatures (400-500 °C), and pressures (>100 bar), to achieve acceptable reaction kinetics. The industry still applies heterogeneous Fe-based catalysts like Ferrite, as has been done since the 20th century. Moreover, HB requires a feed of H_2, which usually comes from fossil fuels like NG, coal or oil.

1.1.3 Process Description

HB can be separated into three parts: (1) feed pre-treatment, (2) NH_3 synthesis and (3) post-treatment. A simplified process flow diagram of a steam-methane reformed (SMR) HB is shown in Figure 2.1.

State-of-the-art NH_3 plants are usually based on NG (72% of existing HB facilities), whereas older plants can be based on coal or oil (around 22%) [28]. The NG-process referred to as SMR-HB, with regard to the steam methane reforming (SMR) step for H_2 production. SMR-HB is considered the best available technology (BAT) with the highest energy efficiency and lowest CO_2 emissions. Hence, this section considers the NG-based process.

Preceding the SMR step, the NG feed is desulfurized to remove impurities that are poisonous the catalyst of SMR. Then, NG together with high-pressure steam is converted to syngas (CO and H_2) in the SMR reactor at

high temperatures (850-900 °C) and pressures of 25-35 bar over a catalyst [5]. The SMR reaction is endothermic, as is shown in Equation 2.2, hence the reactor needs be heated.

$$CH_4 + H_2O \rightleftharpoons CO + 3\,H_2 \qquad \Delta H = 206\ kJ \cdot mol^{-1} \tag{2.2}$$
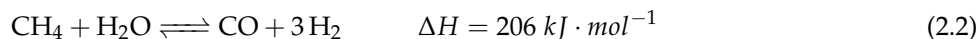
The H_2 production step can work via either a single or double SMR step. In the case of a single SMR reactor, air is first separated into pure N_2 using an air separation unit. On the other hand, when a double SMR step is applied, the product from the first SMR reactor is sent to an autothermic reforming (ATR) reactor. Here, oxygen (O_2) from air and unreacted CH_4 are converted into syngas (as shown in Equation 2.3).

$$2\,CH_4 + O_2 \rightleftharpoons 2\,CO + 4\,H_2 \qquad \Delta H = -71\ kJ \cdot mol^{-1} \tag{2.3}$$
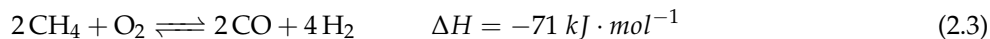
The remaining CO is converted into additional H_2 by the Water-Gas shift (WGS) reactor, where CO and steam are converted to H_2 and CO_2 according to reaction Equation 2.4. Since the HB-reactor is sensitive to CO and CO_2 poisoning, CO_2 needs to be removed by a Benfield or Selexol scrubber [5].

$$CO + H_2O \rightleftharpoons CO_2 + H_2 \qquad \Delta H = -41\ kJ \cdot mol^{-1} \tag{2.4}$$
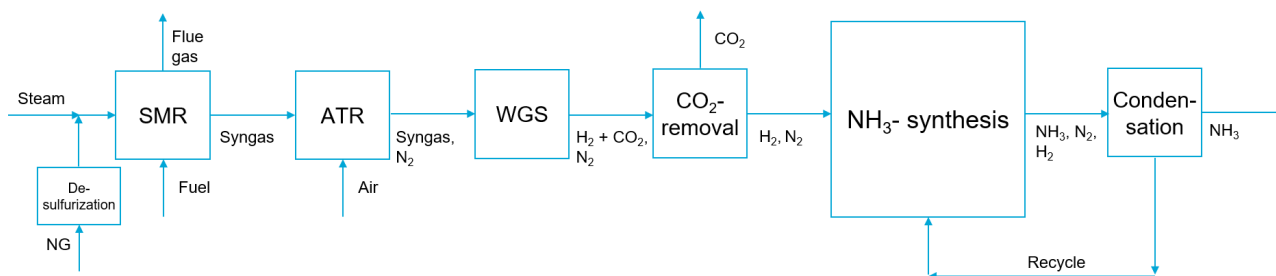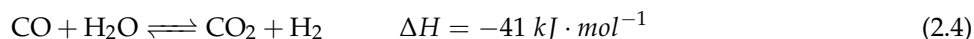
Figure 2.1: Simplified process flow diagram of a methane fed Haber-Bosch process (SMR-HB).

The reactants (H_2 and N_2) are compressed and heated, and fed to the NH_3 synthesis reactor where they are converted to NH_3 (the single pass conversion is around 15% [5]). This stream is fed through a waste heat boiler, and NH_3 product with unreacted N_2 and H_2 are fed to the condenser. Due to the temperature difference, NH_3 condensates whereas unreacted H_2 and N_2 are recycled back to the NH_3 synthesis reactor.

1.1.4 Scale

SMR-HB plants benefit from economies of scales. According to *Ullman's Encyclopedia of Industrial Chemistry* [27], typical plant capacities range from 1,200 to 2,000 tonnes NH_3 per day (t d^{-1}). More recently, plant capacities have increased to 3,300 t d^{-1} [25]. Nevertheless, there are also examples of smaller-scale projects (100-600 t d^{-1}) being commissioned, despite the widespread belief that large-scale NH_3 production is superior due to the high capital intensity of small-scale HB [29, 22].

1.1.5 Energy Consumption

In Figure 2.2, the average energy consumption of HB is shown over the past seven decades. It highlights that HB has made considerable energy efficiency progress since 1950, and the average energy losses have stagnated since 1995 [5].

Smith et al. [5] reports that modern SMR-HB has an energy efficiency between 62 and 65%. The SMR step accounts for 90% of the total energy input [24], and accounts for 10% of the energy losses of the process. Fundamentally, the maximum energy stored in one tonne of NH_3 is expressed via the lower heating value (LHV), which is equal to 18.65 GJ t^{-1} for NH_3 [30]. The theoretic minimal energy requirement for SMR-HB is equal to 22.2 GJ t^{-1} [5]. This includes the energy losses during combustion of NG, and non-recoverable heat losses due to high SMR temperatures (>850 °C). In reality, the BAT consumes 29.4 GJ t^{-1}, which is approximately 23.5% more than the theoretical limit. To add, in an earlier published report ([15]), it was mentioned that the average energy consumption of HB plants is considerably larger than the BAT, reporting an average energy consumption of 38.6 GJ t^{-1}.
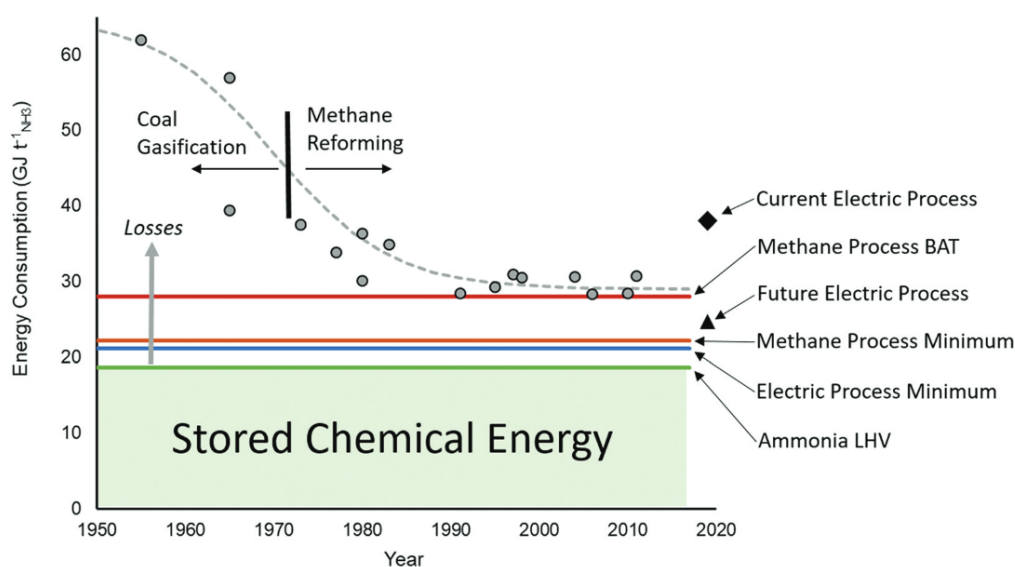
Figure 2.2: Historical energy consumption (GJ t^{-1}) of HB plants over the past seven decades, showing the theoretical minimum energy requirement, as well as the SMR-HB BAT and electrified process. Obtained from Smith et al. [5].

1.1.6 Emissions

The average emissions from HB can vary, depending on the type of feedstock for the H_2 production step (oil, coal, or natural gas) and the age of the plant. The primary source of emissions is stoichiometric CO_2 production in the SMR reaction, which emits roughly 1.22 tonnes CO_2 per tonne NH_3 (t_{CO_2} t^{-1}) [5]. Another important contribution is the flue gas from heating of the SMR reactor and the supply of steam, which emits 0.27 t_{CO_2} t^{-1} [5]. Next to SMR emissions, HB requires pressurisation which emits another 0.17 t_{CO_2} t^{-1}. The total emissions are 1.67 t_{CO_2} t^{-1}, as calculated by Smith and colleagues [5].

1.1.7 Ammonia Production Cost

The Levilised Cost of Ammonia (LCOA) is a measure of the cost of producing NH_3 over the lifetime of a production facility, and is a powerful metric in determining the economic attractiveness of NH_3 production technologies [7, 22, 23]. The LCOA includes the cost of building (capital expenditure) and operating the plant, as well as the cost of the feedstocks and other materials used to form NH_3 (operational expenditure). It is expressed as the cost per unit of NH_3 (such as $ per tonne ($ t^{-1})).

Figure 2.3, which uses data from the forthcoming publication by Izelaar et al. [31], shows that the LCOA of existing HB facilities decreases from 602 to 339 $ t^{-1} with increasing scale. This indicates that HB benefits significantly from the economies of scale. The largest contributors to the capital cost will be the heat exchangers and pressure turbines, along with the HB reactor. The NG costs represent the most substantial operational expenditure [32]. In addition, the LCOA becomes slightly higher if a CO_2 tax of 51 $ $t_{CO_2}^{-1}$ is taken into consideration, which is equally shown in the figure.

1.2 Haber-Bosch with Carbon-Capture and Storage

As was explained in Section 1.1, SMR-HB processes already capture the stoichiometric CO_2 produced in the SMR step, since CO_2 is poisonous to the HB reactor. However, despite the fact that 130 tonnes of CO_2 have been captured in HB facilities in 2020, only 2 tonnes have been permanently stored [12]. The captured CO_2 is either vented into the atmosphere or temporarily stored in urea, a common type of fertiliser. Once the urea is applied to the soil, the CO_2 is emitted to the atmosphere [33].

SMR-HB processes have two CO_2 streams, one from the SMR step and one from flue gasses. Capturing CO_2 from the flue gasses is more challenging, since these have lower CO_2 concentrations. For SMR-HB plants, the additional cost of CCS are estimated between 100 and 150 $ per tonne NH_3, which includes decarbonising the flue gas streams and the permanent storage of CO_2 [28]. The addition of carbon storage for NH_3 synthesis can yield 'blue ammonia', which appears to be the preferred choice of reducing CO_2 emissions from existing HB facilities [34].
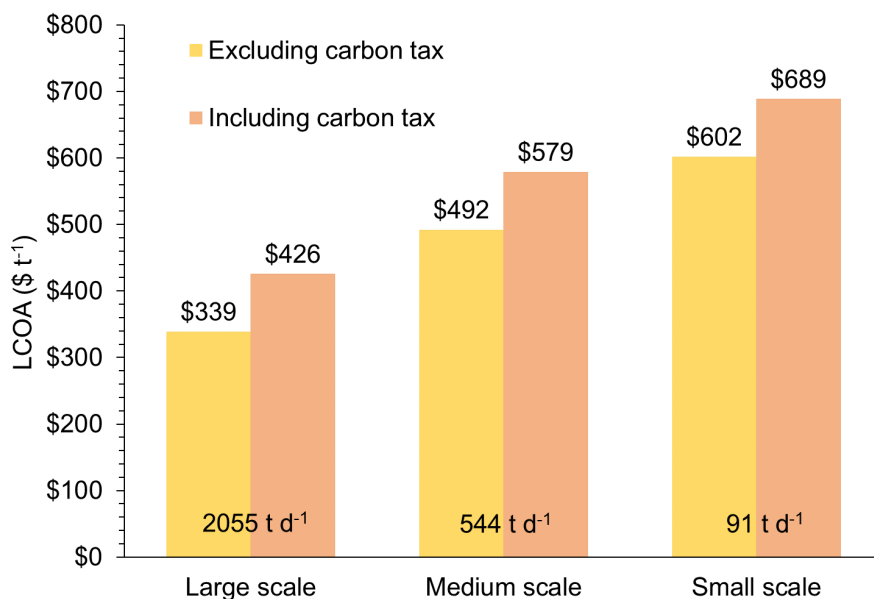
Figure 2.3: The effect of NH_3 capacity (t d^{-1}) on the LCOA ($ t^{-1}). Data obtained from the forthcoming publication by Izelaar et al. [31].

1.3 Electrified Haber-Bosch

An alternative way to decrease CO_2 emissions is to replace the SMR step with renewable H_2 production through electrolysis. The electrified HB process (e-HB) is the combination of electrolysis-produced H_2 with a HB synthesis loop [3]. This process can be fully powered by electricity, potentially from renewable sources.

In 1930, approximately 30% of NH_3 plants already relied on electrochemical H_2 production [28]. This changed when NG became more abundant and less expensive, resulting in the majority of existing NH_3 facilities implementing SMR-HB. However, the cost of renewable electricity has decreased in the past years. This led to a rapid increase in the number of e-HB plant construction announcements [28].

In Figure 2.4, a simplified representation of e-HB can be found. Notably, this process requires an additional air separation unit (ASU) to supply N_2 to the HB reactor. In Section 3.1, the ASU will be analysed in more detail. The HB-loop is similar to conventional HB, with the difference being that it can potentially be powered by electricity. Hence, the following sections will elaborate more on the basic principles and technology behind water electrolysis.
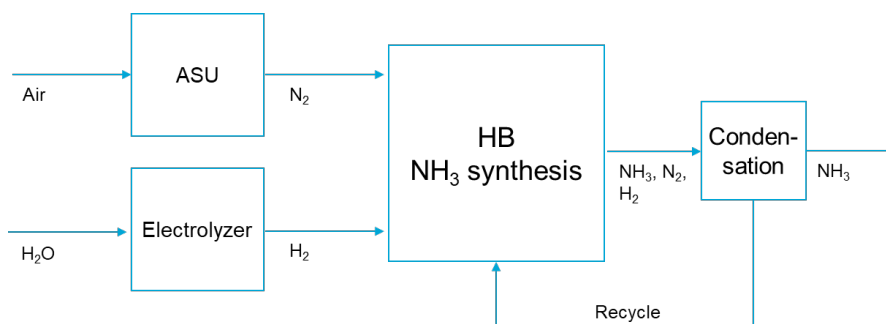
Figure 2.4: Simplified process flow diagram of an electrified HB process.

1.3.1 Fundamentals of Water Electrolysis

Water electrolysis refers to the electrochemical dissociation of water (H_2O) to H_2 and O_2 [35], of which the reaction equation is displayed in Equation 2.5.

$$H_2O \xrightarrow{\text{electricity}} H_2 + 0.5\,O_2 \qquad E^0_{cell} = -1.23\ V \qquad (2.5)$$
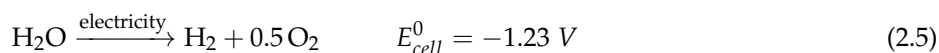
Electrochemical reactions can be split up into two half-reactions: an oxidation reaction and reduction reaction,

as can be seen in Equation 2.6 and 2.7 respectively. In an electrochemical cell, the reduction reaction will occur at the cathode, whereas the oxidation reaction happens at the anode, and the respective reductive (E^0_{red}) and oxidative (E^0_{ox}) potentials are expressed versus the standard hydrogen electrode (SHE).

$$2\,H^+ + 2\,e^- \longrightarrow H_2 \qquad E^0_{red} = 0.0\ V_{SHE} \tag{2.6}$$

$$2\,H_2O \longrightarrow O_2 + 4\,H^+ + 4\,e^- \qquad E^0_{ox} = +1.23\ V_{SHE} \tag{2.7}$$
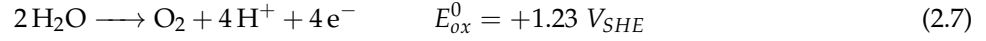
The total energy or enthalpy (ΔH) required for this reaction (Equation 2.8), is partially supplied electrically (ΔG) and by heat (ΔQ), since water splitting is endergonic (non-spontaneous). The equilibrium cell potential (E^0_{cell}) can be calculated through Faraday's law as stated in Equation 2.9, and can be interpreted as the minimal electrical energy required to split water in volts (V). In reality, one must supply some heat. The thermo-neutral potential (E^0_{tn}), equal to -1.48 V, is defined as the minimum total energy required to split water, as is shown in Equation 2.10. In these equations, z is defined as the number of electrons transferred per mole of water ($z = 2$) and F is equal to the Faraday constant ($F = 96485.33\ C\ mol^{-1}$).

$$\Delta H = \Delta G + \Delta Q \tag{2.8}$$

$$E^0_{cell} = -\frac{\Delta G}{zF} \tag{2.9}$$

$$E^0_{tn} = -\frac{\Delta H}{zF} \tag{2.10}$$

ΔH, ΔG and ΔQ fundamentally depend on the temperature, hence the minimum electrical and total energy requirement of water splitting varies with temperature. This effect can be seen in Figure 2.5. Note that the electric energy ΔG is significantly reduced at increased temperature, resulting in lower cell potentials for water electrolyzers working at elevated temperatures.
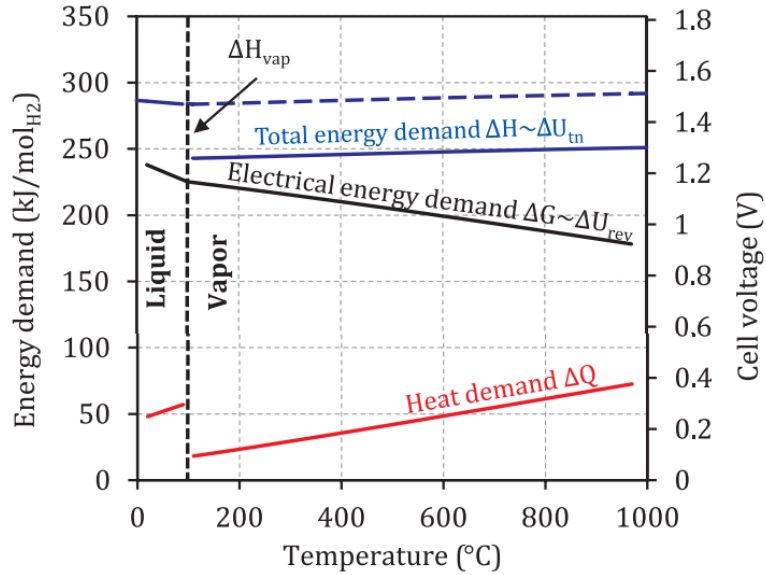
Figure 2.5: Dependence of total energy (ΔH), electrical energy (ΔG) and thermal energy (ΔQ) on the temperature. Obtained from Buttler and Spliethoff [35].

Commercial electrolyzers are operated at voltages higher than the thermo-neutral potential, due to internal energy losses. The applied potential is between 1.5 and 2.2 V, and depends on the operating temperature and pressure, as well as the current density (J) [35]. J is an operational parameter of electrochemical systems and is defined as the current (I) divided by the electrode area (A_e). Working at high J is desired since this maximises the formation of H_2 per unit of electrode area. However, an increased J is accompanied with larger energy losses in the system.

1.3.2 Electrolyzer Types

Buttler and Spliethoff discuss three main cell configurations for water electrolyzers [35]: the Alkaline Electrolyzer (AEL), the Proton Exchange Membrane Electrolyzer (PEMEL) and the Solid Oxide Electrolyzer (SOEL). These cells differ in the type of electrolyte used, as well as the type of membrane and electrode material. The AEL has been in commercial use since the 1910s and use an alkaline aqueous electrolyte. Conventionally, the cell operates at 80 °C and atmospheric pressure (1 bar) with a 25 wt% KOH electrolyte. The PEMEL makes use of a proton-exchange membrane (like Nafion), which acts as a solid electrolyte between the cathode and the anode. The main advantage of the PEMEL is that it benefits from lower cell resistances and can be operated at higher J. Additionally, it can produce H_2 at elevated pressures, thereby decreasing the post-treatment pressurisation requirement [35]. At last, the SOEL requires high temperatures, which thermodynamically decreases ΔG and E^0_{cell} (see Figure 2.5). Hence, these devices can work at high electrical energy efficiencies, although significant heat input (ΔQ) is required too.

In Table 2.1, one can find the typical operating conditions of the different electrolyzers. Note that the AEL and PEMEL are already commercially available with high stack capacities, and the SOEL is available on a lower scale.

Table 2.1: Typical performance parameters of state-of-the-art water electrolysis systems. Data obtained from Buttler and Spliethoff [35].

Parameter	AEL	PEMEL	SOEL
Cell temperature (°C)	60-90	50-80	700-900
Current Density (A cm^{-2})	0.25-0.45	1.0-2.0	0.3-1.0
Available Capacity per stack (Nm^3 h^{-1})	1400	400	<10
Nominal Stack Efficiency (LHV) (%)	63-71	60-68	100

1.3.3 Ammonia Production Cost

The electricity price is an important measure within feasibility studies of e-HB [7, 3, 5]. Electrolyzer operation usually encompasses half of the production cost in e-HB [28]. Electrolyzer equipment cost contributes significantly too (approximately 10^6 \$ MW^{-1}), resulting in increased capital intensity of e-HB [3]. Next to large costs, intermittent operation of the HB loop in e-HB is challenging. HB is optimally operated continuously, which conflicts with the day-night pattern of solar power, and seasonal fluctuations in wind power [3]. Hence, the operation of the HB-loop will likely require additional energy storage infrastructure.

The production cost of e-HB is estimated between 720 and 1400 \$ t^{-1} [28]. It is expected that this will decline to 310-610 \$ t^{-1} by 2050, due to the forecasted decrease in the renewable electricity price and equipment cost [28].

2 Electrochemical Ammonia Synthesis

This section will explore an alternative pathway for the production of NH_3 that does not require a HB reactor. This pathway employs the e-NRR, which occurs in an electrolyzer and takes water as the H-source. There are two modes of electrochemical NH_3 synthesis described in literature: (1) an electrocatalyst facilitates the direct electron and proton addition to N_2 via the e-NRR and (2) a redox mediator (like Li^+) is reduced, which then facilitates the conversion of N_2 to NH_3 [3]. The second mode is out of the scope of this research, and this section will focus on direct electrochemical synthesis of NH_3 via e-NRR.

2.1 Electrochemical Nitrogen Reduction Reaction (e-NRR)

NH_3 synthesis via the e-NRR has gathered a lot of research attention in the past decade [3, 28], and is an interesting future replacement for HB for a couple of reasons:

- The high operating pressures and temperatures of HB can be avoided, since e-NRR allows for NH_3 production at ambient temperatures and pressures [3, 25, 36].

- e-NRR can potentially produce NH_3 with a lower energy intensity than the existing methods (Section 1) [3], at a thermodynamic minimal energy requirement of 19.9 GJ per ton NH_3 [5, 37].

- The process can be fully powered by renewable electricity, and the modular electrolyzer design makes it more suitable for intermittent operation, an important element in the future energy system [3, 38]. This way, the climate impact of NH_3 production can be mitigated by directly pairing the process to renewable electricity produced via solar or wind power (power-to-NH_3).

- e-NRR hydrogenates N_2 with protons (H^+) directly, using water as a reactant, thereby undermining the conversion of hydrocarbons to H_2. This process is emission-free, and allows for NH_3 production from the abundant molecules N_2 and H_2O [36]. This equally allows for more decentralised production since the necessary proximity to natural gas reserves is deleted.

2.1.1 Fundamentals of e-NRR

The e-NRR reaction equation is shown in Equation 2.11 and consist of two half-cell reactions (shown in Equations 2.12 and 2.13 in an acidic environment).

$$2\,N_2(g) + 6\,H_2O\,(l) \xrightarrow{\text{electricity}} 4\,NH_3\,(g) + 3\,O_2\,(g) \qquad E^0_{cell} = -1.17\ V \tag{2.11}$$
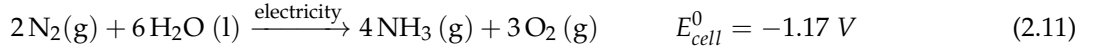
The reduction of N_2 (Equation 2.12) takes place on the cathode, and involves the consumption of three electrons per mole of NH_3, which are supplied by an external direct current (DC) power supply. The counter-reaction on the anode (Equation 2.13) is known as the oxygen evolution reaction (OER), which splits water in protons and O_2.

$$N_2 + 6\,H^+ + 6\,e^- \longrightarrow 2\,NH_3 \qquad E^0_{cat} = +0.092\ V_{SHE} \tag{2.12}$$

$$2\,H_2O \longrightarrow 4\,H^+ + O_2 + 4\,e^- \qquad E^0_{an} = +1.23\ V_{SHE} \tag{2.13}$$
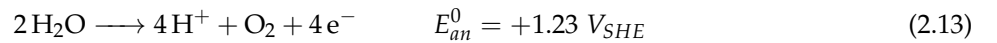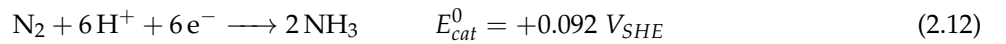
The minimum thermodynamic electrical energy requirement (ΔG) was calculated at 25 °C and 1.01325 bar, and converted to the minimum reversible cell potential (E^0_{cell}) in Appendix A. Equation 2.11 shows that E^0_{cell} for one-step e-NRR is equal to -1.17 V. Per unit of NH_3, the minimum energy requirement will thus be equal to 329.3 kJ mol^{-1} or 19.9 GJ t^{-1}. In some cell environments, NH_3 will not form as a gas but it will dissolve into the electrolyte, which changes the reversible cell potential to -1.14 V (329.3 kJ mol^{-1} or 19.3 GJ t^{-1}).

Energy losses during operation of the cell are caused by inefficiencies (overpotential). The total cell potential consists of the following contributions, the sum of which yields the total cell voltage, as shown in Equation 2.14.

$$E_{total} = E_{cell} + \eta_{act} + \eta_{Ohm} + \eta_{con} \tag{2.14}$$

(a) E_{cell} = *reversible cell potential*: The potential that is thermodynamically required in a perfectly reversible electrochemical cell. It can be corrected via the Nernst equation (Equation 2.15) to account for the concentration and temperature.

$$E_{cell} = E^0_{cell} - \frac{RT}{zF} ln\left(\frac{a_{product}}{a_{reactant}}\right) \tag{2.15}$$

where:

E^0_{cell} = reversible cell potential at 25 °C and 1.01325 bar.

R = universal gas constant.

T = temperature.

z = number of electron transfers.

F = Faraday constant.

$a_{product}$ = activity of products.

$a_{reactant}$ = activity of reactants.

(b) η_{act} = *activation overpotential*: The potential needed to overcome the activation barrier of the half-reactions. This is influenced by the e-NRR and OER catalysts and will be further discussed in the next subsections.

(c) η_{Ohm} = *Ohmic resistance*: Losses caused by charge transfer resistances within the cell. These can be caused by the electrolyte, separator membrane and electrodes. Their contribution is usually calculated via the ionic conductivity per unit of distance, and is dependent on the operational current density and temperature of the cell. High current densities will increase the Ohmic overpotential (via Ohm's law ($U = I \cdot R$)).

(d) η_{con} = *concentration overpotential*: This type of overpotential is caused by the concentration gradient of reactants and products between the bulk electrolyte and the electrode surface, caused by mass transport limitations. When the reaction is significantly fast, for instance when high current densities are applied, the reactants are depleted quickly, and cannot be replenished from the bulk. The electrode reactant concentration is thus reduced, which results in higher Nernst (Equation 2.15) and activation overpotentials [39]. The limiting current density (J_{lim}) is defined as the current where the electrode reactant concentration falls to zero under operation, which will directly cease product formation. If the operational current density is 90% of J_{lim}, the concentration overpotential is negligible (around 10 mV) [40].

e-NRR can also be performed with H_2 as the proton source, resulting in H_2 oxidation at the anode. This is known as two-step e-NRR, and its reaction is shown in Equation 2.16 below. Thermodynamically, this reaction appears spontaneous ($\Delta G < 0$) since the standard equilibrium cell potential is +0.057 V. Nevertheless, H_2 must be produced by a secondary H_2O electrolyzer, which requires -1.23 V, so the total cell voltage of the complete process remains -1.17 V. Looking at the current body of research, it appears that using H_2 as the H-source improves the NH_3 production rate [41]. Nonetheless, an obvious drawback is that this process requires two electrolyzers, which both work at overpotentials, which results in a lower possible process efficiency. According to Soloveichik [38], the exact benefits of two-step e-NRR are not yet known.

$$N_2 \text{ (g)} + 3\,H_2 \text{ (g)} \xrightarrow{\text{electricity}} 2\,NH_3 \text{ (g)} \qquad E^0_{cell} = +0.057 \; V \qquad (2.16)$$
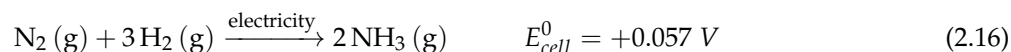
2.1.2 Activity

In e-NRR, the strong N≡N triple bond must be broken for nitrogen atoms (N) to be protonated. Section 1.1 explained that HB uses high temperatures in combination with a catalyst to overcome this activation barrier. Similarly, for e-NRR, N-activation is a considerable challenge, and reaction kinetics are sluggish at ambient conditions. While the exact mechanism of e-NRR is not completely understood [41], it appears that N-activation at ambient conditions is a bottleneck for the performance of e-NRR systems [42, 43, 44]. To overcome this, recent research efforts have therefore gone into identifying appropriate electrocatalysts, where transition metals appear to significantly lower the activation barrier of the e-NRR [45]. Next to this, another possibility to increase activation is by working at higher temperatures. Bi et al. mention that increasing the temperature increases the rate constant of the reaction through the Arrhenius equation (Equation 2.17) [36]. This equation shows the dependency of the rate constant (k) on the activation energy (E_a), pre-exponential factor (A) and the temperature (T). A lower activation energy and a higher temperature will thus increase k and result in a faster reaction and higher NH_3 production rates.

$$k = A \cdot exp(\frac{-E_a}{RT}) \qquad (2.17)$$

2.1.3 Selectivity

The selectivity of electrochemical systems is commonly expressed as the Faradaic Efficiency (FE), which is defined as the charge consumed by the desired reaction (e-NRR) (I_{NH_3}), divided by the total charge of the cell (I_{total}). I_{NH_3} can be calculated via Faraday's law and NH$_3$ production rate (r_{NH_3}) (Equation 2.18):

$$FE = \frac{I_{\mathrm{NH_3}}}{I_{total}} \cdot 100\% = \frac{r_{NH_3} \cdot F \cdot z_{NRR}}{I_{total}} \cdot 100\% \tag{2.18}$$

where:
FE = the Faradaic Efficiency in %.
r_{NH_3} = production rate of ammonia in mol s^{-1}.
F = the Faraday constant (F = 96,485.33 C mol^{-1}).
z_{NRR} = number of electrons involved in the reaction (z_{NRR} = 3).

In e-NRR, there is one particular parasitic reaction that is problematic: the hydrogen evolution reaction (HER). The half-cell potential for HER (E_{HER}^0 = 0.0 V_{SHE}), is particularly close to that of e-NRR (E_{NRR}^0= +0.092 V_{SHE} at pH 0) [36]. As a result, both reactions can be activated simultaneously if we neglect each independent activation barrier. Consequently, HER is a fundamental and considerable side reaction in e-NRR cells. According to Soloveichik [38], HER kinetics increase faster with increased potentials than the e-NRR. Furthermore, e-NRR is a 6th proton-coupled electron transfer (PCET) reaction with multiple intermediate steps [2]. This means that the activation barrier is much higher than for HER, which contains only 2 PCETs. Estimated by density functional theory calculations (DFT), the minimum required overpotential for the e-NRR lies between -0.4 and -0.6 V [2, 45, 46]. This is significantly higher than for the HER, which approach 0 V close to optimal conditions.

An ideal catalyst would suppress the formation of H$_2$, while still increasing the activity for N-activation. New catalysts can be found using DFT, which theoretically calculates the optimal binding energies of catalysts, and evaluates if they can lower the activation energy of the rate-determining step(s). Skúlason et al. [45] found that transition metals such as Mo, Fe, and Ru are good catalysts, lowering activation energies of the rate limiting steps of e-NRR. However, these metals are known to also catalyse HER. More recently, Drăzevic and Skúlason [46] published an article where they mention that Mn, Ga and In could theoretically be stable in aqueous solutions and suppress HER, thereby opening up potential for higher FE. However, this has yet to be validated experimentally.

2.1.4 State-of-the-art e-NRR Performance

Primarily due to the activity and selectivity challenges mentioned above, research on NH$_3$ synthesis through e-NRR has not yet achieved commercial competitiveness [3, 41, 36]. The level at which electrocatalytic processes are expected to be economically viable has been previously explored by the United States Department of Energy (DoE) REFUEL program [13], which defined guidelines based on the NH$_3$ production rate (r_{NH_3}), current density (J), Faradaic Efficiency (FE) and energy efficiency (EE). Martin et al. [41] reviewed the gap between the performance of current e-NRR literature versus the DoE goals (Figure 2.6). They concluded that e-NRR is still far away from reaching HB parity.

In a more recent study, detection challenges of NH$_3$ were addressed, including the identification of several false positives in the e-NRR field [47]. Due to the low product yields, experiments are susceptible even to small concentrations of extraneous (external) N-impurities. It is expected that (^{15}N-isotope) N$_2$ feed gasses contain impurities such as NO$_x$ [47], which are easily reduced to NH$_3$. Such contamination can also come from components within the cell, like electrolyte or electrode materials [25]. Consequently, research about e-NRR must be evaluated critically to rule out false positives. In the research by Bi et al. [36], the current state-of-the-art of e-NRR was determined by reviewing recent research efforts. They evaluated whether the experiments conducted isotope-labelled control tests, thereby decreasing the opportunities for false NH$_3$ detection. Table 2.2 shows their results for performance of present-day e-NRR NH$_3$ synthesis, as well as the DoE performance targets.

Here, the gap between current e-NRR performance and DoE targets becomes more evident. NH$_3$ production rates are still 1000 times smaller than the DoE guidelines. Also, the DoE-reported FE of 95% is far off, especially considering that most experiments report a FE of less than one percent [48, 38].
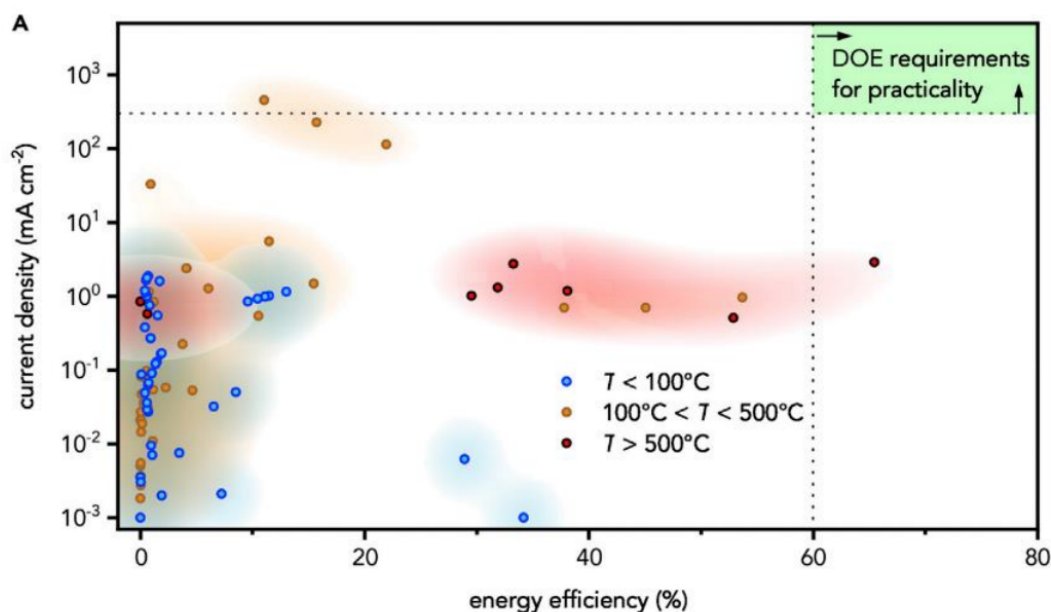
Figure 2.6: Performance map of state-of-the-art electrochemical NH_3 synthesis in three temperature ranges: high temperature (T>500 °C) (red), medium temperature (100 °C < T < 500 °C) (orange) and low temperature (T<100 °C) (blue). The U.S. DoE targets are also shown. Obtained from Martin et al. [41].

Table 2.2: Performance of state-of-the-art e-NRR research versus the performance targets of U.S. DoE. Data obtained from ref. [13] and [36].

Performance Metric	DoE target [13]	State-of-the-art [36]
r_{NH_3} (mol s^{-1} cm^{-2})	>10^{-6}	<10^{-9}
J (A cm^{-2})	>0.3	$<0.3 \cdot 10^{-3}$
FE	>95%	<30%

2.2 Electrochemical Cell Configurations

Numerous publications have emerged on e-NRR electrolyzer cell configurations, which aim to address this 'performance gap' [43, 49]. These papers are focused on improving e-NRR activity and selectivity via the application of new electrocatalysts and electrolytes. As was mentioned, finding appropriate cathode materials remains challenging. In contrast, anode electrodes are commercially available, and are typically based on transition metals like iron (Fe) and Nickel (Ni) [50].

The electrolyte is responsible for the transfer of ions between the anode and cathode. Depending on the electrolyzer configuration and operating temperature, the electrolyte is either in the solid or liquid phase. Solid state electrolytes generally consist of a membrane or ceramic electrolyte, which selectively conduct ions and physically separates the anode and cathode [51]. An example is Nafion, a commercially available proton conducting polymer electrolyte. Liquid electrolytes contain dissolved ions like aqueous potassium hydroxide (KOH) solutions. To minimise reactant or product crossover, liquid electrolyte cells require an additional separator (like Zirfon) to separate the anolyte and catholyte. The crossover of product could lead to leakage currents and product oxidation, which decreases cell efficiency [52].

2.2.1 Operating Temperature

The operating temperature of e-NRR cells has an optimum, as can be seen in Figure 2.7. It shows that elevating the temperature until 480 °C increases NH_3 production rates. This is due to increased ionic conductivity of electrolytes which reduces electrolyte resistances [36, 51, 53]. Nevertheless, when the temperature reaches 480 °C, selectivity is reduced since HER is thermodynamically favoured over the e-NRR [38]. Moreover, NH_3 decomposition to H_2 and N_2 becomes spontaneous at temperatures above 400 °C [54]. It is estimated that at experimental flow rates, NH_3 decomposition at 550 °C was approximately 20% [54]. Hence, NH_3 production at temperatures higher than 550 °C is seldom researched [48, 53, 51]. The effect of NH_3 decomposition can be

reduced by working at high flow rates [51], and cooling the outlet of the electrochemical cells to temperatures of 300 °C [55].
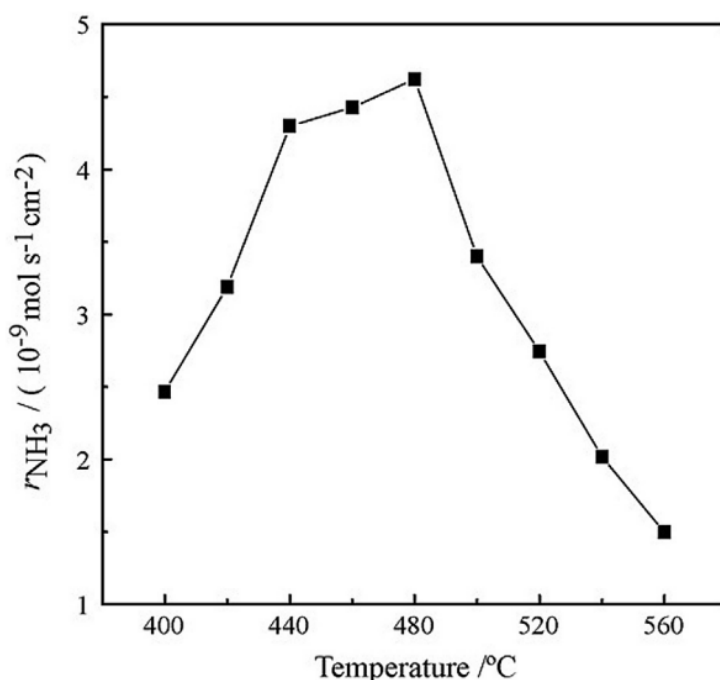
Figure 2.7: Effect of temperature on the NH$_3$ production rate (r_{NH_3}). Obtained from Gunduz et al. [53].

In literature, three main temperature domains for e-NRR can be distinguished: low temperature (T<100 °C), medium temperature (100 °C <T< 500 °C) and high temperature (T> 500 °C) [51, 48, 53]. The following bullet-points will explore recent developments in e-NRR literature for different types of possible electrolytes in these temperature domains:

- **Low temperature: (T<100 °C)**

  - *Aqueous electrolytes*: These types of electrolytes are widely applied in e-NRR research. The operating temperature needs to be between room temperature and 80 °C to minimise water evaporation. Increasing the temperature above room temperature will positively influence the ion-conductivity of the electrolyte [56], so the temperature is usually around 60-80 °C [49]. The electrolytes used predominantly in e-NRR research can be acidic (e.g. sulphuric acid (H$_2$SO$_4$) or alkaline (e.g. potassium hydroxide (KOH)), while an alkaline environment appears more suitable for the e-NRR [49].

  - *Ion conductive membranes*: Anion or cation conducting membranes are suitable for electrochemical NH$_3$ synthesis at room temperature. To be conductive, these types of membranes need to be kept wet with aqueous electrolytes, so it can be argued that the electrolyte is actually the combination of membrane and electrolyte solution. Nafion membranes (for instance from Dupont) were previously presented as a commercially applied cation exchange membrane, and possesses high proton conductivity at room temperature [48, 49]. Anion-exchange membranes lack a durable membrane material.

  - *Non-aqueous liquid electrolytes*: Non-aqueous (ionic liquid (e.g. 1-ethyl-3-methylimidazolium acetate) or aprotic (e.g. tetrahydrofuran)) electrolytes are conventionally operated at room temperature. These types have the potential to limit proton availability near the cathode, hence limit the parasitic HER [49, 36]. Nonetheless, their performance appears to be limited by the its low ionic conductivity, and these systems are therefore obstructed by very low NH$_3$ production rates ($<$ 0.002 $\cdot$ 10^{-10} mol s^{-1} cm^{-2} [57]).

- **Medium temperature: (100 °C<T<500 °C)**

  - *Molten Salts*: Elevated temperatures allow for the application of molten salt electrolytes, like chlorides (LiCl, KCl, CsCl) or hydroxides (NaOH, KOH). These electrolytes transfer nitride ions (N^{3-}) between the cathode and anode, which could theoretically limit the proton availability near the

13

cathode and increase FE [51]. In practise, these types of cell are troubled by limited N_2 solubility and poor system stabilities [42], and will not be treated further.

- *Solid acids*: These are a type of proton conducting solid state electrolytes, which are commonly applied in fuel cells [48]. Nevertheless, these electrolytes are not stable in the presence of NH_3, since this weak base will react with the acidic groups on the solid electrolyte. Solid acids will also not be elaborated further.

- **High temperature**: **(T>500 °C)**

    - *Oxygen or proton conducting (ceramic) electrolytes*: The most common type of high temperature electrolytes are comprised of solid oxide ceramics [51]. An example is Yttrium Stabilised Zirconia (YSZ), which is used in NH_3 fuel cells and high temperature water electrolysis [58]. YSZ can either conduct protons (H^+) or oxide ions (O^{2-}), with protons having a higher conductivity at temperatures below 600 °C [58]. An important limit of this operating temperature is the trade-off between electrolyte conductivity and the aforementioned NH_3 decomposition [53].

2.2.2   Cell Designs

The different electrolytes and operating temperature ranges described in the previous pages can form four electrolyzer cell configurations: the alkaline electrolyzer (AEL), a flow-cell with gas diffusion electrode (GDE), membrane electrode assembly cells (MEA) and solid oxide electrolyzers (SOEL), as shown in Figure 2.8. These types of electrolyzers were believed to possess the highest potential for industrial application, based on existing know-how from H_2O-electrolysis and applicability to e-NRR NH_3 synthesis.

- **Alkaline electrolyzer** (Figure 2.8a): The AEL make use of an alkaline liquid electrolyte. An alkaline cell environment is preferred over an acidic, since the formed NH_3 is a weak base and will likely be protonated to ammonium ions (NH_4^+), which are more difficult to isolate from the electrolyte. Moreover, the high acidity could restrict the choice of cathode material, since only noble metals are sufficiently stable at low pH. Therefore, the choice was made to limit this research to alkaline aqueous electrolytes.

    The half-cell reactions of e-NRR in the alkaline environment are shown in Equation 2.19 and 2.20 below. Note that the half cell potentials (E_{an}^0 and E_{cat}^0) are different to the ones previously displayed for the acidic environment (Equations 2.12 and 2.13), but the cell potential remains the same (E_{cell}^0 = -1.14 V since NH_3 will form in the aqueous phase).

$$6\,OH^- \longrightarrow 1.5\,O_2 + 3\,H_2O + 6\,e^- \qquad E_{an}^0 = +0.40\ V_{SHE} \qquad (2.19)$$

$$N_2 + 6\,H_2O + 6\,e^- \longrightarrow 2\,NH_3 + 6\,OH^- \qquad E_{cat}^0 = -0.74\ V_{SHE} \qquad (2.20)$$

    As shown in Figure 2.8a, H_2O will be oxidised to O_2 on the anode. The OH^- ions move to the cathode under the influence of an electric field, where they are used in the N_2 reduction to NH_3. The anode and cathode are electrically connected with an external circuit, which is also used to supply the potential difference. At last, a separator (Zirfon, displayed as the dotted line in the figure) is applied to separate the anolyte and catholyte.

    The primary advantage of the AEL is the extensive know-how from water electrolysis [3]. In research about e-NRR, it is often used as a cost-effective way to test new catalyst materials, due to the low cost of the aqueous electrolyte. Nonetheless, one must be wary of poor N_2 solubility and resulting mass transfer issues, that cause low limiting current densities (J_{lim}).

- **Flow-cell with gas diffusion electrode** (Figure 2.8b):

    In an effort to circumvent the poor N_2 solubility of water, recent research efforts have shifted towards the application of gas-diffusion electrodes [59, 60, 61]. From preceding research in CO_2 electrolysis, the GDE appears to be an interesting electrochemical cell for industrial applications [62], especially considering processes where reaction rates are limited due to mediocre reactant solubility. Furthermore, according to Kolen et al. [59] and Shahid et al. [61], the GDE can be advantageous in the electrosynthesis of NH_3, by mitigating the N_2 solubility issue and challenges of false-positives in product quantification.

    At the electrode surface of the GDE, N_2 will react on a triple phase boundary (TFB) reaction site (on the boundary of (1) electron conducting material, (2) the catalyst layer and (3) the electrolyte). In principle, this type of cell follows the same reactions as the AEL, but the primary difference is that N_2 is supplied
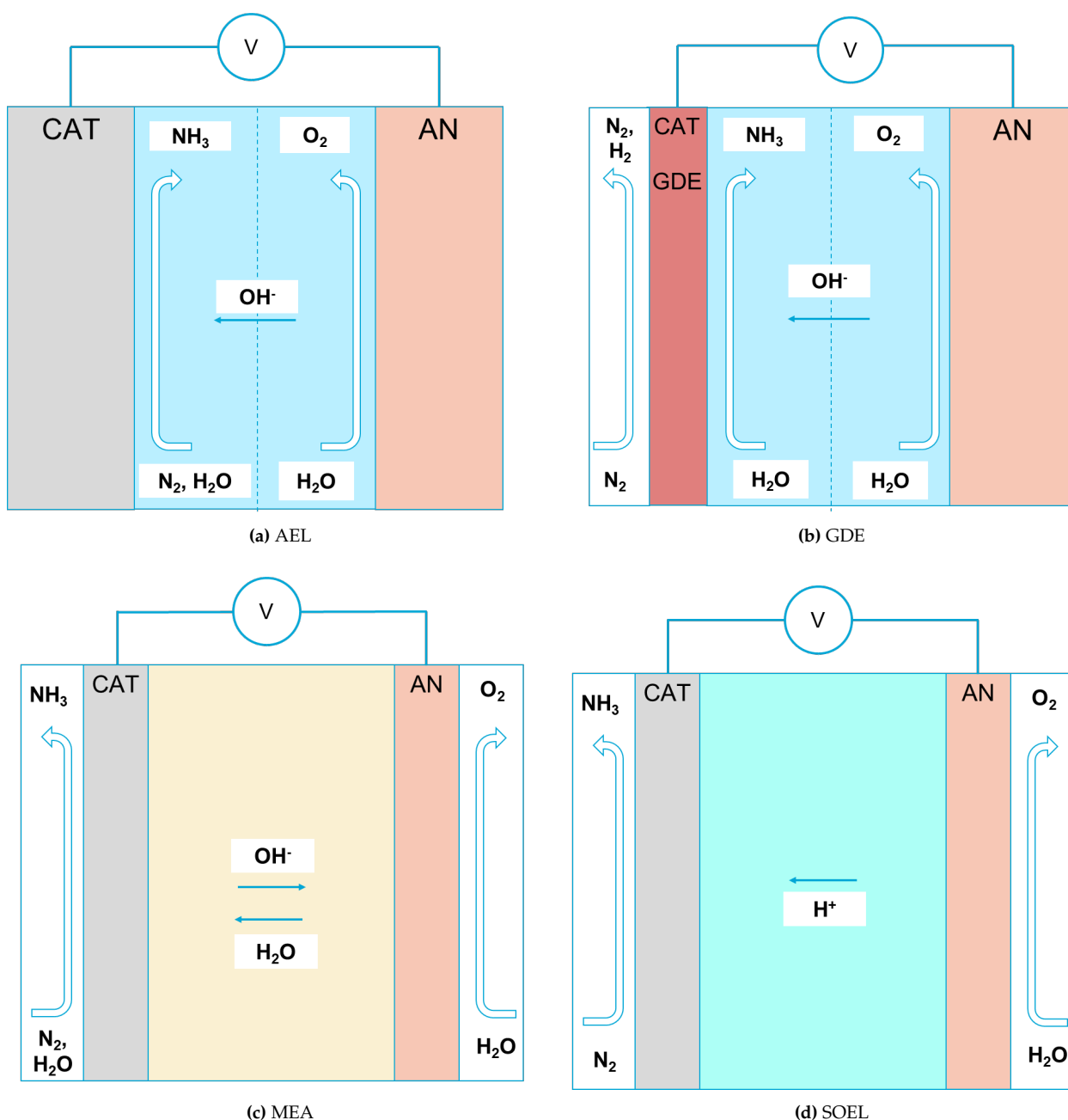
Figure 2.8: Overview of different electrolyzer types: (a) AEL, (b) GDE, (c) MEA and (d) SOEL.

from a secondary gas flow channel. N_2 therefore arrives at the TFB reaction site without the necessity of dissolution. After N_2 is reduced to NH_3 on the TFB, it is expected that the NH_3 formed on the electrode will move towards the aqueous phase [59]. On the contrary, unreacted N_2 (as well as H_2 by-product) will diffuse back towards the gas flow channel due to its much lower solubility.

This type of cell thus mitigates N_2 solubility problems, while still profiting from the cheap and simple operation of an aqueous electrolyte. Nevertheless, the GDE is yet to be proven on a commercially relevant scale [62], and e-NRR performance remains poor [59]. Moreover, it is expected that these types of electrolyzers are slightly more capital intensive, due to the requirement of a pressure-regulator and more expensive manufacturing of the electrode.

- **Membrane electrode assembly** (Figure 2.8c):

  These types of cells use a solid-state polymer electrolyte, which can be chosen to either conduct protons (to form a proton exchange membrane electrolyzer (PEMEL)) or hydroxide ions (to form an anion exchange membrane electrolyzer (AEMEL)). In Figure 2.8c, the latter is shown. In this type of cell, the e-NRR again takes place on the TPB interface of the porous cathode, and therefore also has the potential to mitigate N_2 solubility problems. Due to a lack of liquid electrolyte, the formed product will move to the cathodic gas flow channel, yielding a product exit stream containing N_2, NH_3 and H_2 formed via the

parasitic HER.

The membrane can be made with low thickness, which can result in lower Ohmic resistances and the consequential ability to work at higher current densities. Nevertheless, literature mentions that PEMs such as Nafion suffer from problems with the cross-over of formed NH_3 over the membrane to the anode [36, 63]. NH_3 can also accumulate in the membrane, which significantly decreases its conductivity and makes PEM-type electrolyzers impractical to operate. Moreover, the accumulation of NH_3 has a role in the dehydration of the membrane, permanently degrading it over time [42]. As a result, anion-exchange membranes have a more interesting proposition for e-NRR NH_3 synthesis. However, anion exchange membranes have yet to reach commercial availability, and experience issues with stability as a result of structural degradation [36].

- **Solid oxide electrolyzer** (Figure 2.8d):

Figure 2.8d shows that the SOEL electrolyzer conducts protons from anode to cathode. The cell consists of two gas flow channels, steam is fed to the anode, and N_2 to the cathode. Again, NH_3 formation occurs at the TFB of the GDE cathode, and the produced NH_3 exits the cell via the cathodic gas flow channel.

The cell is operated at an elevated temperature, which increases e-NRR reaction kinetics. It is mentioned in literature that this type of electrolyzer can therefore achieve higher NH_3 production rates compared to its alternatives operating at room temperature [53]. Next to reaction kinetics, the temperature also has an effect on the reaction thermodynamics. In Appendix A.3, the effect of operating temperature on ΔH, ΔG and $T\Delta S$ for the e-NRR reaction are shown. Interestingly, the necessary electrical energy for e-NRR, ΔG, slightly increases at elevated temperature. Thus, the high temperature operation is accompanied by a larger required minimal cell potential (which is showcased in Figure A.2 in Appendix A.3).

These types of electrolyzers are applied in H_2O electrolysis, where they exhibit high electrical efficiencies due to the thermodynamics of HER (as was displayed in Figure 2.5). The SOEL's biggest pitfall has to do with the stability of the ceramic electrolyte. Upon heating and cooling, mechanical stability of the electrolyte is crucial, and still proves challenging. Moreover, since the thermodynamics of HER are more favourable at elevated temperatures compared to e-NRR, it is expected that high temperature operation has a destructive effect on the selectivity. Also, NH_3 decomposition limits e-NRR performance further.

3 Process Design for Electrochemical Ammonia Synthesis

The electrochemical synthesis of NH_3 from air and H_2O requires both pre-treatment and post-treatment steps. A simple process design is shown in Figure 2.9 below. This section aims to assess literature about the available up and downstream processing equipment, providing the reader with an idea about the machinery necessary to design a process for NH_3 production via e-NRR.
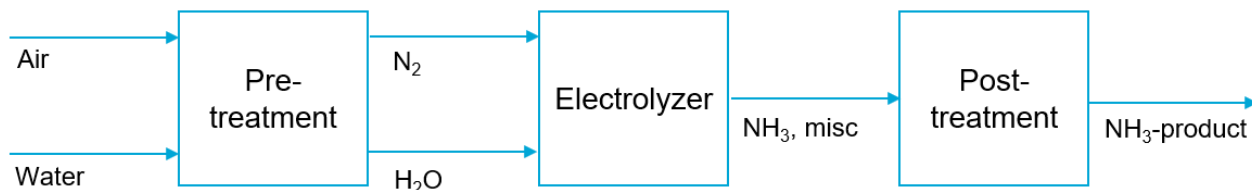
Figure 2.9: Simplified process flow diagram of the e-NRR process.

3.1 Pre-treatment

H_2O and air are the required raw materials for electrocatalytic NH_3 synthesis. These building blocks are available worldwide and in large supply, which is one of the merits of the e-NRR. This section explores different possibilities to extract N_2 from the air with low levels of contamination. The pre-treatment of H_2O was assumed out of scope.

3.1.1 Air Separation Unit

Air is made up of multiple components, of which the biggest contributors are nitrogen N_2 (78%), oxygen O_2 (21%) and argon Ar (0.9%). There are several technologies that are able to separate air into these pure components. Three commercially available technologies are cryogenic distillation, pressure-swing adsorption, and membrane-based processes. The applicability of these technologies depends on the capacity and required purity of the N_2 generation facility. It is expected that the membrane ASU cannot yield sufficient N_2 purity and is not included in the scope of this thesis.

Cryogenic Air Distillation

The industry standard ASU is cryogenic distillation (CAD), and accounts for more than 90% of N_2 production facilities [26]. It is an old and mature technology (first industrially applied in 1902), and uses differences in boiling points and condensation temperatures. The word *cryogenic* refers to the low operational temperatures, since the boiling points of O_2 and N_2 are -183 °C and -196 °C respectively. CAD can produce N_2 with high purity, approximately 99.9999%, and is usually applied for large scale projects (at least 500 t_{N_2} d^{-1} [26]) in order to benefit from economies of scale. The typical capacity range extends up to 5,000 t_{N_2} d^{-1}, and the largest existing N_2 plant located in Cantarell Mexico is capable of producing 10,000 t_{N_2} d^{-1} [64].

There are two main types of CAD processes: (1) the single column process and (2) the double column process [26]. The double column is conventionally used when purified N_2 and O_2 are both required. Since the electrolyzer only requires N_2, the single column process will be analysed further. A process flow diagram of the single column CAD process is illustrated in Figure 2.10a, which goes through the following steps:

- Atmospheric air is pumped through a filter (to remove dust particles) and pressurised to roughly 5-8 bar.

- Subsequently, the air is cooled through a heat exchanger and enters an air purification unit, where residual H_2O, CO_2 and other hydrocarbons are removed by thermal swing (Zeolite) adsorption. The stream leaving the adsorption unit is composed of mainly N_2 and O_2, and some Ar.

- This stream enters a refrigeration cycle, where it is cooled to cryogenic temperatures (roughly -185 °C).

- The cooled stream enters the distillation column. N_2 leaves the column at the top (due to its lower boiling point), and an O_2-rich stream (also containing Ar) leaves the column at the bottom. This stream is reboiled and re-fed to the column. The N_2 stream goes back through a heat exchanger, and is ejected from the system to the consumer.
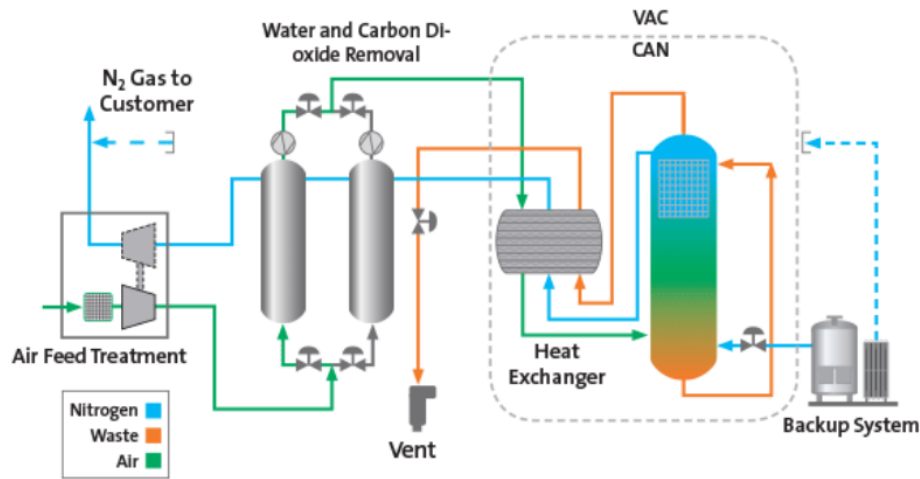
(a) Cryogenic air distillation
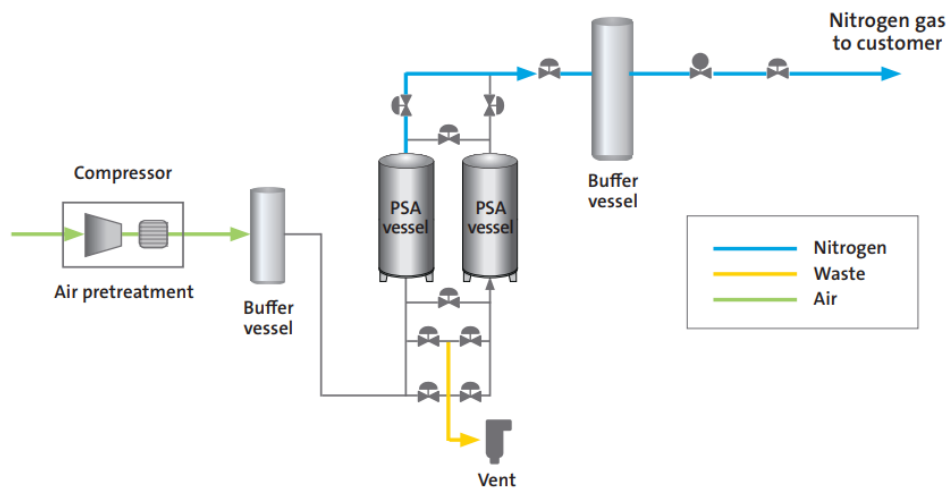
(b) Pressure swing adsorption

Figure 2.10: Process flow diagrams of different types of air separation units: (a) cryogenic air distillation and (b) pressure swing adsorption. Obtained from [65] and [66].

Pressure Swing Adsorption

A method for air separation that can be applied on smaller scales than CAD is pressure swing adsorption (PSA). In essence, PSA can be more cost-effective than cryogenic distillation at lower N_2 purity or capacities (lower than 500 t_{N_2} d^{-1} [67]). PSA systems operate on the basis of adsorption differences between the gas constituents. PSAs have a higher compatibility with an intermittent energy supply due to their switching capabilities because they can start-up and power down within minutes [67].

In Figure 2.10b, one can find an overview of the main unit operations with the main steps described below [66]:

- The air is compressed and filtered to remove excess water, dust, oil and other contaminants.

- The filtered air is fed into the adsorption column, where carbon-molecular sieves bind O_2. N_2 will not be adsorbed and moves towards the product stream. Once the carbon-molecular sieves of the first PSA unit are saturated with O_2, the gas stream enters the second unit, which allows the saturated first PSA to be depressurised thereby releasing the O_2. This O_2 rich stream is vented.

- The purified N_2 is stored in a buffer vessel, which is included to compensate for peaks and valleys of supply and demand.

3.2 Post-treatment

NH_3 is separated from the product stream in the post-treatment step. The exact composition of the product streams depends on the cell layout (Subsection 2.1, Figure 2.8). Figure 2.8 demonstrated that NH_3 leaves the electrolyzer either dissolved in the liquid electrolyte phase (for the AEL and GDE), or as a gas mixed with H_2 and N_2 (for the MEA and SOEL). Both options require different separation methods, as will be highlighted in this subsection.

3.2.1 Ammonia Distillation

A possible option to separate NH_3 dissolved in the aqueous electrolyte is distillation. In terms of industrial application, NH_3 separation via distillation is not particularly well developed, since no existing NH_3 production processes form a product stream with NH_3 dissolved in water. However, the boiling point of NH_3 (-33 °C) is far lower than that of H_2O (100 °C). Hence, a separation on the basis of boiling point like fractional distillation could be a viable option. A similar reasoning was carried out by Wang et al. [7], who included fractional distillation in their conceptual process design.

NH_3 readily dissolves in H_2O because NH_3 and H_2O form strong hydrogen (O-H) bonds [68]. This makes NH_3/H_2O mixtures difficult to separate. Furthermore, NH_3 is a weak base and can react with H_2O to ammonium-ions (NH_4^+) in acidic environments (Equation 2.21). Hence, working at high pH is required to minimise the formation of ammonium-ions.

$$NH_3(aq) + H_2O(l) \rightleftharpoons NH_4^+(aq) + OH^-(aq) \tag{2.21}$$

An alternative to distillation could be NH_3 stripping, as is often done in the de-ammonification of waste water streams [69]. In this approach, a reagent (a strong base like calcium hydroxide (lime) or sodium hydroxide (caustic)) is added to the aqueous mixture, which converts NH_4^+ to pure NH_3 gas, which can be collected and form a pure NH_3 stream. However, it is expected that a part of the NH_3 remains dissolved in the aqueous solution, so this method will yield low NH_3 recovery. It is also not possible to achieve sufficient NH_3 purity [69].

3.2.2 Ammonia Condensation

Condensation for the separation of gaseous NH_3 out of a mixture of N_2 and H_2 is commercially applied in HB. This separation technology relies on the differences in volatility of the components. In HB, the pressurised (around 140 bar) product stream is fed into a condensation drum which operates at low temperatures (around -33 °C) [70]. The refrigeration to -33 °C is achieved by either cooling water or a refrigeration cycle with NH_3 refrigerant [70]. The decrease in temperature condensates NH_3, which is liquefied, whereas N_2 and H_2 remain in the gas phase.
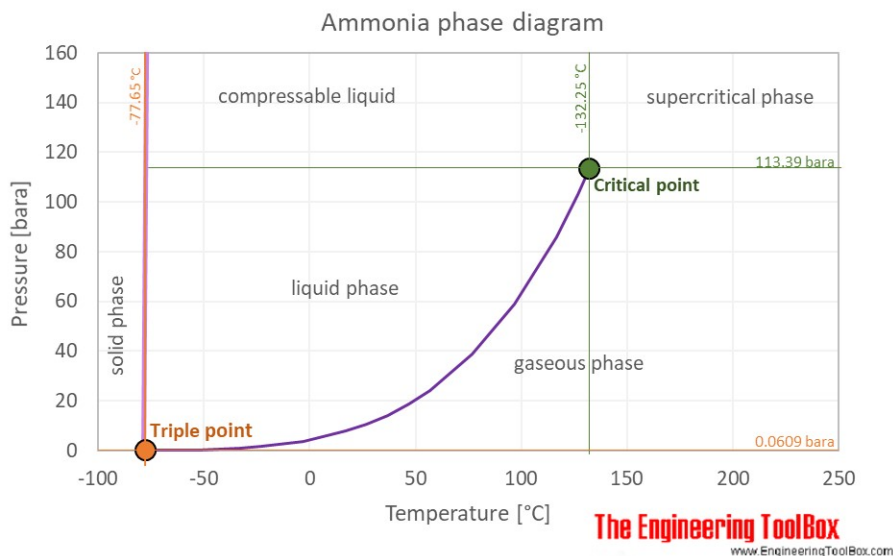
Figure 2.11: Ammonia phase diagram. Obtained from *The Engineering Toolbox* [71].

Electrochemical NH_3 synthesis via e-NRR works at ambient pressures. This changes the required condensation temperature, as can be seen in the phase diagram of NH_3 in Figure 2.11. Thus, to reach the same degree of separation as the condensation applied in HB, one must either first pressurise the stream, or use a refrigeration cycle to reach satisfactory NH_3 separation. The energy requirements for pressurising a gas do not scale linearly, hence applying condensation for NH_3 separation is not as simple for low temperature and pressure systems. Kugler et al. [72] modelled the application of pairing an e-NRR NH_3 synthesis process with downstream separation by condensation, and found that the energy input for constitutes approximately 8% of total energy demand, or 3.6 GJ t^{-1}.

Chapter 3

Method

This chapter explains the methodology used to design several conceptual processes for electrochemical NH_3 synthesis via e-NRR. These processes are distinguished based on three specific scales and electrolyzer types to investigate the techno-economic compatibility of e-NRR NH_3 synthesis compared to HB as a benchmark. The three scales are: small (91 t d^{-1}), medium (544 t d^{-1}), and large (2055 t d^{-1}), which were chosen based on existing SMR-HB plants (Fortigen plant in Nebraska [73], Simplot plant in Wyoming [74] and Yara/BASF plant in Texas [74]). For each scale, three different types of electrolyzers were evaluated: the AE, the GDE and the SOEL. These types are chosen based on several studies reporting promising NH_3 performance metrics [54, 36], and industrial applicability in the H_2O-electrolysis field.

The process design approach presented in this thesis primarily aims to include unit operations that are commercially applied. An advantage of this approach is that sufficient literature is available, which means that mass and energy balances can be solved in Excel. However, not all required process steps are applied in industry, so Aspen Plus V.12 (referred to as Aspen) is used to model these. Aspen is a powerful tool due to its ability to accurately simulate complex chemical systems, but has an inherent uncertainty margin and requires validation.

This chapter begins by evaluating the design choices and modelling assumptions for the electrolyzer (Section 1), pre-treatment (Section 2) and post-treatment (Section 3). Following this, the conceptual process designs for the different electrolyzer types are presented in Section 4. Then, Section 5 presents the method for the economic review. At last, Section 6 summarises the most relevant model parameters.

1 Electrolyzer

1.1 Electrolyzer Choice

A large body of research on e-NRR focuses on the AEL [36], which is the first interesting candidate for NH_3 production due to its simple layout and extensive application and resulting know-how from the field of water electrolysis [35]. However, aqueous solvents are limited by poor N_2 solubility, resulting in mass transfer issues and low product concentrations. This can be circumvented by the application of a gas diffusion electrode in the GDE [59, 60, 61]. It would be interesting to compare the compatibility of GDE systems and the AEL. The third and final type of electrolyzer is a SOEL operating at high temperature (>500°C), which can theoretically aid in N_2 activation and is also used in high temperature H_2O-electrolysis.

Alternatively, an electrolyzer using a membrane electrode assembly (MEA) receives significant research attention. Nevertheless, MEAs are not included in the scope of this research, owing to several concerning factors: 1) protonic MEA cells are expected to significantly suffer from product crossover due to the diffusion of NH_3 through cation selective Nafion membranes; 2) NH_3 is lost through oxidation at the anode; and 3) NH_3 accumulation in the membrane decreases its ionic conductivity [63]. Furthermore, anion-exchange membrane (AEM) cells could solve this problem, but lack a stable commercial membrane material.

1.2 Alkaline Electrolyzer

Process input for the AEL was based on the commercial Nel Hydrogen A3880 H_2O-electrolyzer [75]. It operates at 80 °C to improve KOH conductivity whilst minimising water evaporation, and atmospheric pressure (P = 1 bar). The electrolyte is a 25 wt% KOH solution. The AEL was modelled as a black-box, of which schematic representation is shown in Figure 3.1. The model assumed a parallel stack design with a single pass conversion

(χ_{N_2}) of 10%. χ_{N_2} is defined as the percentage of N_2 molecules that are able to dissolve into the electrolyte, diffuse to the electrode, and react to NH_3. The assumed χ_{N_2} is in line with earlier reported models (5-30% [22], 5-25% [7]).
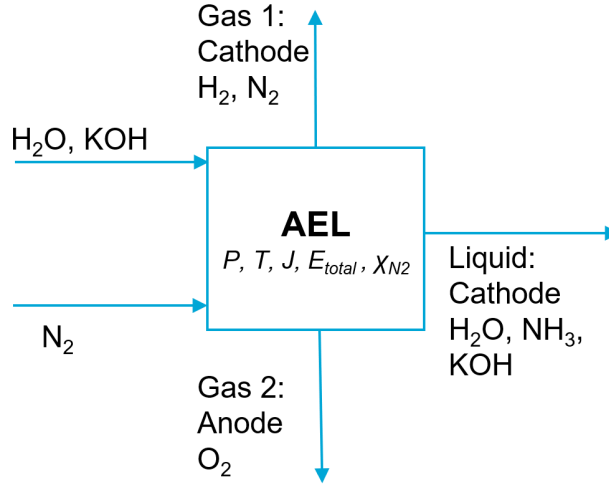
Figure 3.1: Schematic representation of inflows and outflows of the black-box AEL

Figure 3.1 displays that two streams enter the electrolyzer, a liquid electrolyte (H_2O and KOH) and a gaseous N_2 stream. The N_2 is bubbled into the electrolyte, where a fraction (0.864 mmol%) of it dissolves. N_2 is converted to NH_3, which is assumed to directly dissolve in the electrolyte. The electrolyzer is separated in an anodic and cathodic compartment, assumed to be perfectly separated by a separator (Zirfon). So, the anodic exit stream is pure O_2 and the cathodic exit stream is a mixture of N_2 and H_2. Furthermore, it is assumed that all dissolved N_2 is converted so the liquid outflow only contains NH_3, H_2O and KOH.

The NH_3 production rate (r_{NH_3}), as well as the reaction rate of the HER (r_{H_2}) and OER (r_{O_2}), and the reaction rates of the reactants (r_{N_2} and r_{H_2O}) are based on Faraday's law and the reaction stoichiometry. They are described by the following set of equations:

$$r_{NH_3} = FE \cdot \frac{I}{F \cdot z_{NRR}} \tag{3.1}$$

$$r_{H_2} = (1 - FE) \cdot \frac{I}{F \cdot z_{HER}} \tag{3.2}$$

$$r_{O_2} = 0.75 \cdot r_{NH_3} + 0.5 \cdot r_{H_2} \tag{3.3}$$

$$r_{H_2O} = -1.5 \cdot r_{NH_3} - r_{H_2} \tag{3.4}$$

$$r_{N_2} = -0.5 \cdot r_{NH_3} \tag{3.5}$$

where:
r_i = the production rate in mol s^{-1} for component i.
FE = the Faradaic efficiency.
F = the Faraday constant.
z_{NRR} = the number of electrons in NRR.
z_{HER} = the number of electrons in HER.

The primary design parameter of the electrolyzer is the NH_3 production rate, r_{NH_3}, which is chosen to yield a specified NH_3 product capacity (2055, 544 and 91 t d^{-1}). The FE was used to determine the required current (I) that matches this r_{NH_3}. The DoE REFUEL [13] program estimates an optimistic value of 95% for the FE, which is not realistic for the inherent HER competition in e-NRR systems. The highest FE towards NH_3, without the possibility of false positives, is 66% [76], as was found by the review paper by Choi [77]. Hence, for the base case, a value of 70% was assumed.

The base case current density (J) of the AEL, and for the other electrolyzer types, is fixed at 0.3 A cm^{-2} [13]. The current density plays a large role in sizing the electrolyzer, as it directly determines the required electrode area (A_e), which is an important parameter in the capital expenditure of process.

The power consumption (P_{cell}) of the cell was determined by multiplying the required current (I) and the cell potential (E_{total}). The base case cell potential of the AEL is approximately 2.2 V, which is the sum of anode activation overpotential ($\eta_{act,an}$), cathode activation overpotential ($\eta_{act,cat}$), separator resistance ($\eta_{Ohm,mem}$), electrolyte resistance ($\eta_{Ohm,el}$), and the thermodynamic reversible cell potential (E_{cell}). The latter is determined at 80 °C through Nist data, as shown in Appendix A.3, Figure A.2. Table 3.1 below summarises the contributions of the cell potential.

Table 3.1: Base case assumptions of AEL cell potential.

Parameter	Value	Unit	Assumptions	Reference
$\eta_{act,an}$	0.3	V	n.a.	[50]
$\eta_{act,cat}$	0.6	V	n.a.	[46]
$\eta_{Ohm,mem}$	0.02	V	Zirfon, 0.05 cm thickness	[78]
$\eta_{Ohm,el}$	0.12	V	1 cm gap, 80 °C	[79]
E_{cell}	1.146	V	80 °C	[80]
E_{total}	2.2	V		

1.3 Gas Diffusion Electrode Flow Cell

The GDE is similar to the AEL. It operates under the same operation conditions as the AEL (80 °C, 1 bar), and has a parallel stack design with χ_{N_2} equal to 10%. r_{NH_3} and I were calculated through Equations 3.1 to 3.5. Figure 3.2 shows a schematic representation of the internal structure of the GDE, and is based on the design stipulated by Kolen et al. [59]. The cathodic and anodic compartment are separated by a membrane and contains a flowing 25 wt% KOH electrolyte. The cathode is replaced by a gas diffusion electrode, which allows gas permeation from an additional gas compartment towards the interphase between the gas, electrocatalyst and electrolyte. As has been evaluated in Section 2.2, the GDE does not require dissolution of N_2. Rather, N_2 and OH^- react on the triple phase boundary on the electrode. It is assumed that NH_3 dissolves directly into the liquid electrolyte after it has been formed [59]. H_2 does not dissolve, due to its much lower solubility. Hence, H_2 will permeate through the GDE and enter the cathodic gaseous exit stream.
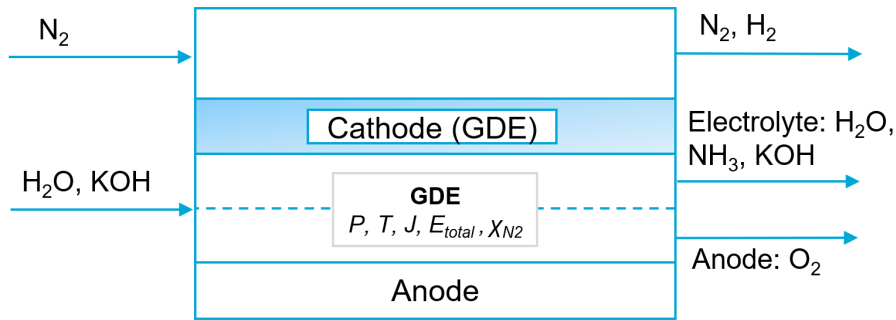
Figure 3.2: Schematic representation of the internal structure of the GDE. Based on the cell design of Kolen et al. [59].

For the GDE cell, the E_{total} is again determined as the sum of anodic and cathodic activation overpotentials, electrolyte resistance, membrane resistance, and the thermodynamic reversible cell potential. A Sustainion 37-50 membrane is assumed as the separator with a 0.05 cm thickness and 0.08 S cm^{-1} conductivity [81]. The electrolyte conductivity was calculated for 25 wt% KOH, with a channel thickness of 0.3 cm (based on [82]). The results are summarised in Table 3.2 below, with an E_{total} of approximately 2.3 V for the base case.

1.4 Solid Oxide Electrolyzer

The SOEL model is based on an Yttrium Stabilised Zirconia (YSZ) electrolyte similar to what is currently the best available technology for high temperature H_2O-electrolysis. These types of electrolytes can conduct oxide ions (O^{2-}) or protons (H^+), with the highest O^{2-} conductivity at temperatures above 700 °C [58]. However, NH_3

Table 3.2: Base case assumptions of GDE cell potential.

Parameter	Value	Unit	Assumptions	Reference
$\eta_{act,an}$	0.3	V	n.a.	[50]
$\eta_{act,cat}$	0.6	V	n.a.	[46]
$\eta_{Ohm,mem}$	0.19	V	Sustainion, 0.05 cm thickness	[81]
$\eta_{Ohm,el}$	0.07	V	0.3 cm gap, 80 °C	[79], [82]
E_{cell}	1.146	V	80 °C	[80]
E_{total}	2.2	V		

decomposition becomes spontaneous above 400 °C, hence working at or above 700 °C is not desired. In reality, most SOELs for NH_3 operate at 550 °C [53, 51], which is chosen as the operating temperature. Therefore, it is assumed that YSZ conducts protons.

The black-box model of the SOEL with the in- and outflows is illustrated in Figure 3.3. It is assumed that all H_2O fed is completely converted, which leaves a pure and marketable O_2 stream from the anode. Pre-heated N_2 is fed at the cathode side, where it is activated and reacts with H^+ to NH_3. Again, the production of H_2 is inevitable and forms a mixture with unreacted N_2 due to an assumed single pass conversion of 10%.

Moreover, produced NH_3 will undergo decomposition. This is modelled as a separate mass balance, where it is assumed that 10% of produced NH_3 is converted to H_2 and N_2. Literature found that at 570 °C, NH_3 decomposition was less than 20% [83], which could go below 10% at industrially relevant flow rates. So, 10% conversion of NH_3 to H_2 and N_2 is assumed.
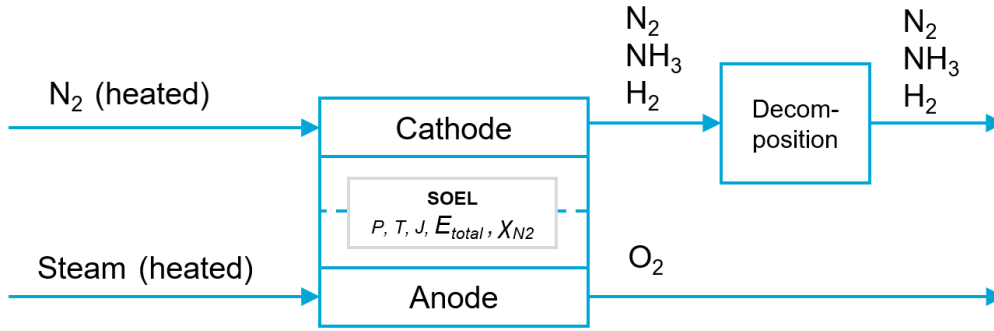
Figure 3.3: Schematic representation of inflows and outflows of the black-box SOEL.

Theoretically, high temperature electrolyzers do not need to be heated if the cell potential is above the thermo-neutral potential [84]. Electrical energy loss via the overpotential is converted into heat, which can sustain the SOEL temperature at 550 °C.

The cell potential contributions are summarised in the table below. Note that the reversible cell potential is calculated for e-NRR at 550 °C (Appendix A.3, Figure A.2).

Table 3.3: Base case assumptions of SOEL cell potential.

Parameter	Value	Unit	Assumptions	Reference
$\eta_{act,an}$	0.3	V	n.a.	[50]
$\eta_{act,cat}$	0.6	V	n.a.	[46]
$\eta_{Ohm,el}$	0.015	V	0.02 mm thickness, 550 °C	[85]
E_{cell}	1.09	V	550 °C	[80]
E_{total}	2.2	V		

2   Feed Pre-treatment

Electrolyzers desire high purity feed streams to avoid unwanted side reactions (e.g. O_2 reduction) or catalyst deactivation (e.g. trace metals). This section focuses on the supply of N_2 through air separation systems (ASU) (Section 2.1), and the pre-heating steps (Section 2.2). The purification of water is assumed outside the scope of this research.

2.1 Air Separation Unit

Two commercial ASUs were considered: cryogenic air distillation (CAD) and pressure swing adsorption (PSA). Due to their industrial maturity, the choice was made to base the performance of the ASU on industrial heuristics rather than modelling in Aspen. It is assumed that data from industry is more reliable than Aspen simulations.

The mass and energy balances of the two types of ASUs were calculated based on inputs of N_2 recovery (Y_{N_2}), N_2 purity (y_{N_2}) and ASU energy consumption (P_{ASU}). A schematic representation of the ASU process flow diagram is illustrated in Figure 3.4. The electrolyzer requires r_{N_2} to generate the specified r_{NH_3}. The capacity of the ASU is calculated by dividing r_{N_2} by χ_{N_2}. The air feed is assumed 22 mol% O_2 and 78 mol% N_2 at 1 bar and 25 °C, the presence of argon and other compounds is neglected. A N_2 purity of 99.9% is assumed, which is achievable by industrial CAD and PSA systems [26].
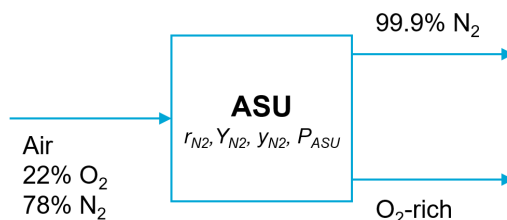
Figure 3.4: Schematic representation of the ASU model.

The design choice for the ASU of either CAD or PSA depends on the specified N_2 capacity. Table 3.4 shows the capacity limitations of each ASU technology based Sánchez et al. [86], as well as assumptions for y_{N_2}, Y_{N_2} and P_{ASU} which are taken from [26]. The PSA was selected for small scale (<500 t_{N_2} d^{-1} or 91 t_{NH_3} d^{-1} with recycle), and CAD for all larger scales.

Table 3.4: Overview of design choice and model assumptions for air separation. Based on Sánchez et al. [86] and *Ullman's Encyclopedia of Industrial Chemistry* [26]

N_2 capacity (t_{N_2} d^{-1})	ASU choice	y_{N_2} (%)	Y_{N_2} (%)	P_{ASU} (GJ $t_{N_2}^{-1}$)
>5000	Double column CAD	99.9	70	0.288
500-5000	Single column CAD	99.9	40	0.576
<500	PSA	99.9	90	0.864

2.2 Pre-heating

For the GDE and AEL, modelling of pre-heating of N_2 is done via an Aspen heater block. A steam heat exchanger design was assumed that takes steam at 7 bar and 170 °C as the heating medium to pre-heat the reactants to 80 °C. The steam requirement (utility) was imported from outside the battery limits of the plant.

For the SOEL process, the N_2 feed has to be heated to 550 °C, which is not possible with steam heat exchangers [87]. To pre-heat the N_2 feed, an electric heater was implemented with 80% efficiency. For the formation of steam at 550 °C, a steam boiler is applied with 80% efficiency.

3 Post-treatment

NH_3 leaving the battery limits must have a commercial grade purity (99.5%) [88]. The composition and phase of the product stream differs with different electrolyzers, hence the appropriate post-separation technology will also vary. In the AEL and GDE, the NH_3/H_2O mixture is separated via distillation, for which the modelling assumptions are elaborated in Section 3.1. For the SOEL process, a product gas mixture of NH_3, N_2 and H_2 will be separated by condensation (Subsection 3.2), similar to what is done in HB. At last, the exit stream with H_2/N_2 mix can be further separated with PSA to sell H_2 as a value adding by-product and recycle N_2 (Subsection 3.3).

3.1 Distillation

NH_3 distillation from a 25 wt% aquous KOH solution is modelled in Aspen, using the NRTL-RK equations of state, in a RADFRAC block. A screenshot of the Aspen simulation is shown in Figure 3.5.
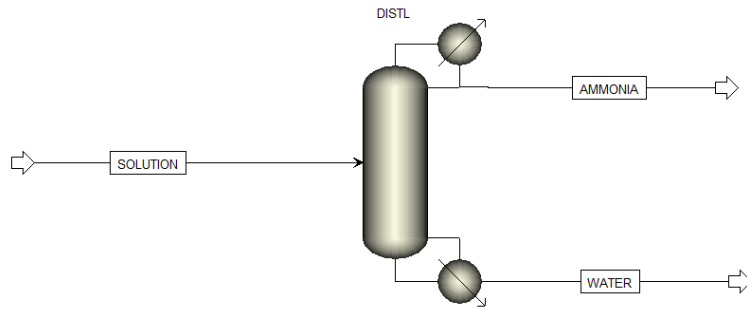
Figure 3.5: Screenshot of the Aspen simulation of the distillation of NH_3 from the alkaline electrolyte.

The effectiveness of the distillation is strongly influenced by the NH_3 concentration [89]. Therefore, a sensitivity analysis was performed by varying the NH_3 liquid fraction between 2-15 mol% to reach optimal column specifications. The values of the optimised column parameters reflux ratio (RR), distillate to feed ratio (DF), number of stages (N) and feed stage location (LOC) for different NH_3 concentrations (c_{NH_3}) are shown in Table 3.5. These calculations were done for a constant NH_3 recovery of 99.5 %, and a purity of 99.5%. It was concluded that separation at lower NH_3 concentrations will be more capital and energy intensive. The minimal c_{NH_3} for distillation to be economically viable was chosen at 10 mol%, resulting in an energy consumption of 6.97 GJ t^{-1}.

Table 3.5: Optimised column parameters and distillation energy consumption (GJ t^{-1}) for NH_3 distillation at decreasing NH_3 concentrations.

c_{NH_3} (mol%)	RR	DF	N	LOC	Duty (GJ t^{-1})
15	1.66	0.15	14	5	6.06
10	1.57	0.1	22	5	6.97
5	2.07	0.05	25	5	10.7
4	2.54	0.04	32	7	12.6
2	4.95	0.02	40	10	21.9

3.1.1 Product Accumulation

Owing to the low solubility of N_2 in water, the steady state NH_3 concentration in the product stream of the AEL is incredibly low ($4.7 \cdot 10^{-4}$ mol%). To increase c_{NH_3}, the electrolyte was recycled untill the NH_3 concentration reaches 10 mol% (Figure 3.6). Electrolyte leaving the electrolyzer enters a splitter, where the product stream is split into a recycle and product stream. The recycle stream re-enters the electrolyzer, where more NH_3 is added (r_{NH_3} is assumed constant and no NH_3 is oxidised). After some time, the system reaches steady state with increased product concentration. The split fraction (SF) is defined as the percent of mass flow that leaves the splitter as the NH_3 product stream, and determines the NH_3 concentration in the product stream. As a higher fraction of electrolyte is recycled (which is the case at low SF), a larger steady state product concentration can be achieved.

This accumulation system was iterated for many split fractions and it was found that at SF = $1.4 \cdot 10^{-4}$, the system electrolyte is passed 7060 times through the electrolyzer and the NH_3 concentration equals to 10 mol%.
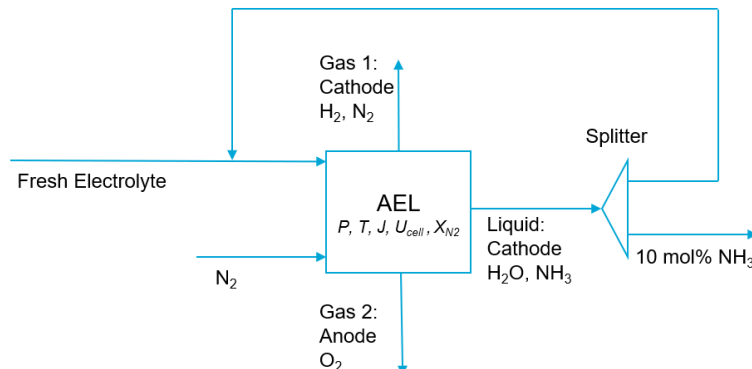
Figure 3.6: Schematic representation of product accumulation in the AEL process.

3.2 Condensation

NH$_3$ separation by condensation generally occurs at high pressures in the HB synthesis loop [70]. However, the product gas stream leaving the SOEL is 1 bar, hence different temperatures and pressures are required to achieve a similar or even higher NH$_3$ recovery rate. To investigate the relationship between operating pressure and temperature, flash condensation was modelled in Aspen, of which a screenshot is shown in Figure 3.7. The pre-compressor and cooling blocks determine the flash duty and have been modelled separately to obtain the total duty. The model in Aspen assumes the Peng-Robinson equations of state.
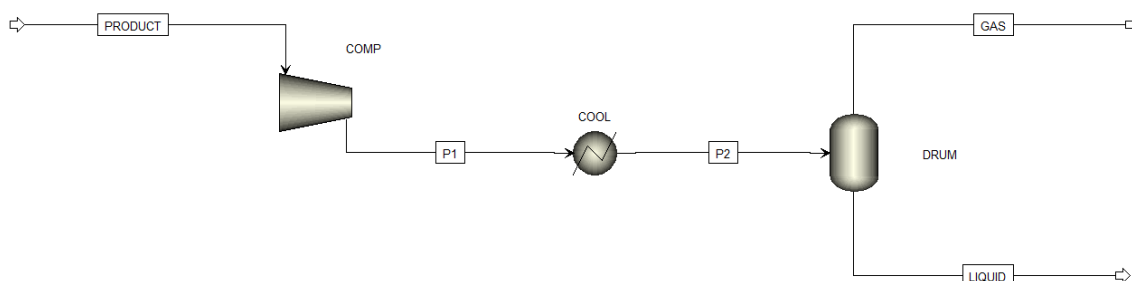
Figure 3.7: Screenshot of Aspen simulation of NH$_3$ condensation in SOEL process.

The equilibrium condenser temperature for 91% recovery and 99.5% purity at different pressures was calculated in order to find the optimal flash conditions for the atmospheric SOEL product stream (shown in Table 3.6).

Table 3.6: Equilibrium condensation pressure and temperature for NH$_3$ (14.4 mol%) condensation at 91% recovery and 99.5% purity.

P (bar)	T (°C)
1	-92
12	-64
23	-56
34	-52

The energy consumption of the condensation system was determined from the sum of pre-compressor and cooling duties. The duty of the compressor was calculated by Aspen, which assumes 72% isentropic efficiency by default. It proved most energy efficient to execute the condensation at 1 bar and -92 °C. With pre-compressor duty equal to zero, condenser duty consisted solely of the refrigeration cycle. The (reversed Carnot) refrigeration cycle energy duty was calculated by first selecting an appropriate refrigerant based on data from *Chemical Process Design and Integration* from Smith [90]. With the operating temperatures of the refrigerant and assuming a heat exchanger minimal temperature difference of 10 °C, the ideal Coefficient of Performance (COP) was calculated through Equation 3.6 below. The temperature of the cold medium (T_C) was determined by adding the minimum temperature difference to the required refrigeration temperature. The temperature of the hot medium (T_H) was chosen based on the maximum stable temperature of the refrigerant [90]. The energy consumption of the refrigeration cycle is subsequently determined by the shaft work of the compressor in the refrigeration cycle.

$$COP_{ideal} = \frac{T_C}{T_H - T_C} \tag{3.6}$$

where:
COP_{ideal} = the ideal COP.
T_H = temperature of the hot medium (heat ejection temperature).
T_C = temperature of the cold medium.

The refrigeration cycle shaft work (W_S) was found by dividing the Aspen-calculated cooling energy (Q_C) by the ideal COP, as shown in Equation 3.7 below. The real shaft work is determined by assuming 72% isentropic compressor efficiency.

$$W_S = \frac{Q_C}{COP_{ideal} \cdot \eta_{compressor}} \tag{3.7}$$

where:
W_S = ideal shaft work of refrigeration cycle
Q_C = theoretical cooling energy, equal to enthalpy change
$\eta_{compressor}$ = isentropic efficiency of cooling cycle compressor.

This resulted in an energy consumption of 5.23 GJ t^{-1} for the SOEL's 14.4 mol% NH_3 product concentration.

3.3 Hydrogen Isolation

At last, H_2 can be further separated from the H_2/N_2 mixture by pressure swing adsorption (PSA). It was found in literature that for a system with a H_2 concentration of 60 mol%, a PSA system with 55% H_2 recovery and 99.97% H_2 purity (fuel cell grade) is available [91]. The PSA system works between 7-9 bar and 20 °C. The energy consumption of the PSA system was determined by the compression energy and cooling energy, which cools the gasses to PSA conditions after compression. Again, compressor energy is calculated in Aspen with 72% isentropic efficiency.

3.3.1 Hydrogen Accumulation

As mentioned, the H_2 concentration of the gas stream needs to be at least 60 mol%, whereas the base case concentration was found 12.5 mol%. A continuous accumulation system similar to that shown in Figure 3.6 with 11.5 accumulations was applied to reach 60 mol%.

4 Process Flow Diagrams

One can find the base-case process flow diagrams (PFD) of the AEL, GDE and SOEL processes in Figure 3.8 on page 29. There are several things to clarify:

- *H_2/N_2 separation*: Due to the co-production of H_2, the idea was presented to isolate this from the cathodic gas stream to sell it as a value adding side product. To determine whether this is economically attractive, the process containing a PSA system (Figure 3.8b) is compared to a simpler system where the cathodic gas stream is purged (Figure 3.8c). This was executed for the GDE process, since the cathodic gas stream is physically separated from the liquid stream by the electrode. Thus, note that there are two distinct processes for the GDE, the GDE PSA process and GDE purge process.

- *Accumulation*: In the AEL and GDE PSA processes, an accumulation loop is added to increase NH_3 and H_2 concentration. The triangular blocks in Figure 3.8a and 3.8b represents a stream splitter that recycles part of the product streams.

- *Air Separation Unit*: as mentioned in Section 2, the process is equipped with CAD or PSA unit based on the N_2 capacity of the process. All of the presented processes use CAD, expect for the processes presented in Figure 3.8b. This is caused by the decreased N_2 needs due to the inclusion of a N_2 recycle stream.

5 Economics of Chemical Process Design

The process economics were expressed in US $, and brought to the value of 2022 through the Chemical Engineering Plant Cost Index (CEPCI) indexes via Equation 3.8 below.

$$\frac{C_1}{C_2} = \frac{INDEX_1}{INDEX_2} \tag{3.8}$$

where:
C_1 = cost of component in year 1.
C_2 = cost of component in year 2.
$INDEX_1$ = CEPCI price index in year 1.

(a) AEL process

(b) GDE PSA process

(c) GDE purge process
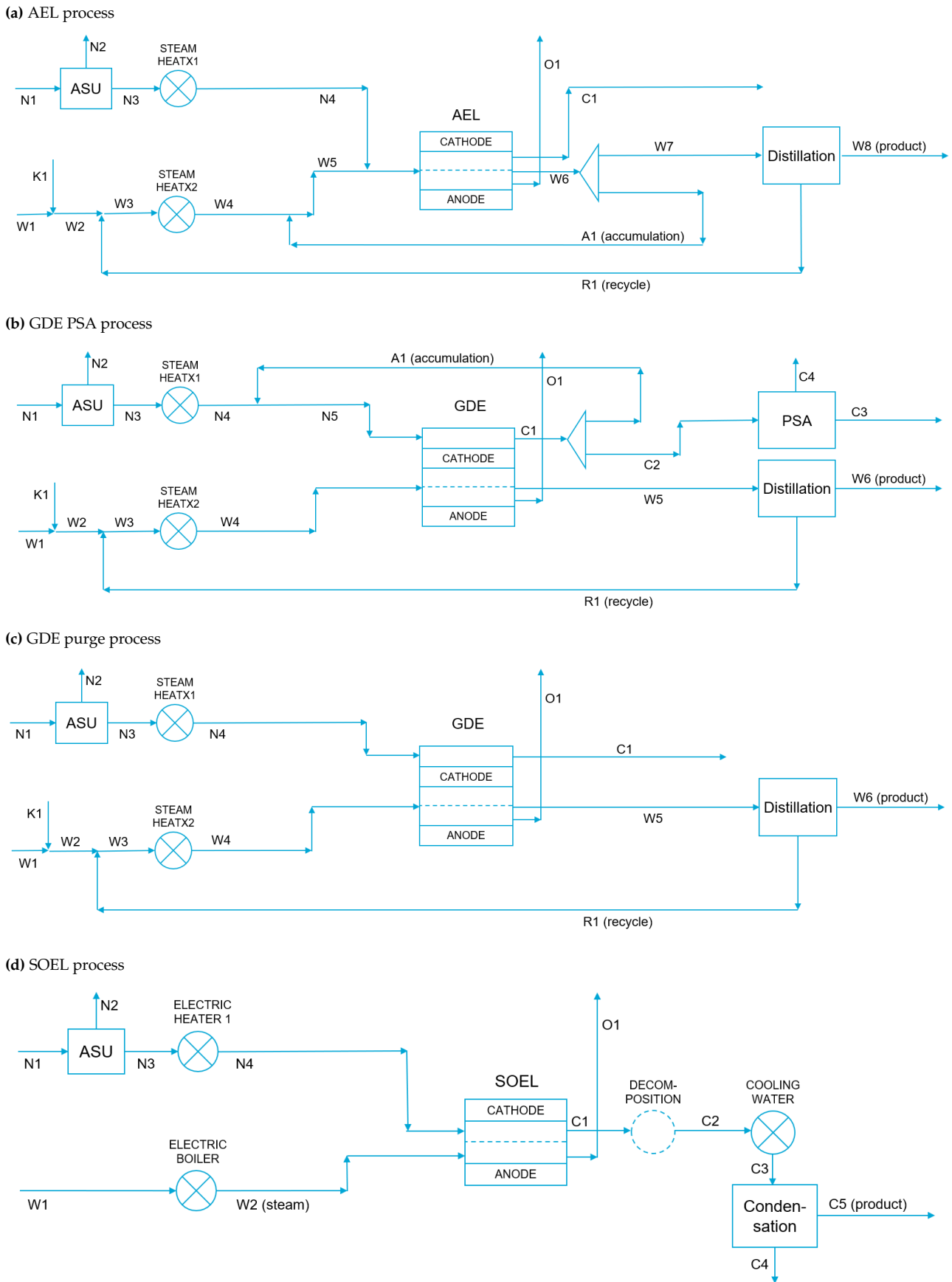
(d) SOEL process

Figure 3.8: Process flow diagrams of the base-case scenarios for the different electrolyzer types (a) AEL process, (b) GDE with H_2 isolation (GDE PSA process), (c) GDE without H_2 isolation (GDE purge process) and (d) SOEL process.

$INDEX_2$ = CEPCI price index in year 2.

The economics of chemical processes can be split into two parts, Capital Expenditure (CAPEX) and Operational Expenditure (OPEX), which will be elaborated in Section 5.1 and 5.2 respectively. The Levilized Cost of Ammonia (LCOA) and Capital Intensity (CI) are discussed in Sections 5.3 and 5.4.

5.1 CAPEX Evaluation

The capital costs are be broken down into three main parts: (1) equipment cost (i.e. all components to form a functioning process from raw materials to products), (2) installation costs and (3) indirect costs. Equipment costs are calculated based on scaling laws of existing equipment, and multiplied with a temperature factor (f_T) (for the SOEL process) [92]. Installation factors ($f_{inst,i}$) are dependent on the type of equipment and were adopted from Smith [92] and Hand' factors [93]. Indirect costs factors ($f_{ind,i}$) consist of contingency (unforeseen expenses) contributions [92]. The total capital expenditure of individual equipment parts ($C_{TFC,i}$) is calculated based on literature reported scaling laws and multiplication factors (ref. [92], [93] and [94]) via Equation 3.9 below.

$$C_{TFC,i} = C_{B,i}(\frac{Q_i}{Q_{B,i}})^{M_i} f_{T,i} f_{inst,i} f_{ind,i} \tag{3.9}$$

where:
$C_{TFC,i}$ = total final CAPEX for component i with capacity Q.
$C_{B,i}$ = known base cost for component i with capacity Q_B.
M_i = scaling factor for component i.
$f_{T,i}$ = correction factor for temperature of component i.
$f_{inst,i}$ = installation factor of component i.
$f_{ind,i}$ = indirect cost factor for unforeseen (contingency) costs of component i.

The total final CAPEX was found by summing the individual components (Equation 3.10):

$$C_{TFC} = \sum_i C_{TFC,i} \tag{3.10}$$

where:
C_{TFC} = total final CAPEX of the process.
$C_{TFC,i}$ = total final CAPEX of component i.

5.1.1 Equipment Cost Estimation

The equipment cost of the unit operations was divided into *regular chemical equipment* (e.g. heat exchangers, compressors, coolers, ASU), *electrolyzer equipment* and *specialist equipment* (e.g. NH$_3$ distillation and low pressure condensation), and was estimated as follows:

1. *Regular chemical equipment:* The CAPEX of the ASU, compressors, coolers and heat exchangers were obtained from literature due to their application in existing industry.

   For the CAD it is assumed that the cost follows the *six-tenths* scaling rule (M_{CAD} = 0.6) [86]. The equipment cost for CAD was obtained from Morgan [95] and adjusted with the scaling law. The PSA ASU cost were estimated on the basis of linear scaling (M_{PSA} = 1) [86] and taken from Bañares [96].

   The cost of steam heat exchangers for the AEL and GDE pre-heating are based on [92] and scaled based on the heat exchange area (calculated by Aspen), with a scaling factor of 0.68.

   Compressor cost are estimated based on shaft work duty, where the base cost and scaling factor (M_{comp} = 0.46) are again taken from [92].

   For the SOEL process, electric conduction heaters are required, of which the equipment cost and scaling factors were adopted from [94].

   For NH$_3$ condensation, it is assumed that the most important equipment costs are the refrigeration cycle: specifically the compressor and the heat exchanger, which are calculated from [92].

2. *Electrolyzer equipment*: The cost of the different types of electrolyzers was based on state-of-the art H_2O-electrolyzers. The report by *Clean Hydrogen Joint Undertaking* [97] mentions different scenarios for H_2O-electrolyzer equipment costs in $ kW^{-1}. Via the electrolyzer footprint (kW m^{-2}), the cost per m^2 of electrode was calculated. This approach is similar to Ramdin et al. [62].

   The AEL and SOEL electrolyzer cost are estimated at 7,800 $ m^{-2} and 15,937 $ m^{-2} respectively [97]. The GDE cost is estimated in the middle of the AEL and SOEL, at 11,868 $ m^{-2} since it does not require expensive solid oxide electrolytes but does need the application of a more expensive GDE electrode and pressure equalisation equipment.

   All electrolyzers are expected to exhibit linear scaling ($M_{el} = 1$) behaviour and due to higher degrees of uncertainty, the contingency cost are estimated based on 20% of electrolyzer cost instead of the 10% used for the other types of equipment. The electrolyzer CAPEX was validated for applicability to e-NRR systems by comparing them to other examples of techno-economic research about e-NRR NH_3 synthesis. These papers assumed lower electrolyzer costs, as can be observed in Table 3.7. Due to the lack of industrial data on e-NRR NH_3 electrolyzer prices, H_2O-electrolyzer prices function as an industrially-inspired base cost.

Table 3.7: Electrolyzer cost assumptions from this paper, compared to other techno-economic e-NRR literature.

Reference	Electrolyzer type	Cost ($ m^{-2})
This research	AEL	$ 7,800
This research	GDE	$ 11,868
This research	SOEL	$ 15,937
Fernandez et al. [23]	PEM	$ 200-300
Wang et al. [7]	GDE	$ 1,000-3,000

3. *Specialist equipment*: The capital expenditure of Aspen-simulated equipment (i.e. NH_3 distillation and condensation) is estimated using Aspen Economic Analyzer. For post-treatment NH_3-distillation, this assumption can be validated by looking at Wang et al. [7], that applied a similar distillation process to execute NH_3/H_2O separation. Condensation energy consumption was validated by assessing HB NH_3 condensation.

Subsequently, all equipment costs were multiplied with the temperature (SOEL), installation ($f_{inst,i}$) and indirect cost factors ($f_{ind,i}$) to obtain the total final CAPEX (C_{TFC}).

5.2 OPEX Evaluation

The operating cost consist of five elements, listed below:

1. *Raw material costs*: The cost of air is assumed to be zero, and the cost of H_2O is taken from US Department of Energy data [98].

2. *Catalyst and consumed chemicals (other than raw materials)*: These cost depend on how often the catalyst needs to be regenerated, or certain solvents that degrade with the reactions. It is assumed that these cost are comparable to existing HB plants, and are defined per tonne of NH_3 as 5.4 $ t^{-1}.

3. *Utility operating cost*: This is the most relevant operational cost. The price of electricity is an important parameter and one of the most pronounced contributors to the operating cost of 'power-to-X' processes. The base-case electricity price is assumed as the December 2022 average of industrial electricity prices at 0.0863 $ kWh^{-1}, obtained from EIA [99]. Other utility cost contain the steam used for pre-heating in GDE and AEL processes, and cooling water for cooling in the SOEL process. The cost of these expenses are estimated using Aspen Economic Analyser.

4. *Labor cost*: The labour costs are estimated based on existing HB facilities. At 2055 t d^{-1}, the Yara/BASF plant has 35 workers. The 544 t d^{-1} plant from Simplot has 40, and the 91 t d^{-1} has 22. The average salary is assumed at 40 $ h^{-1} [100] and annual working hours are 1791 h y^{-1} [101].

5. *Maintenance cost*: the operations and maintenance costs are estimated at 3% of C_{TFC}, as recommended by [27].

The yearly OPEX is calculated as the sum of above components.

5.3 Levilized Cost of Ammonia (LCOA)

The LCOA is defined as the price at which NH_3 must be sold in order to break even at the end of the plant lifetime. In this research, this concept is used to compare e-NRR NH_3 synthesis versus HB. The LCOA is evaluated by calculating the NH_3 selling price at which the Net Present Value (NPV) of the project equals zero.

The NPV is defined as the sum of cash flows (CF) with the incorporation of the time value of money (money received now has a greater value than money received at a later point in the future, since money can be invested to earn returns). CF is defined as the revenue minus the expenses per year. It is assumed that in year 0, there is no NH_3 production and the CF is equal to the negative of the total CAPEX. In year 1, revenue is generated by selling NH_3 at a certain price, so revenue is calculated by multiplying the NH_3 capacity (t y^{-1}) by the price ($ t^{-1}). O_2 is also sold for a fixed price of 0.096 $ kg^{-1} [102]. For the GDE PSA process, H_2 is marketed for a price of 3.7 $ kg^{-1} [103].

The CF is calculated by subtracting the total OPEX from the revenue. The yearly CFs are converted to discounted cash flow (DCF) through Equation 3.11, and summed to yield the NPV via equation 3.12.

$$DCF_n = \frac{CF_n}{(1+i)^n} \qquad (3.11)$$

where:
DCF_n = discounted cash flow over year n.
CF_n = cash flow over year n.
i = nominal interest rate.
n = year.

$$NPV = \sum_n DCF_n \qquad (3.12)$$

The nominal yearly interest rate (i) is taken at 5% [7] and the lifetime (n) at 20 years [62]. The LCOA is found through an Excel goal-seek macro for NPV equals zero. Linear depreciation over 20 years with a salvage value of 25% of the equipment cost (depreciable CAPEX) [7] was assumed in order to estimate the taxable income. Taxes are are subtracted from the yearly CF, with a tax rate of 25% of taxable income [62].

5.4 Capital Intensity (CI)

The CI is a measure that expresses the amount of capital (CAPEX) required to produce a single unit of NH_3. It was obtained by first calculating the yearly capital expenditure through the *Capital Recovery Factor* (*CRF*) (Equation 3.13). *CRF* is defined as the fraction of total CAPEX that needs to be re-payed yearly, and considers i and n. Subsequently, the annualised CAPEX is divided by the annual NH_3 production capacity to obtain the project's capital intensity in $ t^{-1}.

$$CRF = \frac{i(1+i)^n}{(1+i)^n - 1} \qquad (3.13)$$

6 Base Case Summary

Table 3.8 summarises the most important values of electrolyzer and economic model inputs, to provide the reader with an overview of what has been established in the previous sections.

Table 3.8: Summary of essential base case assumptions of electrolyzer and economic parameters.

	Electrolyzers			Economics	
Parameter	AEL	GDE	SOEL	Parameter	Value
χ_{N_2} (%)	10	10	10	Elec. price ($ kWh^{-1})	$ 0.0863
FE (%)	70	70	70	n (years)	20
E_{total} (V)	2.2	2.3	2.1	i (%)	5
J (A cm^{-2})	0.3	0.3	0.3	Tax rate (% of profit)	25
Electrolyzer cost ($ m^{-2})	$ 7,800	$ 11,868	$ 15,937	Salvage value (% of CAPEX)	25
T (°C)	80	80	550		
P (bar)	1	1	1		

Chapter 4

Results and Discussion

This chapter analyses the results from the e-NRR conceptual process design models with the focus on energy consumption and the techno-economic analysis. At first (Section 1), the outcomes of the models with the base case assumptions will be explored. These assumptions are studied and optimised by a sensitivity analysis presented in Section 2, which can elucidate and indicate the most important process model parameters. At last, a techno-economic analysis with the optimised case will be discussed in Section 3, which is used to compare the feasibility of e-NRR with the SMR-HB benchmark.

1 Base Case

1.1 Energy Evaluation

The normalised energy consumption for the processes with integrated AEL, GDE and SOEL at the largest scale (2055 t d^{-1}) are shown in Figure 4.1. It was found that the energy consumption did not differ significantly with varying scale, so only the processes at the largest scale were used for this analysis. For the GDE, two scenarios were investigated: 1) integration of a PSA for the separation of H_2/N_2 for H_2 recovery and N_2 recycle (GDE PSA process); and 2) purging the gaseous product stream (GDE purge process). The PFD of the first option is shown in the *Method* in Figure 3.8b, and the second in Figure 3.8c.
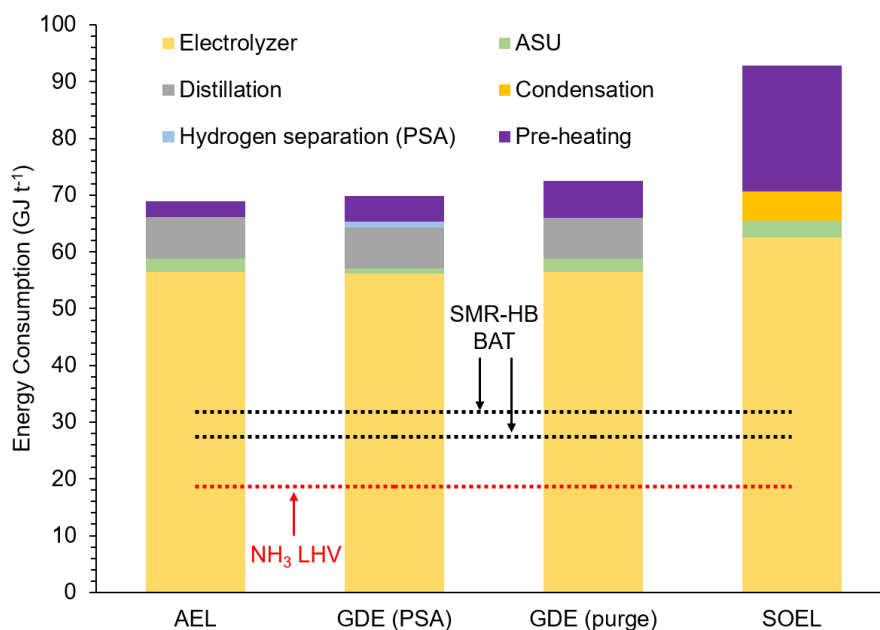
Figure 4.1: Energy consumption (GJ t^{-1}) contributions of different electrolyzer configurations, shown for the 2055 t d^{-1} scale. The SMR-HB BAT energy consumption is obtained from Smith et al. [5].

1.1.1 Total Energy Consumption

The total energy consumption of the AEL process (69.0 GJ t^{-1}) is the lowest. The GDE purge scenario was found slightly more energy intensive (6.4%) than the GDE PSA, as it lacks a N_2 recycle loop and therefore has a higher ASU duty. It was found that the recycle loop can save 2.6 GJ t^{-1} in purge losses. The SOEL process has with 92.8 GJ t^{-1} a considerably larger energy consumption. The reason for this is the additional feed pre-heating and a higher electrolyzer energy consumption per tonne, caused by NH_3 product loss by decomposition in the cell. Moreover, the energy efficiencies (EE_{LHV}) of the processes were evaluated and shown in Table 4.1. The AEL has the highest energy efficiency at 27.0%, followed by the GDE PSA (26.7%) and the GDE purge (25.7%), whereas the SOEL was found to be less energy efficient (20.1%).

In earlier reported techno-economic studies, the energy consumption of e-NRR is significantly lower than observed by this analysis (Figure 4.1), which is related to the difference in assumed base case model parameters. For instance, Wang et al. report an energy consumption between 50.0-51.9 GJ t^{-1} for AEL and SOEL processes assuming a FE of 90% with E_{total} is 1.8 V for the electrolyzer [7]. An ASU was not considered under the assumption that air was de-oxygenated by the combustion of the H_2 by-product. At last, NH_3 decomposition was neglected in their SOEL process. It is expected that if the authors included similar base-case assumptions, an ASU and NH_3 decomposition, their calculated energy consumption would be more comparable to our data.

1.1.2 Haber-Bosch Benchmark

According to the data presented in Figure 4.1, the base-case e-NRR energy consumption for all electrolyzer configurations was several times higher than the SMR-HB benchmark (BAT is 27.4-31.8 GJ t^{-1} [5]), which is primarily related to the energy losses in the electrolyzers. It was found that the electrolyzer consumes 56.2-56.5 GJ t^{-1} for the GDE and AEL processes (80-82% of the total), and 62.6 GJ t^{-1} in the SOEL process (74% of the total). The AEL and GDE operated at 33% energy efficiency, and the SOEL at 30% under the base case assumption, and therefore 37.8, 37.6 and 43.8 GJ t^{-1} of energy is lost in the AEL, GDE and SOEL respectively. The electrolyzer alone was found to be responsible for 47.3-54.8% of process energy losses. Given this, the improvement of electrolyzer performance is the most important goal for reducing the energy consumption in e-NRR processes.

Table 4.1: Process energy efficiencies (EE_{LHV}) of the different processes, based on the NH_3 lower heating value (LHV) of 18.65 GJ t^{-1} and the 2055 t d^{-1} scale.

	AEL process	GDE PSA process	GDE purge process	SOEL process
EE_{LHV} (%)	27.0	26.7	25.7	20.1

1.1.3 Pre- and Post-treatment

Next to the losses in the electrolyzer, the pre- and post-treatment unit operations still significantly contribute to the process energy consumption, especially for the SOEL process. For the AEL and GDE processes, 9.5-16.1 GJ t^{-1} is consumed in the pre- and post-treatment unit operations, whereas the SOEL process consumes 30.2 GJ t^{-1}. The latter result is considerable, as the SOEL's pre- and post-treatment steps already require a higher energy input than the total SMR-HB benchmark.

A significant contribution to the SOEL process energy consumption is the extensive pre-heating requirement, since the reactant feed needs to be 550 °C. The elevated operation temperatures could aid in N_2 activation and improve the kinetics of e-NRR. It does however not thermodynamically lower the SOEL's equilibrium cell potential (Appendix A.3, Figure A.2). The electricity consumption of e-NRR is not reduced, while the process requires higher pre-heating energy, so the energy consumption of the SOEL process is higher than the AEL and GDE process. In addition, NH_3 decomposition becomes problematic at elevated temperatures above 400 °C, and decreases the current efficiency of the SOEL electrolyzer by up to 20% [54].

Despite these downsides, it could be interesting to analyse a scenario in which waste-heat from other industrial processes can be utilised for pre-heating the reactants. Hereby, the pre-heating energy consumption will be reduced while improving the reaction kinetics. This scenario has been evaluated in previous studies, where it is mentioned that high temperature electrochemical NH_3 synthesis has increased viability when it is coupled with the waste-heat streams from concentrated solar power, nuclear power plants or geothermal heat [104].

Furthermore, it might prove worthwhile to investigate the application of more extensive process heat integration for the SOEL process. Considering that the electrolyzer works at potentials higher than the thermoneutral potential, it is expected that heat will be generated within the electrochemical cell. The streams that

exit the electrolyzer therefore likely possess thermal energy that could be used in a heat exchanger to pre-heat the inlet streams.

1.1.4 Electrolyzer Operating Pressure

The electrolyzer operating pressure has the potential to decrease the energy consumption of the post-treatment condensation step for the SOEL process, since NH_3 condensation is more efficient at elevated pressures. Under the base case assumptions, the condensation step consumes significant amounts of energy (5.22 GJ t^{-1}), caused by the atmospheric operation of the SOEL combined with the high required recovery due to the inapplicability of a product recycle loop (as a result of NH_3 decomposition). If the electrolyzer is operated at 34 bar, the equilibrium condensation temperature is considerably higher (-92 °C at 1 bar versus -52 °C at 34 bar). This has the potential to reduce the condensation energy to 2.9 GJ t^{-1}, 44.4% less than the operating the electrolyzer at 1 bar. Nevertheless, pressurisation of the inlet gasses is required, which increases pre-treatment energy consumption.

Due to the low N_2 solubility, it was established that the AEL required large excesses of electrolyte and produced low NH_3 concentrations in the product stream, which made it necessary to include a product recycle loop in the process (as can be seen in the PFD, Figure 3.8a). For this process, pressurised operation could also be beneficial, since pressure increases the N_2 solubility in the electrolyte. In that case less electrolyte will be needed and the outlet concentration of the formed NH_3 will increase. To add, the higher N_2 solubility could increase the reactant concentration near the cathode, which is expected to reduce the mass-transfer (concentration) overpotential. In water electrolysis, pressurised AEL operation has long been a subject of interest, and there are commercial examples of H_2O-AEL's working at 33 bar (e.g. Sunfire Hydrogen [105]). Nevertheless, while the N_2 solubility is increased from 0.864 mmol% at 1 bar to 25.0 mmol% at 34 bar, the NH_3 product concentration remains below 1.5 mol% (at 34 bar) without the implementation of an accumulation loop. The post-treatment step of removing NH_3 from the product stream (via distillation) was found to be technically infeasible at concentrations below 2 mol% NH_3, hence the accumulation loop remains necessary.

1.2 Economic Evaluation

The economics for the simulated processes were evaluated based on the capital intensity, OPEX and resulting LCOA.

1.2.1 Capital Intensity

The capital intensity of the processes differed among the electrolyzer types and production scales. For all electrolyzer configurations at small (91 t d^{-1}), medium (544 t d^{-1}) and large (2055 t d^{-1}) scales, the capital intensity is presented in Figure 4.2. It can be observed that the AEL process has a capital intensity of 534-580 $ t^{-1}, lower than the GDE PSA scenario (807-832 $ t^{-1}) and the GDE purge scenario (802-849 $ t^{-1}). The SOEL process has a significantly higher capital intensity, at 1,289-1,340 $ t^{-1}.

The capital cost of the electrified processes exhibited economies of scale, but to a lesser extent than SMR-HB, which makes e-NRR more applicable for smaller scale NH_3 production. In Figure 4.2, it can be seen that the CAPEX per tonne NH_3 for the e-NRR processes decreases slightly with increasing scale (an 8% decrease from 91 to 2055 t d^{-1}). This is caused by the assumed scaling factors (M) of the heat exchangers, compressors, air separation units and post-treatment operations, which constitute 3-11% of the capital intensity of the processes. Nevertheless, the SMR-HB capital intensity decreases 64.7% from 91 to 2055 t d^{-1}. The difference between SMR-HB and e-NRR is caused by the linear scaling assumption of the electrolyzers.

The base case results further show that the proposed processes are considerably more capital intensive than the SMR-HB counterpart, which is primarily incurred by the large electrolyzer cost. Figures B.5-B.8 (Appendix B) show the contributions of the individual unit operations on the total CAPEX. The electrolyzer cost ($ m^{-2}) exhibited the largest CAPEX contribution (89-97%) for all processes. Hence, the base case electrolyzer cost assumption has the most considerable impact on overall process capital intensity. Nonetheless, the assumptions used to estimate the electrolyzer cost are not without ambiguity, as will be highlighted in the next paragraphs.

Herein, the cost of the electrolyzers were based on the cost of industrial H_2O-electrolyzers. This assumption is difficult to validate due to the infancy of e-NRR electrolyzer technology. It is not logical to extrapolate the cost data from e-NRR laboratory experiments, hence the only probable commercial benchmark was assumed to come from H_2O electrolyzer technology. Nonetheless, it is hard to forecast to what extent e-NRR electrolyzers will actually resemble the ones used for water splitting. The electrolyzer costs of the presented processes are therefore questionable.

Figure 4.2: Capital intensity ($ t^{-1}) of different electrolyzer configurations. SMR-HB capital intensity data is based on the forthcoming publication by Izelaar et al. [31].

In previous techno-economic e-NRR literature (i.e. [23, 7]), lower electrolyzer prices were assumed, which were actually not based on industrial H_2O electrolyzer prices. As has been mentioned in the *Method* chapter in Table 3.7, Wang et al. and Fernandez et al. expected a 3.5-8 times smaller electrolyzer cost. Nevertheless, these papers did not validate their electrolyzer cost assumptions with literature, so their overall findings remain questionable.

1.2.2 Operational Expenditure

The operational expenses (OPEX) for all unit operations of the conceptual processes are displayed in Figure 4.3. The OPEX did not show significant variations at different scales, since these varied only in the type of ASU used, which had a minor contribution to the total OPEX (1.1-3.1%). Hence, only the normalised OPEX ($ per tonne NH_3) for the 2055 t d^{-1} scale is presented in the figure.

The OPEX values of the AEL, GDE and SOEL processes differed significantly. It can be seen that the AEL process has the smallest OPEX at 1,857 $ t^{-1}, followed by GDE PSA (1,932 $ t^{-1}) and GDE purge processes (1,998 $ t^{-1}). The OPEX of the SOEL process is at 2,723 $ t^{-1} considerably higher, which was caused by the larger pre-heating and electrolyzer energy consumption (Section 1.1).

The OPEX of the SMR-HB benchmark was a lot lower at 344-396 $ t^{-1}, under the assumption of a natural gas price of 6.97 $ MMBTU^{-1}. The difference between e-NRR and SMR-HB can be explained by looking at the different OPEX contributions. The operational expenses of the e-NRR processes were categorised as (1) electricity, (2) steam, (3) cooling water, (4) raw materials and (5) miscellaneous (payroll, O&M, cost for consumables). The first three of these are directly determined by the process energy consumption, and it was found that electricity had the largest contribution to the OPEX (>80%) (Appendix B, Figure B.4). It was also observed (Section 1.1) that all e-NRR processes are significantly more energy intensive than the SMR-HB process, which offers an explanation for the higher e-NRR operating cost. It is expected that decreasing the process energy consumption, by for instance improving the e-NRR electrolyzer performances (increasing FE and reducing overpotential), can significantly decrease the OPEX.

Due to the high contribution of electricity costs to the OPEX, decreased electricity market prices can considerably lower the operational expenses for the e-NRR processes. Under the base-case assumption, it was assumed that the electricity price is equal to the U.S. 2022 industry average of 0.0863 $ kWh^{-1}. Nonetheless, it is stated in the literature that the cost of renewable electricity is expected to substantially decline to much lower values, owing to the increased investment in electricity generation from renewable energy sources (RES) like wind and solar power [106]. Optimistic predictions state that the price of renewable electricity will decline to 0.02 $ kWh^{-1} in the near future [106], which has been calculated to decrease the e-NRR OPEX by 50%.

Operation and maintenance (O&M) costs are shown in Figure 4.3 and have with 10.9-17.7% the second
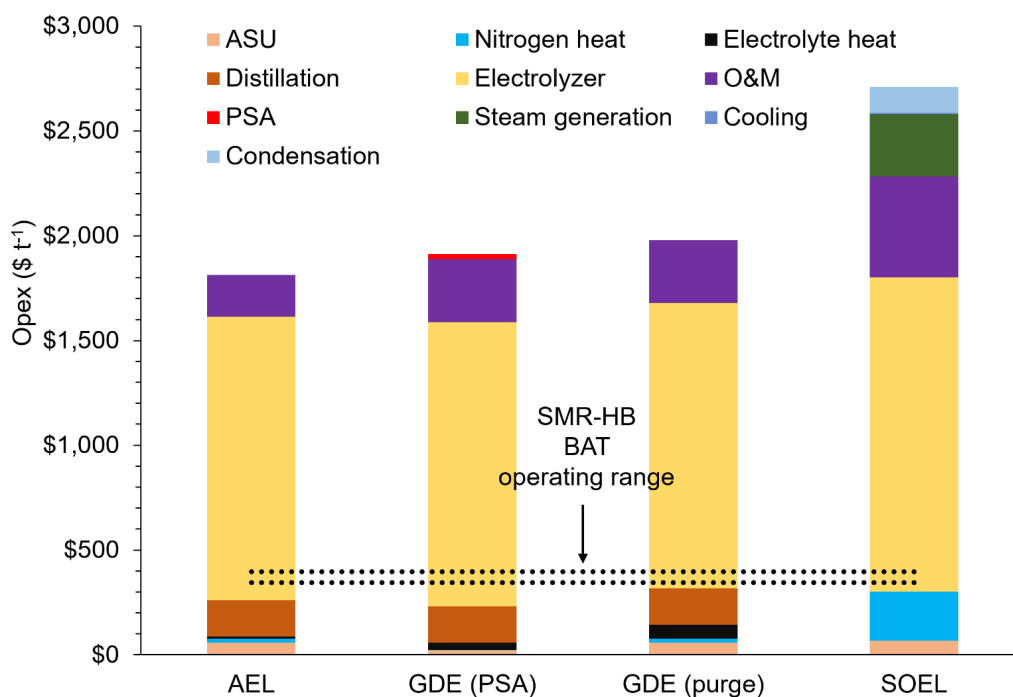
Figure 4.3: Normalised operational expenditure ($ t^{-1}) of different electrolyzer configurations for the 2055 t d^{-1} scale. The SMR-HB BAT OPEX is based on the forthcoming publication by Izelaar et al. [31] and assumes the natural gas price in 2019 (6.97 $ MMBTU^{-1}).

largest contribution to the OPEX. O&M costs were assumed 3% of the CAPEX, and therefore increased with a higher capital intensity. The e-NRR processes were significantly more capital intense than the SMR-HB process, caused by the high cost of the electrolyzer (Section 5.4). Since the SOEL process was the most capital intense, it was found to have the largest O&M cost too, at 481 $ t^{-1}, higher than the total SMR-HB's OPEX.

It is projected that electrochemical processes, particularly those involving solid oxide electrolytes, will encounter durability and degradation issues over time, resulting in relatively large O&M costs [35]. In this research, it was assumed that these costs were fixed and did not change over the lifetime of the facility. Nonetheless, it can be expected that the electrolyzer degradation will increase over time.

1.2.3 LCOA

Figure 4.4 presents the NH$_3$ production costs (LCOA) for the different scales and electrolyzer types, and concludes that the AEL process at 2055 t d^{-1} has the lowest LCOA at 2,311 $ t^{-1}. The GDE PSA and GDE purge processes, including and excluding H$_2$ isolation, costed 2,607 $ t^{-1} and 2,818 $ t^{-1}, respectively. The inclusion of H$_2$/N$_2$ separating infrastructure appears an attractive addition. The SOEL process is the most expensive to operate and requires the highest capital investment, hence has the the largest LCOA of 4,128 $ t^{-1} at 2055 t d^{-1}.

It was found that there is still a large gap in LCOA for the electrochemical processes compared to SMR-HB benchmark, which resulted in a limited expected viability of the presented e-NRR processes under the base-case assumptions. The LCOA of SMR-HB at different scales is equal to 339, 492 and 602 $ t^{-1} at 2055, 544 and 91 t d^{-1}, respectively. These values are at least a factor 6 smaller than the most cost-effective e-NRR process (the 2055 t d^{-1} AEL). The difference between e-NRR and SMR-HB becomes slightly smaller when a CO$_2$ tax of 51 $ t^{-1}$_{CO_2}$ was added to the SMR-HB LCOA, as is shown in Table 4.2. Despite that, the difference between e-NRR and SMR-HB remained substantial and one can therefore argue that e-NRR NH$_3$ has lower economic feasibility when compared to the SMR-HB benchmark.

e-NRR operation at smaller scale shows a slightly lower absolute difference with SMR-HB. In the previous subsection (Subsection 1.2.1), it was mentioned that the capital intensity of the e-NRR processes decreased less at larger scale than the SMR-HB benchmark. This can equally be observed in the data for the LCOA. For the AEL, GDE and SOEL processes, the LCOA of 2055 t d^{-1} versus 91 t d^{-1} scales sees an increase of 3.7-7.9%, whereas the SMR-HB benchmark increases by 43%. Although operating at smaller scales appears to result in smaller deviations from the SMR-HB benchmark, the difference is minimal and the base-case e-NRR processes remain economically unattractive.

Previous e-NRR techno-economic studies generally forecast a lower LCOA [7, 23], which is primarily
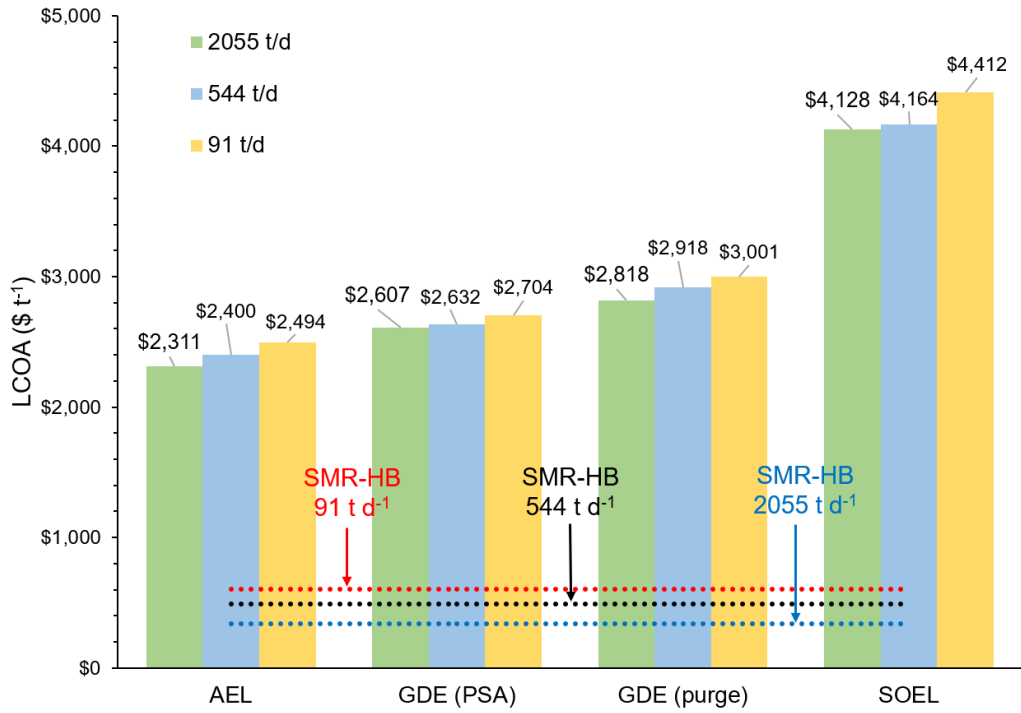
Figure 4.4: LCOA ($ t^{-1}) of different electrolyzers and scales. The SMR-HB data is based on the forthcoming publication by Izelaar et al. [31].

Table 4.2: LCOA of SMR-HB (a) excluding CO_2 tax and (b) including CO_2 tax (51 $ per tonne CO_2) for scales from 91 t d^{-1} to 2055 t d^{-1}. The data is obtained on the forthcoming publication by Izelaar et al. [31].

Scale (t d^{-1})	Excluding CO_2 tax ($ t^{-1})	Including CO_2 tax ($ t^{-1})
2055	$ 339	$ 426
544	$ 492	$ 579
91	$ 602	$ 689

caused by their model assumptions. These are summarised in Table 4.3 and compared with the main assumptions from this work. Wang et al. [7] assumes more optimistic electrolyzer performance parameters (FE, J, η), as well as a lower electricity price (0.02 $ kWh^{-1}) and electrolyzer cost (1,000-3,000 $ m^{-2}). Fernandez et al. [23] assumes less optimistic electrolyzer parameters, but uses much lower electrolyzer costs (200-300 $ m^{-2}). This has logically resulted in significantly lower LCOAs (339-400 $ t^{-1} [7] and 930 $ t^{-1} [23]). It can be assumed that the LCOA calculated in this work will be more economically appealing if the base-case assumptions would have been chosen more optimistically.

Table 4.3: Assumptions and LCOA results of preceding economic analyses about electrochemical NH_3 synthesis. Data obtained from ref. [7] and [23].

	Wang et al. [7]	Fernandez et al. [23]	This research
Scale (t d^{-1})	100	0.03	2055, 544 and 91
Electrolyzer type	SOEL and GDE	MEA	AEL, GDE and SOEL
J (A cm^{-2})	0.5	0.1	0.3
η (V)	0.37-0.6	n.a.	0.9-1.1
FE (%)	90	30	70
Elec. price ($ kWh^{-1})	$ 0.02	$ 0.03	$ 0.0863
Electrolyzer cost ($ m^{-2})	$ 1,000 - $ 3,000	$ 200 - $ 300	$ 7,800 - $ 15,937
LCOA ($ t^{-1})	$ 339 - $ 400	$ 930	$ 2,311 - $ 4,412

1.3 Process Implementation Issues

While the previous sections mentioned considerations about the process energy consumption, CAPEX, OPEX and LCOA, several important process implementation issues are overlooked and will be discussed in the following subsections.

1.3.1 Alkaline Electrolyzer

Resulting from the low N_2 solubility the AEL's electrolyte, high excesses of electrolyte were required, which are expected to limit the practicality of the AEL process. To dissolve the required N_2 for the synthesis of one tonne of NH_3, 80,970 tonnes of electrolyte was required (*Mass Balances*, Appendix C, Table C.3). This caused a large volume inflow ($\sim 1.4 \cdot 10^6$ L s^{-1}) into the electrolyzer, and it is unclear whether the electrolyzer system can be designed to handle volume flow rates of this magnitude.

Another issue is the limited N_2 mass transfer from the bulk solution towards the cathode, thereby effectively limiting the NH_3 production rate. In the model, it has been assumed that the bulk concentration was equal to the concentration of N_2 at the electrode, thus neglecting mass-transfer limitations. In reality, there will be a concentration gradient between the bulk and electrode (*Literature review*, Section 2.1). Upon operation of the electrochemical cell, the electrode concentration needs to be replenished from the bulk, which is constrained if the N_2 concentration in the bulk phase is low. In literature, it is mentioned that the limiting current densities for AEL are constrained to $0.6 \cdot 10^{-4}$ A cm^{-2} [59], which is more than 10,000 times less than the assumed J of 0.3 A cm^{-2}.

Additional constraints can arise from recycling the electrolyte for the purpose of NH_3 accumulation. In the model, the assumption was made that the recycled NH_3 does not decompose in the electrolyzer. Nonetheless, there is a possibility that NH_3 can reach the anolyte as a result of membrane-cross over. When NH_3 reaches the anode, there is a possibility of it being oxidised, which would reduce the amount of recoverable product.

It can also be expected that the accumulation loop will result in issues with switching on and off, since the system will require long start-up times to reach steady state (~ 1.96 hours). This can inhibit the practicality of the AEL process in two scenarios:

1. *Maintenance downtime*: Maintenance requires the electrolyzer to be switched off , thereby stopping the electrolyte recycle system. This requires a long time to reach steady state when switched back on, and causes large energy and product losses.

2. *Intermittent energy supply*: Owing to the long start-up times, the accumulation loop is less suitable for intermittent operation. Ideally, future NH_3 production should be powered by renewable electricity. Renewable energy systems like solar and wind are not continuously available and have variable generation levels resulting from fluctuations in weather conditions. It would therefore be difficult to couple the AEL to renewable energy sources, and additional energy storage infrastructure would be needed.

1.3.2 Solid Oxide Electrolyzer

The SOEL is expected to be less compatible with intermittent operation, caused by the high temperature requirements. Material degradation is increased when SOEL's are operated intermittently [35], as heating and cooling increases the thermal stress and fatigues the electrolyte. This reduces the system lifespan and results in higher maintenance costs, which will increase the LCOA.

Additionally, high temperature operation reduces the switching capability, due to the time it takes to reach the required optimal operating temperature. This additional time can result in energy wastage, since the electrolyzer will operate on sub-optimal temperatures during heating to the optimal temperatures. The cold start up time of solid oxide H_2O electrolyzer is in the order of hours, which is higher than that of proton exchange membrane electrolyzers which takes minutes [35].

We have seen that in order for the AEL and SOEL to work intermittently, energy storage infrastructure must be included within the process design, which will significantly increase the LCOA. It has been estimated from literature that the application of lithium-ion batteries as the energy storage medium will add 1,800 $ per tonne NH_3 of capital intensity [7], thereby almost certainly diminishing overall the process viability. Another option for intermittent operation could be the application of the H_2 by-product in combination with a fuel cell.

2 Sensitivity Analysis

The sensitivity analysis evaluates how the alteration of model parameters from the base-case assumption to more optimistic (and pessimistic) values influenced the economic performance of the e-NRR processes. The altered model parameters (named uncertainty variables) are the electricity price, electrolyzer cost, faradaic efficiency, cathodic overpotential and current density, and were selected based on their impact on the LCOA. This section aims to analyse what variables have the biggest contribution to the e-NRR's economic performance, and to uncover what value they require to result in an economically viable process.

2.1 Sensitivity Analysis on the LCOA

Figure 4.5 shows that among the chosen uncertainty variables, the electricity price has the largest effect on the LCOA for all electrolyzer types. When the electricity price is changed to 0.02 \$ kWh^{-1} for the optimistic case, the LCOA is decreased by 41.4-52.7% depending on the electrolyzer. The electricity price can thus increase the economic viability of e-NRR NH$_3$ production to the largest extent when compared to the other uncertainty variables.

In addition to the electricity price, the electrolyzer cost also had the potential to significantly reduce the NH$_3$ production cost, especially for the SOEL and GDE processes. When the electrolyzer cost of the AEL process was reduced to 2,000 \$ m^{-2}, the LCOA decreased by 27.3%. For the GDE processes, the LCOA decreased with 34.2% and 37.0% for the PSA and purge scenario respectively, assuming an electrolyzer cost of 3,000 \$ m^{-2}. The LCOA decreased 39.4% for the SOEL process assuming an electrolyzer cost of 3,500 \$ m^{-2}. The GDE and SOEL processes have significantly higher base-case electrolyzer costs than the AEL, so this explains the relatively large effect on the LCOA.
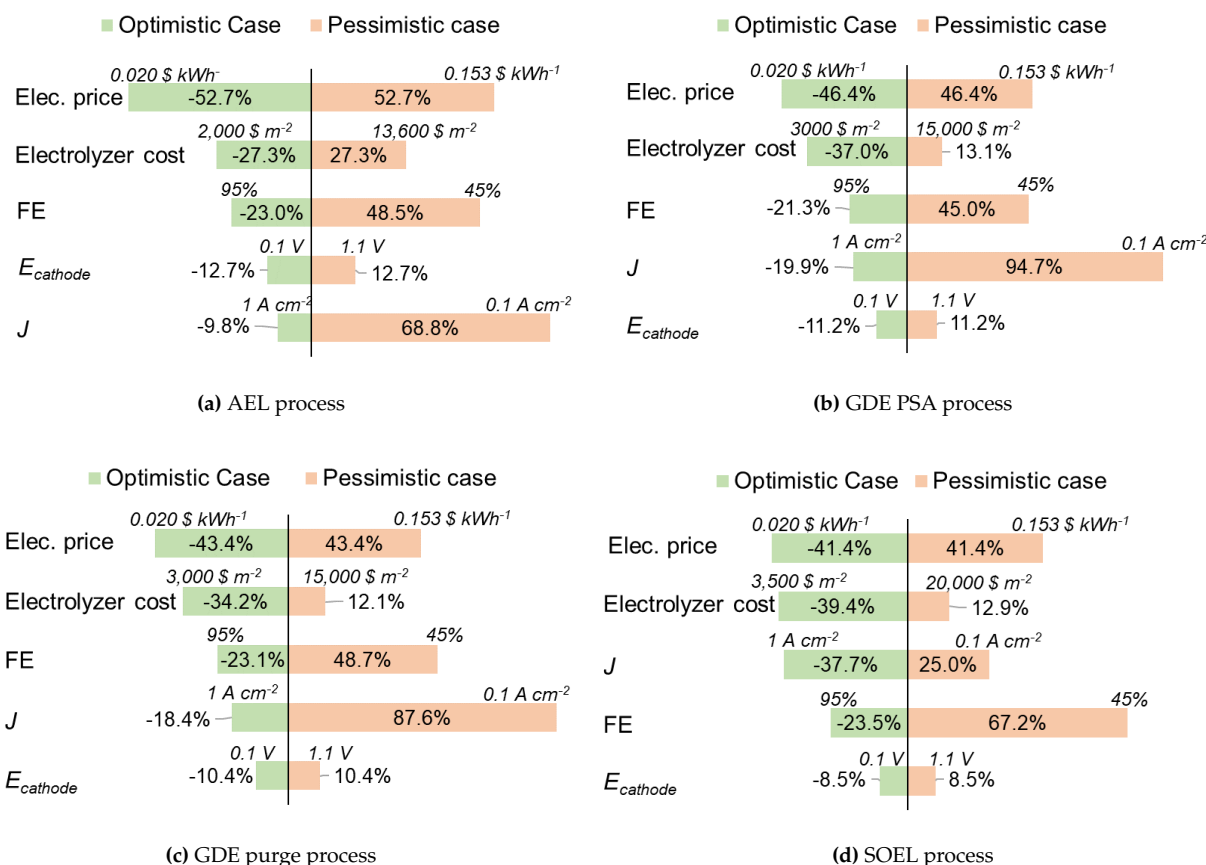
Figure 4.5: Percent deviation of LCOA for optimistic (green) and pessimistic (orange) parameter assumptions compared to the base case. Shown for the (a) AEL process, (b) GDE PSA process, (c) GDE purge process and (d) SOEL process.

Increasing the faradaic efficiency from the base case (70%) to an optimistic 95%, the LCOA decreased by 19.9-23.5%. On the other hand, under the pessimistic assumption of 45% FE, the LCOA increases by 45-67%. This indicates that the negative effect of a lower FE assumption is larger than the positive effect of a higher FE.

The current density follows a similar pattern, showing a reduction in the LCOA for the optimistic case of 9.8-37.7%, whereas the pessimistic case shows an increase of 48.5%-94.7%. The alteration of the current

density equally showed large differences among the different electrolyzer types. It was observed that the SOEL was more sensitive to the current density than the other processes (Figure 4.5d), which is caused by its larger electrolyzer cost per m^2. The current density directly determined the necessary electrode area, so larger electrolyzer costs (per m^2) have an increased influence on the LCOA.

2.2 Sensitivity Patterns

While the previous section highlighted the effects of the uncertainty variables on the LCOA, they did not explain the root causes of the observations. Therefore, the next sections will focus on elaborating on the observed patterns and aim to validate the observations made in the previous section.

2.2.1 Electricity Price

In Figure 4.6, the LCOA is plotted against varying electricity prices for the AEL (4.6a) and SOEL (4.6b) processes, highlighting a linear dependency between the electricity price and LCOA. The GDE processes showed similar results to the AEL and were therefore omitted from this analysis.

It was observed that the AEL (and GDE) processes were more sensitive to the electricity price than the SOEL. This is caused by the relatively large O&M OPEX of the SOEL process, caused by its large electrolyzer cost. The AEL had a lower O&M OPEX contribution, and thus a proportionally higher electricity expenditure than the SOEL, explaining its larger sensitivity.

Figure 4.6 also shows different electrolyzer costs for the AEL and SOEL processes. It was found that reducing the electrolyzer cost made the processes more sensitive to the electricity price. By halving the AEL's cost, the electricity price sensitivity (upon reduction from 0.0863 to 0.02 $ kWh^{-1}) of the AEL process was equal to -64.1% instead of the -52.7% observed at the base case electrolyzer cost. For the SOEL, a 57.7% electricity price sensitivity was observed when the electrolyzer cost was halved, versus the 41.4% sensitivity at base case electrolyzer cost. The electrolyzer costs affected the O&M OPEX of the processes, and reducing these cost therefore increased the relative contribution of the electricity price to the OPEX, making the processes more sensitive to the electricity price.

To reach SMR-HB parity, lower electricity prices show a promising effect on lowering the LCOA, but other process improvements must also be made. The AEL process with an electricity price of 0.02 $ kWh^{-1}, and an electrolyzer cost reduction of approximately 50% (4,000 $ m^{-2}), showed an LCOA of 680 $ t^{-1}. Note, that the LCOA of SMR-HB is still nearly twice as low. For the SOEL process it was found that nearly halving the electrolyzer cost (9,000 $ m^{-2}) and reducing the electricity price to 0.02 $ kWh^{-1} gives an LCOA of 1,513 $ t^{-1}.
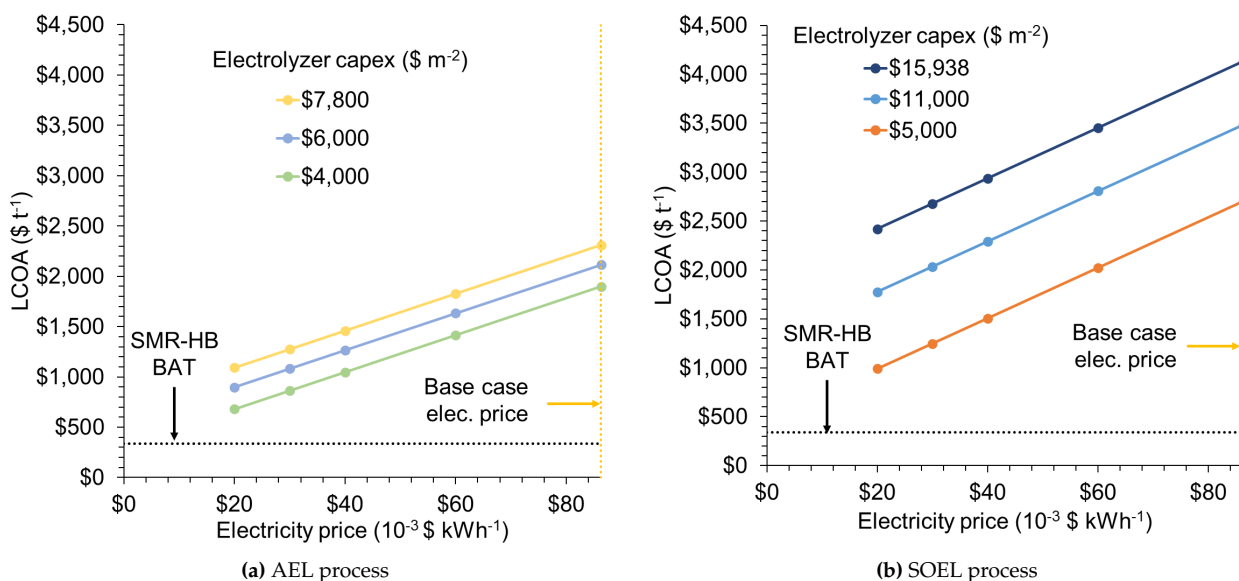
Figure 4.6: Effect of electricity price and electrolyzer cost on LCOA for the (a) AEL process and (b) SOEL process.

2.2.2 Current Density

Figure 4.7 shows the effect of changing the current density on the LCOA, indicating a hyperbolic dependency and an approaching vertical asymptote at low current densities for all electrolyzers. Operating at current

densities lower than the base case makes the processes less appealing, showing LCOAs as high as 14,289 $ t^{-1} for the SOEL process, and between 6,416 $ t^{-1} and 8,914 $ t^{-1} for the AEL and GDE processes at a current density of 0.05 A cm^{-2}. Moreover, when working at current densities higher than the base case, the LCOA is found to decrease slightly. These two observations from the figure support the statements made earlier (Section 2.2), where current densities higher than the base case showed limited gains, whereas lower current densities make the processes substantially worse. It can therefore be argued that operating at a current density of 0.3 A cm^{-2} (obtained from the DoE REFUEL program [13]) appears to be a relevant benchmark performance.

The hyperbolic effect can be explained by looking at how the current density affects the output parameters. The required electrode area, which is used as the scaling unit of the electrolyzer, was calculated by dividing the total current by the current density. It was therefore observed that the capital intensity of the processes followed a $1/x$ rational function behaviour, which can also be recognised in the LCOA curve shown in Figure 4.7. The current density further affected the cell potential (E_{total}), since a higher current will result in a higher Ohmic losses (Appendix B, Figure B.9). For instance, the cell potential of the AEL and GDE reached 5.2 and 5.3 V when operating at 3.5 A cm^{-2}.
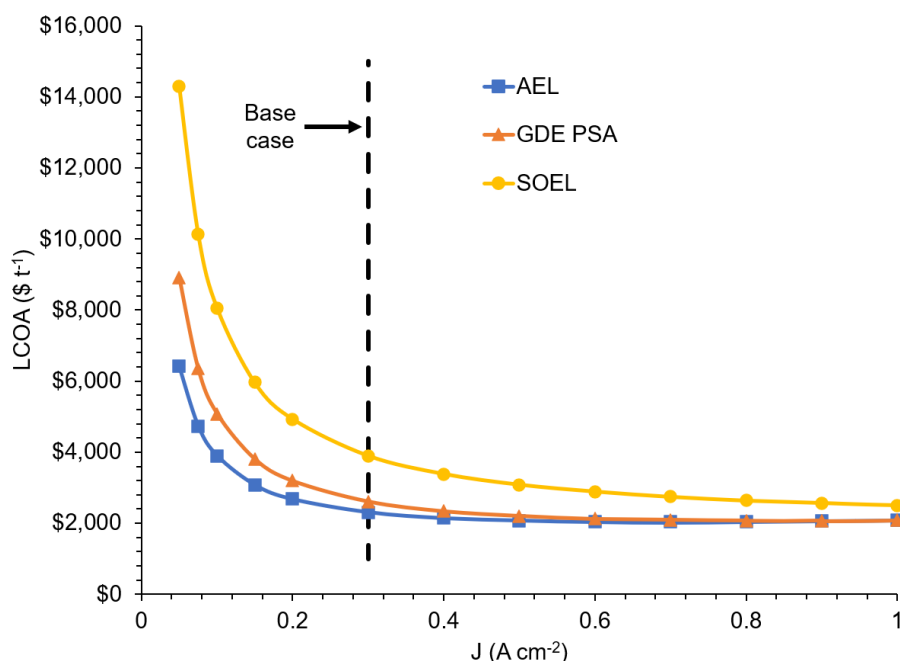
Figure 4.7: Effect of current density (J) on the LCOA for different electrolyzer processes.

2.2.3 Faradaic Efficiency

The FE has an effect on energy consumption of the electrolyzer and the product separation. For instance, the FE influences the required current necessary to reach NH$_3$ production capacity, which is used to calculate the electrolyzer power consumption. Additionally, the FE determines the composition of the electrolyzer product streams, which affects the post-treatment. The latter effect is especially relevant for the SOEL, since NH$_3$ will form in the gas phase. On the contrary, the AEL and GDE have NH$_3$ formation in the liquid phase, and its composition is not directly influenced by the FE. Nonetheless, the GDE process is presented with a H$_2$/N$_2$ separation step, whose energy consumption and viability does seem to be influenced by the FE.

The preceding points all impacted the calculated LCOA values, which consequently showed a high sensitivity towards the FE for the electrolyzer configurations, as can be seen in Figure 4.8. The figure shows that the AEL and GDE PSA processes have a similar dependency on the FE, displaying a more or less constant LCOA for FEs above 60%, but show a large increase below that. The SOEL process was seen to have a slightly higher sensitivity to the FE, which is primarily caused by the FEs effect on the the condensation step.

It was found that with increasing FE, the NH$_3$ concentration in the product stream of the SOEL increased from 4.7 mol% at a FE of 10%, to 15.8 mol% at a FE of 95%, which is presented as the purple line in Figure 4.8b. Condensation was found to be facilitated at higher NH$_3$ concentration (blue line in Figure 4.8b), yielding an energy consumption of 16.2 GJ t^{-1} at 4.7 mol% and 4.9 GJ t^{-1} at 15.8 mol%. The energy consumption of the SOEL's condensation step is thus significantly increased at low FE, which explains the larger observed FE sensitivity of the SOEL process compared to the other processes.

For the GDE PSA process, it was found that lower FE increased the potential revenue by selling H_2 as a value adding product, which increases the attractiveness of adding the H_2/N_2 separation infrastructure to the process. This can be seen in the blue curve of Figure 4.8c, which shows that the H_2 revenue (per tonne NH_3) decreases from 3,312 $ t^{-1} at 10% FE to 19.4 $ t^{-1} at a FE of 95%. This curve additionally shows the effect of the FE on the OPEX, where a higher OPEX is observed caused by the larger electrolyzer energy consumption. Upon a decrease of the FE from 95% to 10%, the OPEX sees an increase of 850% from 999 $ t^{-1} to 9,493 $ t^{-1}. It can be argued that the primary goal of the presented process is to sell NH_3, for which a high FE is absolutely beneficial. Nonetheless, a lower FE appears to make H_2 separation a more appealing unit operation as an addition to the process.

(a) LCOA FE sensitivity

(b) Posttreatment NH_3 condensation FE sensitivity

(c) H_2 sales (with PSA) and electrolyzer OPEX FE sensitivity
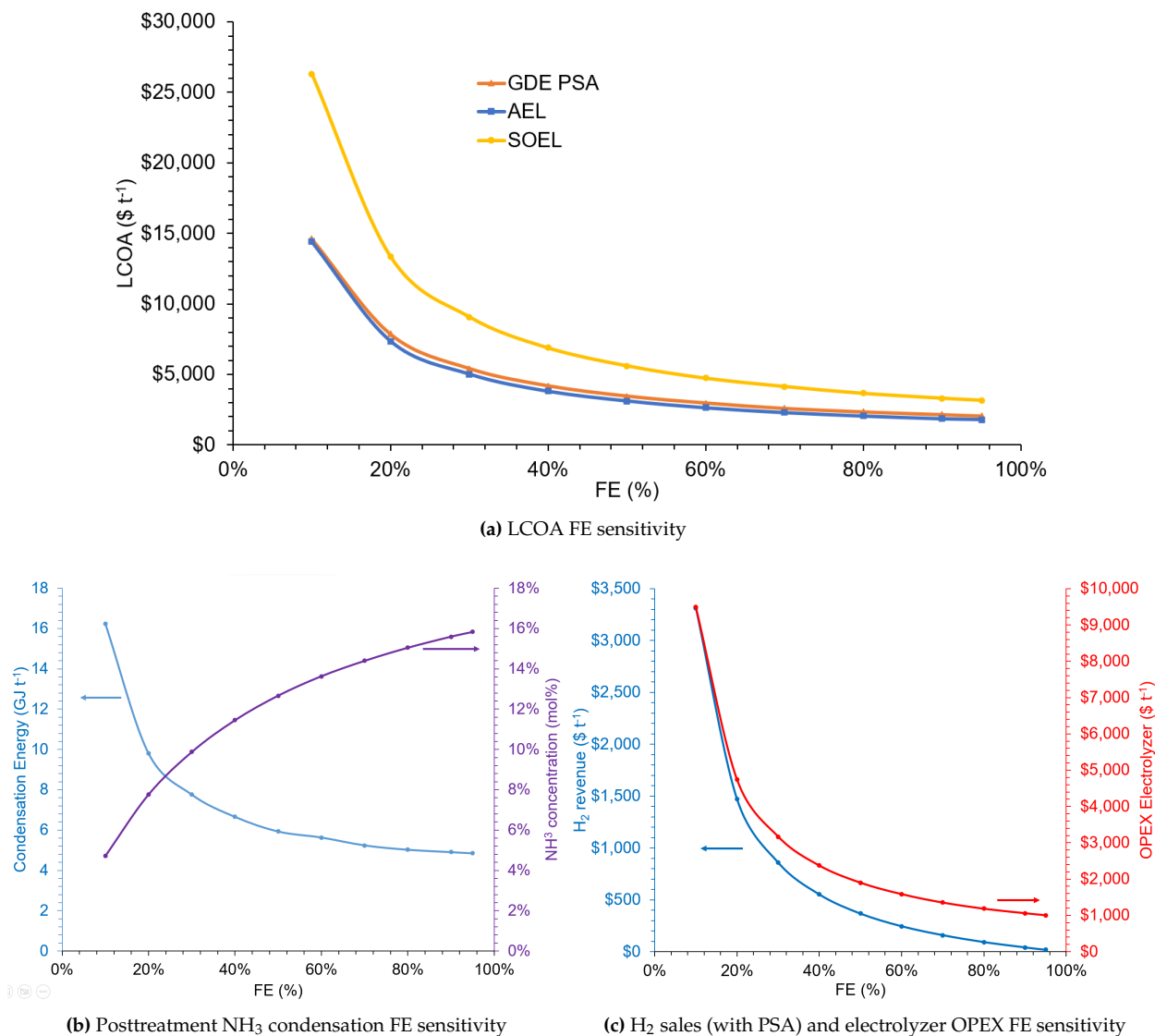
Figure 4.8: Results of varying the faradaic efficiency (FE) on (a) LCOA, and (b-c) post-treatment operational expenditure.

3   Optimised Case

This section will elaborate on the optimised parameter assumptions of the five most important model variables (electricity price, current density, electrolyzer cost, faradaic efficiency and cathodic overpotential). This scenario is ultimately used to understand under which conditions e-NRR will reach SMR-HB parity. The optimised assumptions will be judged based on their technical and commercial validity.

3.1   Choice of Optimised Parameters

The optimistic parameter assumptions for the optimised case were chosen as follows:

- *Electricity price*: With the LCOA being most sensitive to the electricity price for all electrolyzer types and scales (Subsection 2.1), a low electricity price was found the most important parameter for the economic appeal of e-NRR NH_3 synthesis. The electricity price is likely to decline to under 0.020 $ kWh^{-1} in the near future [106]. This is used as the assumption for the optimistic scenario.

- *Current density*: The current density is determined by several technical limitations that are specific for each electrolyzer type. Increasing the current density above 0.3 A cm^{-1} did not yield relevant LCOA improvement. Nonetheless, as a result of technological advances, it is expected that electrochemical systems will be able to work at higher current densities in the future [97]. In literature, it is claimed that alkaline H_2O electrolyzers are technically limited to 0.5 A cm^{-2} [35], which will form the assumption for the optimistic case AEL.

  For the SOEL, it is expected that the current density is limited to 1.0 A cm^{-2} [97]. The GDE current density is not extensively treated in literature, but it can be expected that this type of cell layout can equally be operated at 1.0 A cm^{-2} due to the low electrolyte flow channel thickness.

- *Electrolyzer cost*: Due to the lack of existing commercialised e-NRR electrolyzer systems, the optimistic cost limits of the e-NRR cells proved difficult to accurately forecast. However, cost forecasts do exist for H_2O electrolyzer systems [97], which were thus used to formulate the optimised-case electrolyzer cost assumptions. The AEL cost has been forecast to decrease towards 2,700 $ m^{-2}, whereas the SOEL is assumed to decline to 3,240 $ m^{-2} [97]. Additionally, GDE cost could fall to 2,970 $ m^{-2}.

- *Faradaic efficiency*: The base-case FE assumption of 70% already falls into an optimistic domain. However, the DoE REFUEL program [13] stipulates a FE of 95%, which is taken as the optimistic case assumption.

- *Cathodic overpotential*: The LCOA showed limited sensitivity to the value of cathodic overpotential. Due to the immanent difficulty in N_2-activation, the activation overpotential will likely not fall short of the base-case value of 0.6 V. However, in an optimistic scenario, it could fall below 0.4 V [45].

These observations were distilled into two optimised-case scenarios: an optimistic scenario where the most positive limits for all parameters are chosen; and a more realistic scenario that keeps all base-case parameters equal, except for the electricity price. The parameter values of the optimistic and realistic scenario have been summarised in Table 4.4.

Table 4.4: Optimised parameter assumptions for the optimistic and realistic scenarios.

Parameter	AEL		GDE		SOEL	
	Optimistic	Realistic	Optimistic	Realistic	Optimistic	Realistic
Elec. price ($ kWh $^{-1}$)	$ 0.02	$ 0.02	$ 0.02	$ 0.02	$ 0.02	$ 0.02
J (A cm^{-2})	0.5	0.3	1.0	0.3	1.0	0.3
FE (%)	95	70	95	70	95	70
$E_{cathode}$ (V)	0.4	0.6	0.4	0.6	0.4	0.6
Electrolyzer cost ($ m^{-2})	$ 2,700	$ 7,800	$ 2,970	$ 11,868	$ 3,240	$ 15,937

3.2   Optimised Results

Figure 4.9 shows the results of the LCOA for the optimistic and realistic scenarios, for the processes with varying scale and electrolyzer types.
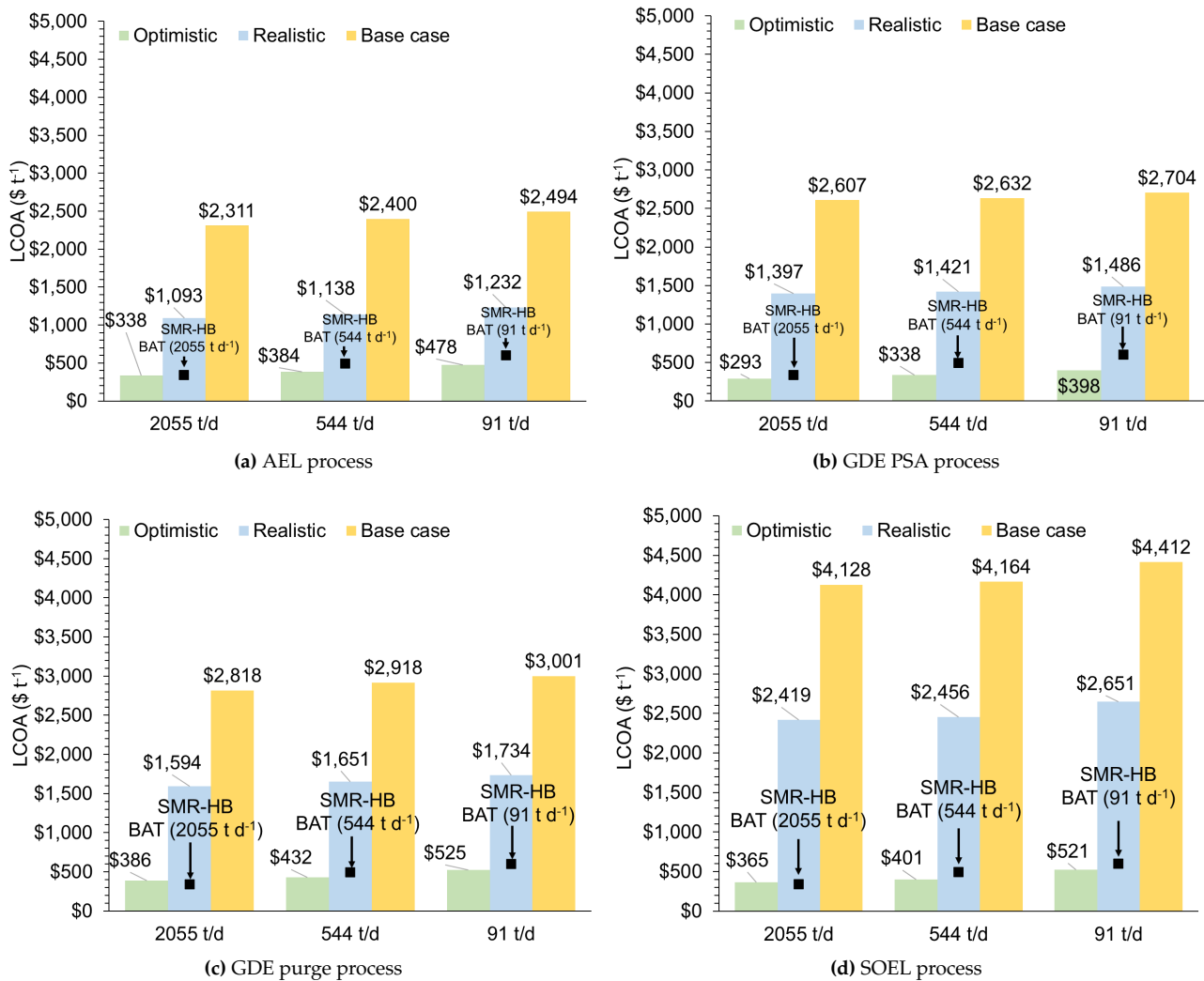
Figure 4.9: Results of optimistic scenario (green) and realistic scenario (blue) for the (a) AEL process, (b) GDE PSA process, (c) GDE purge process and (d) SOEL process.

In Figure 4.9, it can be observed that the GDE PSA has an optimised LCOA of 293-398 $ t^{-1}, lower than the AEL (338-477 $ t^{-1}) and the SOEL (365-521 $ t^{-1}). For the GDE purge, an optimised LCOA of 386-525 $ t^{-1} was found. It can thus be concluded that under the optimised case assumptions, the GDE process with H_2/N_2 separating infrastructure is economically the most compelling. This is primarily caused by its ability to work at a higher current density than the AEL, which reduces the electrode area of the electrolyzer, so it has a lower capital intensity. Next to that, the GDE assumes a slightly lower electrolyzer cost than the SOEL and requires far less pre-heating energy, which explains the SOEL process's higher LCOA in the optimised case compared to the GDE PSA process.

It appears that the addition of the PSA unit for H_2/N_2 separation makes the GDE processes more compelling than the purge scenario, owing to the ability of adding a N_2 recycle loop to the process. This recycle reduces the ASU duty, which was observed to individually reduce the LCOA of the GDE process from 386 $ t^{-1} to 293 $ t^{-1} (-24.1%) in the 2055 t d^{-1} process. To add, the optimised case assumes a FE of 95%, which resulted in a maximum possible H_2 revenue of 19.4 $ t^{-1}. It could therefore be argued that the application of H_2/N_2 separation is more useful for the development of the N_2 recycle loop, rather than for selling H_2 as a value-adding by-product.

Figure 4.9d shows that the SOEL process sees the largest reduction from the realistic case (2,419-2,651 $ t^{-1}) to the optimised case (365-521 $ t^{-1}), which can be explained by the assumptions for the electrolyzer cost, current density and FE. When comparing the realistic and optimistic cases, the electrolyzer cost is reduced from 15,937 $ t^{-1} to 3,240 $ t^{-1} (80% reduction). Combining this with the current density increase from 0.3 A cm^{-2} to 1.0 A cm^{-2}, the SOEL requires significantly lower electrode area and the SOEL's capital intensity is thus reduced substantially. Moreover, the higher FE in the optimistic case was found to reduce the energy consumption of the post-treatment condensation step, thereby reducing OPEX too.

Figure 4.9 equally highlights that small-scale e-NRR operation is more economical when compared to the

benchmark. For the GDE PSA process, the optimistic LCOA at 91 t d^{-1} scale was found to be 33% lower when compared to the 91 t d^{-1} SMR-HB benchmark of 602 $ t^{-1}. On the other hand, the difference between the optimistic GDE PSA process and SMR-HB was equal to 13% at 2055 t d^{-1}. All in all, it appears that the GDE PSA process at 91 t d^{-1} has the most appeal compared to the other electrolyzer configurations in the optimised case. It is further observed that all other electrolyzer configurations fall below the SMR-HB benchmark in the optimistic scenario and at the 91 t d^{-1} scale. Nonetheless, the practicality of the AEL and SOEL processes is lower compared to the GDE process.

3.2.1 Validation of Optimised Parameters

The optimistic case shows that e-NRR can potentially have a lower LCOA than SMR-HB. Nonetheless, the optimistic case parameter assumptions are questionable because of the following reasons:

- *Electricity price*: Although average electricity prices will likely decline in the future, the electricity price remains a market variable, and will display significant degrees of volatility owing to numerous and complicated effects, which make the electricity market price a difficult parameter for accurate forecasting. Moreover, the electricity needs to be supplied from renewable energy sources to properly offset CO_2 emissions, which are often accompanied by an intermittent demand pattern resulting in large fluctuations in their levelized cost of electricity (LCOE) [107].

- *Current density*: For the AEL electrolyzer, assuming that *J* equals 0.5 A cm^{-2} is not realistic, owing to the low N_2 solubility and resulting mass-transfer limited current density that was mentioned in *Process implementation issues* (Section 1.3). For the GDE and SOEL electrolyzers, it was found that they do not suffer from mass-transfer related issues, which makes their optimistic case assumption of 1 A cm^{-2} less ambiguous.

- *Electrolyzer cost*: The forecasts of the electrolyzer prices come from water electrolyzers. It is uncertain whether these can be directly copied for e-NRR electrolyzers.

- *Faradaic efficiency*: Looking at the most up-to-date performance for e-NRR systems (Chapter 2, Section 2.1), the FE appears to be far removed from the DoE objective (the highest recorded FE was found equal to 66% [76]). In essence, the FE of 95% can be taken as an upper limit, but it is doubtful whether this could ever be reached.

- *Cathodic overpotential*: The assumed activation overpotentials have been obtained from DFT papers. The activation potential is yet to validated experimentally.

Taking these considerations in mind, the optimised case parameters could not be validated and the actual probability of e-NRR replacing HB remains questionable.

Chapter 5

Conclusion

The goal of this thesis was to investigate if and under what techno-economic conditions the e-NRR could potentially become compelling over the SMR HB benchmark. This was done by developing a model for different types of electrolyzers and different scales. Taking the LCOA as a metric for gauging overall performance, it was found that the viability of e-NRR NH_3 synthesis depends on several technical and non-technical parameters, which could theoretically yield a production costs below that of SMR-HB. The following bullet-points aim to elaborate on the most important aspects from this analysis.

- **Scale**: The simulation results showed that larger scales yielded a lower LCOA. Nonetheless, the economies of scale were less apparent when compared to SMR-HB, as the electrolyzer scaled linear and had the largest contribution to e-NRR process CAPEX. On the other hand, nearly all process equipment in the SMR-HB process showed non-linear scaling. The difference between the SMR-HB and e-NRR at 91 t d^{-1} was smaller than at larger scales, indicating that the e-NRR is more feasible in a small-scale and decentralised manner.

- **Electricity price**: From the sensitivity analysis, it was found that the electricity price had the largest effect on the LCOA, yielding a decrease in the LCOA of 50% by decreasing the price from 0.0863 $ kWh^{-1} to 0.02 $ kWh^{-1}. This concludes that a low electricity market price is vital for the economic viability for the e-NRR.

- **Electrolyzer performance**: Amongst the technical electrolyzer parameters, the faradaic efficiency and current density had the largest impacts on the LCOA, especially when they were reduced to levels below the base case assumptions. From this, one can see that the FE should be above 60%, and that the DoE current density target of 0.3 A cm^{-2} is an appropriate performance target for electrochemical NH_3 synthesis. Nevertheless, the electrolyzer performance metrics proved difficult to accurately forecast, due to the infancy of the e-NRR technology.

  Moreover, it was found that the GDE was is the most practical electrolyzer option for e-NRR. The AEL is likely to be limited due to mass-transfer issues caused by the low N_2 solubility. In essence, the AEL's limiting current density is too low for industrial relevance. Furthermore, while the SOEL's high temperature (550 °C) might increase the e-NRR reaction kinetics, they incur larger process energy consumption due to pre-heating. Another issue is NH_3 decomposition, which reduces the energy efficiency of this electrolyzer.

- **Capital cost**: Electrolyzer cost can considerably decrease the LCOA, but is ambiguous to estimate because there are no commercial e-NRR electrolyzers. Based on H_2O electrolyzer forecasts, it was foreseen that the price of the GDE could be decreased to approximately $2,970. Decreasing the electrolyzer price to this value was found to decrease the LCOA of the GDE PSA process by 37.0%, from 2,605 $ t^{-1} in the base case to 1,643 $ t^{-1}.

This research provided an optimised case with a LCOA of 398 $ t^{-1} for the GDE PSA process at 91 t d^{-1}, considerably lower than the SMR-HB benchmark of 602 $ t^{-1}. This suggests that theoretically, sustainable NH_3 synthesis via e-NRR could reach SMR-HB parity. Nevertheless, the validation of the model's optimistic assumptions proved to be difficult due to the relative infancy of the e-NRR technology. Recent progress and outlooks still prove that the e-NRR is still far away from commercialisation, hence it remains to be seen whether e-NRR can reach industrially relevant performance.

Chapter 6

Recommendations

Electrolyzer Type

This research concerned the application of three types of electrolyzers (AEL, GDE and SOEL) commonly used for the e-NRR. One type that has received significant research attention, the membrane assembly electrolyzer (MEA), was left out due to several reasons. Firstly, NH_3 literature claims that NH_3 can cross-over conventional Nafion membranes, where it accumulates and degrades the performance of the electrolyzer. To overcome this, one can think of the application of anion exchange membranes (AEM), but these types of membranes are not durable and therefore less suitable for industrial application. Nevertheless, recent research efforts [108] show that new AEM's are being developed, which show higher stability. Considering this, it is advised that future research efforts include AEM electrolyzers too.

Electrolyzer Model

The electrolyzers were modelled as black-boxes in this thesis. For the generation of more accurate results, it is advised to develop a more elaborate electrolyzer model, which for instance includes mass transfer (concentration) characteristics. Especially for the AEL system, it is a valuable addition to be able to gauge the exact effect of low N_2 solubility on the mass transfer inside the cell, and its effect on the maximum achievable current density.

The models did not include practical limits for the maximum capacity or scale of the electrolyzers. For the AEL system, 80,000 tonnes of electrolyte was required for the production of one tonne NH_3, resulting in significantly large volumetric inflows. It is uncertain if the electrolyzer can be designed for this, so it is recommended to investigate if the electrolyzer can be scaled to accommodate this volume flux.

In addition, issues with NH_3 decomposition have been identified, which can arise from two possible causes: (1) oxidation of recycled NH_3 at the anode; or (2) NH_3 decomposition at high temperatures. The extent of NH_3 oxidation on the anode depends on several factors, like the oxidation potential of NH_3 and O_2. Moreover, it should be investigated how much NH_3 cross-over occurs, which depends on the membrane. It is advised that more in-depth research should be done on NH_3 decomposition at elevated temperatures.

Water Purification

The necessary pre-treatment of water was neglected in this thesis, while water needs to be of high purity in order to be used in an electrolyzer [96]. It would make the conceptual processes more accurate to include the purification of an existing water source (e.g. industrial waste-water or water from a nearby river) to appropriate purity levels. In other papers, seawater is taken as the water source, and the purification steps (filtering, mechanical vapor compression) were included in their conceptual processes [95, 96]. It is recommended that the exact water purity requirement of the electrolyzers in this research are examined further, and that the necessary purification units are added to conceptual process designs.

Ammonia Storage

The conceptual processes did not include the pressurisation or chilling of NH_3 to storage conditions. Industry-grade NH_3 is usually sold in liquid form [88]. Hence, it would make the model more accurate to include additional post-treatment pressurisation (to 10 bar) or chilling (to -33 °C) to the conceptual processes.

Heat Integration

Heat integration might improve the energy efficiency of the SOEL process. Investigating possible heat integration of the process inlets with the hot exit streams (via a pinch analysis for example) might offer additional process efficiency. Moreover, process integration with industrial waste-heat sources could be also be compelling for the SOEL process. It would be interesting to research the coupling of an existing waste-heat process (like nuclear waste-heat or geothermal energy) with potential high-temperature e-NRR.

Coupling with Intermittent Electricity Pattern
It would be interesting to see the exact effect of intermittency on the e-NRR processes. Some electrolyzer types, like the AEL and SOEL, are less suitable for intermittent operation, which would likely incur additional production costs. Additionally, with intermittent electricity, larger fluctuations in electricity prices can be observed. It would be compelling to investigate how the economic viability of this process is influenced by the peaks and lows of electricity prices.

General Recommendations

The attractiveness of the proposed processes was found to strongly depend on the technical performance (i.e. FE, J, η) of the electrolyzer. At the current state-of-the-art, e-NRR technology is nowhere near commercialisation, as it is troubled by low FE's (<30%), low operational current densities ($<0.3 \cdot 10^{-3}$ A cm^{-1}), and the achieved NH$_3$ production rates (10^{-9} mol s^{-1} cm^{-1}) are far below industrial relevance (at least 10^{-6} mol s^{-1} cm^{-1}). Considering that the electrolyzer parameter assumptions in this work are considerable more optimistic than state-of-the-art, the results were difficult to verify. Hence, it can be argued that the primary objective of e-NRR research should be about developing lab-scale electrolyzers with commercially relevant performance. Before this type of performance is reached in the lab, it is arduous to accurately assess the market-potential of the e-NRR technology.

Outlook

Considering the infancy of e-NRR, electrified HB or SMR-HB with CCS presently look more appropriate options for sustainable NH$_3$ synthesis, which is primarily caused by the vast experience and robustness of the Haber-Bosch technology. It is equally observed that the majority of newly commissioned NH$_3$ production facilities are e-HB plants [28], indicating that the industry is starting to move towards lower CO$_2$ emissions via electrified HB processes. Nonetheless, due to the inherent upsides of electrochemical NH$_3$ synthesis, like its practical intermittent operation, the presented conceptual process could be a promising future option for power-to-NH$_3$ processes.

Bibliography

[1] Lori Apodaca. Nitrogen Data Sheet - Mineral Commodity Summaries . Technical report, National Minerals Information Center, 2015. Available at: https://pubs.usgs.gov/periodicals/mcs2020/mcs2020-nitrogen.pdf.

[2] Cornelis J M van der Ham, Marc T M Koper, and Dennis G H Hetterscheid. Challenges in reduction of dinitrogen by proton and electron transfer. *Chem. Soc. Rev*, 43:5183, 2014.

[3] Douglas R. MacFarlane, Pavel V. Cherepanov, Jaecheol Choi, Bryan H.R. Suryanto, Rebecca Y. Hodgetts, Jacinta M. Bakker, Federico M. Ferrero Vallana, and Alexandr N. Simonov. A Roadmap to the Ammonia Economy. 4(6):1186–1205, 6 2020.

[4] Vaclav Smil. Detonator of the population explosion. *Nature*, 400(6743):415, 1999.

[5] Collin Smith, Alfred K. Hill, and Laura Torrente-Murciano. Current and future role of Haber-Bosch ammonia in a carbon-free energy landscape. *Energy and Environmental Science*, 13(2):331–344, 2 2020.

[6] The Royal Society. Ammonia: zero-carbon fertiliser, fuel and energy store, Policy Briefing, 2020. Available at: https://royalsociety.org/topics-policy/projects/low-carbon-energy-programme/green-ammonia/.

[7] Miao Wang, Mohd A. Khan, Imtinan Mohsin, Joshua Wicks, Alexander H. Ip, Kazi Z. Sumon, Cao Thang Dinh, Edward H. Sargent, Ian D. Gates, and Md Golam Kibria. Can sustainable ammonia synthesis pathways compete with fossil-fuel based Haber-Bosch processes? *Energy and Environmental Science*, 14(5):2535–2548, 5 2021.

[8] Rong Lan, Shanwen Tao, Shaorong Wang, and Wei Zhou. Ammonia as a suitable fuel for fuel cells. *Front. Energy Res*, 2014.

[9] Caneon Kurien and Mayank Mittal. Review on the production and utilization of green ammonia as an alternate fuel in dual-fuel compression ignition engines. *Energy Conversion and Management*, 251:114990, 2022.

[10] Agustin Valera-Medina and Rene Banares-Alcantara. Chapter 1 - introduction. In *Techno-Economic Challenges of Green Ammonia as an Energy Vector*, pages 1–14. Academic Press, 2021.

[11] Fadhil Y Al-Aboosi, Mahmoud M El-Halwagi, Margaux Moore, and Rasmus B Nielsen. Renewable ammonia as an alternative fuel for the shipping industry. *Current Opinion in Chemical Engineering*, 31:100670, 2021.

[12] *Ammonia Technology Roadmap: Towards more sustainable nitrogen fertiliser production*. International Energy Agency (IEA), Paris, 2020. Available at: https://www.iea.org/reports/ammonia-technology-roadmap.

[13] Grigorii Soloveichik, M Acharya, H Cheeseman, D Wicks, and D Tew. Renewable energy to fuels through utilization of energy dense liquids (REFUEL). *US DOE*, 2016. Available at: https://arpa-e.energy.gov/sites/default/files/documents/files/REFUEL_ProgramOverview.pdf.

[14] Fior Markets. Global Ammonia Market is Expected to Reach USD 81.42 Billion by 2025, 3 2019. Available at: https://www.fiormarkets.com/report/global-ammonia-market-by-product-form-liquid-gas-375934.html.

[15] Yusuf Bicer, Ibrahim Dincer, Calin Zamfirescu, Greg Vezina, and Frank Raso. Comparative life cycle assessment of various ammonia production methods. *Journal of Cleaner Production*, 135:1379–1395, 2016.

[16] NASA's Goddard Institute for Space Studies (GISS). Global Land-Ocean Temperature Index, 8 2022. Available at: `https://climate.nasa.gov/vital-signs/global-temperature/`.

[17] United Nations Environment Programme. Paris Climate Agreement, 12 2015. Available at: `https://wedocs.unep.org/handle/20.500.11822/20830`, institution = United Nations.

[18] European Commission Directorate-General for Communication. European green deal : delivering on our targets. Technical report, 2021. Available at: `https://ec.europa.eu/commission/presscorner/api/files/attachment/869807/EGD_brochure_EN.pdf.pdf`.

[19] Jens Nørskov, Jingguang Chen, Raul Miranda, Tim Fitzsimmons, and Robert Stack. Sustainable ammonia synthesis – exploring the scientific challenges associated with discovering alternative, sustainable processes for ammonia production. 2 2016.

[20] Kevin H. R. Rouwenhorst, Piotr M. Krzywda, Nieck E. Benes, Guido Mul, and Leon Lefferts. *Ammonia, 4. Green Ammonia Production*, pages 1–20. John Wiley & Sons, Ltd, 2020.

[21] Bing Yang, Weilu Ding, Honghua Zhang, and Suojiang Zhang. Recent progress in electrochemical synthesis of ammonia from nitrogen: strategies to improve the catalytic activity and selectivity. *Energy Environ. Sci.*, 14:672–687, 2021.

[22] Gal Hochman, Alan S. Goldman, Frank A. Felder, James M. Mayer, Alexander J.M. Miller, Patrick L. Holland, Leo A. Goldman, Patricia Manocha, Ze Song, and Saketh Aleti. Potential Economic Feasibility of Direct Electrochemical Nitrogen Reduction as a Route to Ammonia. *ACS Sustainable Chemistry and Engineering*, 8(24):8938–8948, 6 2020.

[23] Carlos A. Fernandez and Marta C. Hatzell. Economic Considerations for Low-Temperature Electrochemical Ammonia Production: Achieving Haber-Bosch Parity. *Journal of The Electrochemical Society*, 167(14):143504, 11 2020.

[24] Kevin H R Rouwenhorst and Gabriel Castellanos. 1921–2021: A Century of Renewable Ammonia Synthesis. *Sustainable Chemistry*, 3(2):149–171, 4 2022.

[25] Kevin Hendrik Reindert Rouwenhorst, Piotr Marek Krzywda, Nieck E Benes, Guido Mul, and Leon Lefferts. Ammonia production technologies. *Techno-Economic Challenges of Green Ammonia as Energy Vector*, pages 41–84, 2020.

[26] Nick Böcker, Matthias Grahl, Akos Tota, Peter Häussinger, Paul Leitgeb, and Bernd Schmücker. Nitrogen. In *Ullmann's Encyclopedia of Industrial Chemistry*, pages 1–27. Wiley-VCH Verlag GmbH & Co. KGaA, Weinheim, Germany, 10 2013.

[27] Max Appl. *Ammonia, 2. Production Processes*. Wiley-VCH Verlag GmbH & Co. KGaA, 10 2011.

[28] Kevin H R Rouwenhorst and Gabriel Castellanos. Innovation Outlook: Renewable Ammonia, 2022. Available at: `https://www.irena.org/publications/2022/May/Innovation-Outlook-Renewable-Ammonia`.

[29] Trevor Brown. The capital intensity of small-scale ammonia plants, 2018. Available at: `https://www.ammoniaenergy.org/articles/the-capital-intensity-of-small-scale-ammonia-plants/`.

[30] Eric W Lemmon. Thermophysical properties of fluid systems. *NIST Chemistry WebBook: NIST Standard Reference Database Number 69*, 20899, 1998.

[31] Boaz Izelaar. Discussing the feasibility of different sustainable ammonia production pathways. *in preparation*.

[32] Hanfei Zhang, Ligang Wang, Jan Van herle, François Maréchal, and Umberto Desideri. Techno-economic comparison of green ammonia production processes. *Applied Energy*, 259, 2 2020.

[33] Mar Pérez-Fortes, Andrei Bocin-Dumitriu, and Evangelos Tzimas. Co2 utilization pathways: Techno-economic assessment and market opportunities. *Energy Procedia*, 63:7968–7975, 2014. 12th International Conference on Greenhouse Gas Control Technologies, GHGT-12.

[34] Abdullah Emre Yüzbaşıoğlu, Ali Hikmet Tatarhan, and Ahmet Ozan Gezerman. Decarbonization in ammonia production, new technological methods in industrial scale ammonia production and critical evaluations. *Heliyon*, 7(10):e08257, 2021.

[35] Alexander Buttler and Hartmut Spliethoff. Current status of water electrolysis for energy storage, grid balancing and sector coupling via power-to-gas and power-to-liquids: A review. *Renewable and Sustainable Energy Reviews*, 82:2440–2454, 2018.

[36] Wei Bi, Nima Shaigan, Ali Malek, Khalid Fatih, Előd Gyenge, and David P. Wilkinson. Strategies in cell design and operation for the electrosynthesis of ammonia: status and prospects. *Energy & Environmental Science*, 15(6):2259–2287, 2022.

[37] Rong Lan, John T.S. Irvine, and Shanwen Tao. Synthesis of ammonia directly from air and water at ambient temperature and pressure. *Scientific Reports*, 3, 1 2013.

[38] Grigorii Soloveichik. Electrochemical synthesis of ammonia as a potential alternative to the Haber–Bosch process. *Nature Catalysis*, 2(5):377–380, 5 2019.

[39] W. Wang, X. Wei, D. Choi, X. Lu, G. Yang, and C. Sun. Chapter 1 - electrochemical cells for medium- and large-scale energy storage: fundamentals. In Chris Menictas, Maria Skyllas-Kazacos, and Tuti Mariana Lim, editors, *Advances in Batteries for Medium and Large-Scale Energy Storage*, Woodhead Publishing Series in Energy, pages 3–28. Woodhead Publishing, 2015.

[40] Geoffrey Prentice. Electrochemical engineering. In Robert A. Meyers, editor, *Encyclopedia of Physical Science and Technology (Third Edition)*, pages 143–159. Academic Press, New York, third edition edition, 2003.

[41] Antonio José Martín, Tatsuya Shinagawa, and Javier Pérez-Ramírez. Electrocatalytic Reduction of Nitrogen: From Haber-Bosch to Ammonia Artificial Leaf. *Chem*, 5(2):263–283, 2 2019.

[42] Xiaoyang Cui, Cheng Tang, and Qiang Zhang. A Review of Electrocatalytic Reduction of Dinitrogen to Ammonia under Ambient Conditions. *Advanced Energy Materials*, 2018.

[43] Bryan H.R. Suryanto, Colin S.M. Kang, Dabin Wang, Changlong Xiao, Fengling Zhou, Luis Miguel Azofra, Luigi Cavallo, Xinyi Zhang, and Douglas R. Macfarlane. Rational Electrode-Electrolyte Design for Efficient Ammonia Electrosynthesis under Ambient Conditions. *ACS Energy Letters*, 3(6):1219–1224, 6 2018.

[44] Huidong Shen, Changhyeok Choi, Justus Masa, Xin Li, Jieshan Qiu, Yousung Jung, and Zhenyu Sun. Electrochemical ammonia synthesis: Mechanistic understanding and catalyst design. *Chem*, 7(7):1708–1754, 7 2021.

[45] Egill Skúlason, Thomas Bligaard, Sigríður Gudmundsdóttir, Felix Studt, Jan Rossmeisl, Frank Abild-Pedersen, Tejs Vegge, Hannes Jónsson, and Jens K. Nørskov. A theoretical evaluation of possible transition metal electro-catalysts for N2 reduction. *Physical Chemistry Chemical Physics*, 14(3):1235–1245, 1 2012.

[46] Emil Dražević and Egill Skúlason. Are There Any Overlooked Catalysts for Electrochemical NH3 Synthesis—New Insights from Analysis of Thermochemical Data. *iScience*, 23(12):101803, 12 2020.

[47] Boaz Izelaar, Davide Ripepi, Simone Asperti, A Iulian Dugulan, Ruud W A Hendrikx, Amarante J Böttger, Fokko M Mulder, and Ruud Kortlever. Revisiting the Electrochemical Nitrogen Reduction on Molybdenum and Iron Carbides: Promising Catalysts or False Positives? *ACS Catalysis*, 13:1649–1661, 2023.

[48] Geletu Qing, Reza Ghazfar, Shane T. Jackowski, Faezeh Habibzadeh, Mona Maleka Ashtiani, Chuan Pin Chen, Milton R. Smith, and Thomas W. Hamann. Recent Advances and Challenges of Electrocatalytic N2Reduction to Ammonia. *Chemical Reviews*, 120(12):5437–5516, 6 2020.

[49] Yao Yao, Jing Wang, Usman Bin Shahid, Meng Gu, Haijiang Wang, Hui Li, and Minhua Shao. Electrochemical Synthesis of Ammonia from Nitrogen Under Mild Conditions: Current Status and Challenges. *Electrochemical Energy Reviews*, 3(2):239–270, 6 2020.

[50] Caiwu Liang, Peichao Zou, Adeela Nairan, Yongqi Zhang, Jiaxing Liu, Kangwei Liu, Shengyu Hu, Feiyu Kang, Hong Jin Fan, and Cheng Yang. Exceptional performance of hierarchical Ni-Fe oxyhydroxide@NiFe alloy nanowire array electrocatalysts for large current density water splitting. *Energy and Environmental Science*, 13(1):86–95, 1 2020.

[51] V Kyriakou, I Garagounis, E Vasileiou, A Vourros, and M Stoukides. Progress in the electrochemical synthesis of ammonia. *Catalysis Today*, 286:2–13, 2017.

[52] Philip H Rieger. *Electrochemistry*. Springer Science & Business Media, 1993.

[53] Seval Gunduz, Dhruba J. Deka, and Umit S. Ozkan. A review of the current trends in high-temperature electrocatalytic ammonia production using solid electrolytes. *Journal of Catalysis*, 387:207–216, 7 2020.

[54] Ioannis Garagounis, Anastasios Vourros, Demetrios Stoukides, Dionisios Dasopoulos, and Michael Stoukides. Electrochemical synthesis of ammonia: Recent efforts and future outlook. *Membranes*, 9(9), 9 2019.

[55] Martha Ouzounidou, Aglaia Skodra, Christos Kokkofitis, and Michael Stoukides. Catalytic and electrocatalytic synthesis of NH3 in a H+ conducting cell by using an industrial Fe catalyst. *Solid State Ionics*, 178(1-2):153–159, 2007.

[56] R. J. Gilliam, J. W. Graydon, D. W. Kirk, and S. J. Thorpe. A review of specific conductivities of potassium hydroxide solutions for various concentrations and temperatures. *International Journal of Hydrogen Energy*, 32(3):359–364, 3 2007.

[57] Hoang-Long Du, Rebecca Y. Hodgetts, Manjunath Chatti, Cuong K. Nguyen, Douglas R. Macfarlane, and Alexandr N. Simonov. Is molybdenum disulfide modified with molybdenum metal catalytically active for the nitrogen reduction reaction? *Journal of The Electrochemical Society*, 167(14):146507, oct 2020.

[58] Huangang Shi, Chao Su, Ran Ran, Jiafeng Cao, and Zongping Shao. Electrolyte materials for intermediate-temperature solid oxide fuel cells. *Progress in Natural Science: Materials International*, 30(6):764–774, 2020.

[59] Martin Kolen, Davide Ripepi, Wilson A Smith, Thomas Burdyny, and Fokko M Mulder. Overcoming Nitrogen Reduction to Ammonia Detection Challenges: The Case for Leapfrogging to Gas Diffusion Electrode Platforms. *ACS Catalysis*, 12(10):5726–5735, 5 2022.

[60] Lin Hu, Zhuo Xing, and Xiaofeng Feng. Understanding the electrocatalytic interface for ambient ammonia synthesis. *ACS Energy Letters*, 5(2):430–436, 2020.

[61] Usman Bin Shahid, Yifu Chen, Shuang Gu, Wenzhen Li, and Minhua Shao. Electrochemical nitrogen reduction: an intriguing but challenging quest. *Trends in Chemistry*, 4(2):142–156, 2022.

[62] Mahinder Ramdin, Bert De Mot, Andrew R.T. Morrison, Tom Breugelmans, Leo J.P. Van Den Broeke, J. P.Martin Trusler, Ruud Kortlever, Wiebren De Jong, Othonas A. Moultos, Penny Xiao, Paul A. Webley, and Thijs J.H. Vlugt. Electroreduction of CO2/CO to C2Products: Process Modeling, Downstream Separation, System Integration, and Economic Analysis. *Industrial and Engineering Chemistry Research*, 60(49):17862–17880, 12 2021.

[63] Jong Hyun Park, Hyung Chul Yoon, Jong Nam Kim, Chan Hee Jeong, Eun Young Jeong, Dae Sik Yun, Hana Yoon, Sang Hyun Park, Moon Hee Han, and Chung Yul Yoo. Anion-exchange-membrane-based electrochemical synthesis of ammonia as a carrier of hydrogen energy. *Korean Journal of Chemical Engineering*, 35(8):1620–1625, 8 2018.

[64] The Linde Group. Air Separation Plants. History and technological progress in the course of time. Available at: https://www.linde-engineering.com/en/images/Air-separation-plants-history-and-technological-progress-2019_tcm19-457349.pdf.

[65] Air Products. PRISM® On-site Cryogenic Nitrogen Plants and Services, 2013. Available at: https://www.airproducts.com/supply-modes/gen-gas-on-site/onsite-nitrogen-generation/cryogenic-nitrogen-plant.

[66] Air Products. PRISM® PSA Nitrogen Generation System, 2017. Available at: https://www.airproducts.com/-/media/airproducts/files/en/522/522-17-004-glb-prism-psa-nitrogen-generation-system.pdf.

[67] Svetlana Ivanova and Robert Lewis. Producing nitrogen via pressure swing adsorption. *Chemical Engineering Progress*, 108(6):38–42, 2012.

[68] Aravind Krishnamoorthy, Ken-ichi Nomura, Nitish Baradwaj, Kohei Shimamura, Ruru Ma, Shogo Fukushima, Fuyuki Shimojo, Rajiv K. Kalia, Aiichiro Nakano, and Priya Vashishta. Hydrogen bonding in liquid ammonia. *The Journal of Physical Chemistry Letters*, 13(30):7051–7057, 2022. PMID: 35900140.

[69] United States Environmental Protection Agency. Wastewater Technology Fact Sheet Ammonia Stripping. Technical report, 2000. Available at: `http://www.epa.gov/owmitnet/mtbfact.htm`.

[70] Max Appl. *Ammonia, 3. Production Plants*. 10 2011.

[71] Engineering ToolBox. Ammonia - vapour pressure at gas-liquid equilibrium., 2003. Available at: `https://www.engineeringtoolbox.com/ammonia-pressure-temperature-d_361.html`.

[72] K Kugler, B Ohs, M Scholz, and M Wessling. Towards a carbon independent and CO 2-free electrochemical membrane process for NH 3 synthesis †. *Phys. Chem. Chem. Phys*, 16:6129, 2014.

[73] T Brown. A 100 short-ton-per-day plant was completed in Nebraska in 2018 at a cost of \$75 M or \$826,000 per MT-NH3/day capacity. Available at: `https://ammoniaindustry.com/geneva-ne-fortigen/`.

[74] T Brown. A 600 short-ton-per-day plant was reported to be built in Rock Springs, WY for a cost of \$350 M, or \$643,000 per MT-NH3/day capacity, 2014. Available at: `https://ammoniaindustry.com/rock-springs-wy-simplot/`.

[75] Nel Hydrogen. Atmospheric Alkaline Electrolyser. Available at: `https://nelhydrogen.com/product/atmospheric-alkaline-electrolyser-a-series/`.

[76] Yu-Chen Hao, Yu Guo, Li-Wei Chen, Miao Shu, Xin-Yu Wang, Tong-An Bu, Wen-Yan Gao, Nan Zhang, Xin Su, Xiao Feng, Jun-Wen Zhou, Bo Wang, Chang-Wen Hu, An-Xiang Yin, Rui Si, Ya-Wen Zhang, and Chun-Hua Yan. Promoting nitrogen electroreduction to ammonia with bismuth nanocrystals and potassium cations in water. *Nature Catalysis*, 2(5):448–456, 2019.

[77] Jaecheol Choi, Bryan H.R. Suryanto, Dabin Wang, Hoang Long Du, Rebecca Y. Hodgetts, Federico M. Ferrero Vallana, Douglas R. MacFarlane, and Alexandr N. Simonov. Identification and elimination of false positives in electrochemical nitrogen reduction studies. *Nature Communications*, 11(1), 12 2020.

[78] Matheus T. de Groot and Albertus W. Vreman. Ohmic resistance in zero gap alkaline electrolysis with a zirfon diaphragm. *Electrochimica Acta*, 369:137684, 2021.

[79] R.J. Gilliam, J.W. Graydon, D.W. Kirk, and S.J. Thorpe. A review of specific conductivities of potassium hydroxide solutions for various concentrations and temperatures. *International Journal of Hydrogen Energy*, 32(3):359–364, 2007. Fuel Cells.

[80] M Chase. *NIST-JANAF Thermochemical Tables, 4th Edition*. American Institute of Physics, -1, 1998-08-01 1998. Available at: `https://webbook.nist.gov/chemistry/name-ser/`.

[81] Marian Chatenet, Bruno G Pollet, Dario R Dekel, Fabio Dionigi, Jonathan Deseure, Pierre Millet, Richard D Braatz, Martin Z Bazant, Michael Eikerling, and Iain Staffell. Water electrolysis: from textbook knowledge to the latest scientific strategies and industrial developments. *Chemical Society Reviews*, 2022.

[82] Brian D James, Jennie Huya-Kouadio, Yaset Acevedo, and Kevin McNamara. Liquid Alkaline Electrolysis Techno-Economic Review, 2021. Available at: `https://www.energy.gov/sites/default/files/2022-02/7-TEA-Liquid%20Alkaline%20Workshop.pdf`.

[83] Vasileios Kyriakou, Ioannis Garagounis, Anastasios Vourros, Eirini Vasileiou, and Michael Stoukides. An Electrochemical Haber-Bosch Process. *Joule*, 4(1):142–158, 1 2020.

[84] Thomas Holm, Tory Borsboom-Hanson, Omar E. Herrera, and Walter Mérida. Hydrogen costs from water electrolysis at high temperature and pressure. *Energy Conversion and Management*, 237, 6 2021.

[85] Pawan Dubey, Kevin Lee, Anisur Rahman, Ashish Aphale, Seraphim Belko, Junsung Hong, and Michael (Hydro-Gen) Reisert. Proton-Conducting Solid Oxide Electrolysis Cells for Large-scale Hydrogen Production at Intermediate Temperatures, 2022. Available at: `https://www.hydrogen.energy.gov/pdfs/review20/p152_singh_2020_p.pdf`.

[86] Antonio Sánchez and Mariano Martín. Scale up and scale down issues of renewable ammonia plants: Towards modular design. *Sustainable Production and Consumption*, 16:176–192, 10 2018.

[87] Charles W. Forsberg, Daniel C. Stack, Daniel Curtis, Geoffrey Haratyk, and Nestor Andres Sepulveda. Converting excess low-price electricity into high-temperature stored heat for industry and high-value electricity production. *The Electricity Journal*, 30(6):42–52, 7 2017.

[88] Max Appl. *Ammonia, 1. Introduction.* 10 2011.

[89] Deanne van der Slikke. An Electrochemical Ammonia Synthesis Process: Process Model and Design of a Medium Scale Electrochemical Ammonia Production Plant. 2021. Available at: `https://repository.tudelft.nl`.

[90] Robin Smith. *Chemical process: design and integration*. John Wiley & Sons, 2005.

[91] María Yáñez, Frederico Relvas, Alfredo Ortiz, Daniel Gorri, Adélio Mendes, and Inmaculada Ortiz. PSA purification of waste hydrogen from ammonia plants to fuel cell grade. *Separation and Purification Technology*, 240:116334, 2020.

[92] Robin Smith. *Chemical process: design and integration; Chapter 2: Process Economics*. John Wiley & Sons, 2005.

[93] Kenneth K Humphreys. *Project and cost engineers' handbook*. CRC Press, 2004.

[94] Max Stone Peters, Klaus D Timmerhaus, and Ronald Emmett West. *Plant design and economics for chemical engineers*, volume 4. McGraw-hill New York, 2003.

[95] Eric R Morgan. *Techno-economic feasibility study of ammonia plants powered by offshore wind*. University of Massachusetts Amherst, 2013.

[96] Rene Bañares-Alcántara. Analysis of Islanded NH3-based Energy Storage Systems. *Department of Engineering Science, University of Oxford*, 2016.

[97] Clean Hydrogen Joint Undertaking. Strategic Research and Innovation: Agenda (SRIA) 2021 – 2027, 2020. Available at: `https://www.clean-hydrogen.europa.eu/about-us/key-documents/strategic-research-and-innovation-agenda_en`.

[98] US Department of Energy. Water and Wastewater Annual Price Escalation Rates for Selected Cities across the United States. Technical report, EERE Publication and Product Library, 10 2017.

[99] EIA. Electric Power Monthly: Table 5.6.A. Average Price of Electricity to Ultimate Customers by End-Use Sector, 2022. Available at: `https://www.eia.gov/electricity/monthly/epm_table_grapher.php?t=epmt_5_6_a`.

[100] Bureau of Labor Statistics. Employer Cost for Employee Componsation - December 2022, 2022. Available at: `https://www.bls.gov/news.release/pdf/ecec.pdf`, institution = U.S. Department of Labor.

[101] OECD. *OECD Compendium of Productivity Indicators 2023*. OECD, 2 2023. Available at: `https://www.oecd.org/global-forum-productivity/researchandimpact/oecd-compendium-of-productivity-indicators-22252126.htm`.

[102] Intratex. Oxygen price, 2018. Available at: `https://www.intratec.us/chemical-markets/oxygen-price`.

[103] Paris IEA. Global average levelised cost of hydrogen production by energy source and technology, 2019 and 2050, 2022. Available at: `https://www.iea.org/reports/global-hydrogen-review-2021/executive-summary`.

[104] Ibrahim Dincer and Yusuf Bicer. 3.2 Ammonia Production. *Comprehensive Energy Systems*, 3-5:41–94, 1 2018.

[105] Sunfire Hydrogen (previously IHT). High pressure alkaline electrolyzer, 2015. Available at: `https://hidrogenoaragon.org/wp-content/uploads/2015/03/electrolizador_en.pdf`.

[106] EIA. Levelized Costs of New Generation Resources in the Annual Energy Outlook 2022, 3 2022. Available at: `https://www.eia.gov/outlooks/aeo/electricity_generation.php`.

[107] Richard Nayak-Luke, René Bañares-Alcántara, and Ian Wilkinson. "green" ammonia: Impact of renewable energy intermittency on plant sizing and levelized cost of ammonia. *Industrial & Engineering Chemistry Research*, 57(43):14607–14616, 2018.

[108] Dirk Henkensmeier, Malikah Najibah, Corinna Harms, Jan Žitka, Jaromír Hnát, and Karel Bouzek. Overview: State-of-the Art Commercial Membranes for Anion Exchange Membrane Water Electrolysis. *Journal of Electrochemical Energy Conversion and Storage*, 18(2), 08 2020. 024001.

[109] Peter Atkins, Peter William Atkins, and Julio de Paula. *Atkins' physical chemistry*. Oxford university press, 2014.

Appendix

A Thermodynamics of the e-NRR

A.1 Derivation of Standard Equilibrium Cell Potential

The overall reaction of direct electrochemical ammonia synthesis can be seen below:

$$0.5\,N_2(g) + 1.5\,H_2O\,(l) \longrightarrow 0.75\,O_2(g) + NH_3\,(g) \tag{6.1}$$
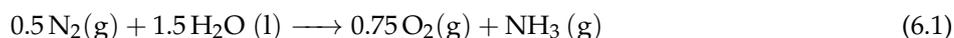
In Table A.1, the thermodynamic properties (enthalpy and entropy) of the constituents of e-NRR at STP (25 °C, 1.0135 bar) is listed. For NH_3, one can either assume the compound to be dissolved in water (since it dissolves readily in aqueous environments) or in a gaseous state.

Table A.1: Thermodynamic data on eNRR reaction. Enthalpy and entropy of formation data obtained from *Physical Chemistry* by Atkins [109]

Compound	h_f^0 (kJ/mol)	s_f^0 (J/molK)
N_2 (g)	0	191.5
H_2O (l)	-285.83	69.95
O_2 (g)	0	205.03
NH_3 (aq)	-80.29	111.3
NH_3 (g)	-46.19	192.33

First, ΔH^0 and ΔS^0 of the reaction are calculated, after which the Gibbs Free energy of formation is calculated via equation 6.2, which can be converted to the cell potential E_{cell}^0 through Faraday's law. For NH_3 (g), E_{cell}^0 = -1.17 V, and for NH_3 (aq), E_{cell}^0 = -1.14 V.

$$\Delta G^0 = \Delta H^0 - T\Delta S^0 \tag{6.2}$$

A.2 Derivation of Half-reaction Potentials

The e-NRR half reactions for (a) acidic and (b) alkaline environments are showcased below:

a. Acidic

$$\text{NRR:} \quad N_2 + 6\,H^+ + 6\,e^- \longrightarrow 2\,NH_3 \tag{6.3}$$

$$\text{OER:} \quad 2\,H_2O \longrightarrow 4\,H^+ + O_2 + 4\,e^- \tag{6.4}$$

b. Alkaline

$$\text{NRR:} \quad N_2 + 6\,H_2O + 6\,e^- \longrightarrow 2\,NH_3 + 6\,OH^- \tag{6.5}$$

$$\text{OER:} \quad 6\,OH^- \longrightarrow 1.5\,O_2 + 3\,H_2O + 6\,e^- \tag{6.6}$$
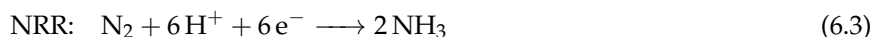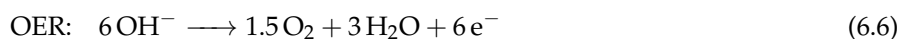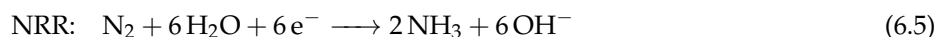
The table below summarises the half-cell potentials for the reactions in acidic (pH 0) and alkaline (pH 14) environments. Also, the distinction is made whether NH_3 is formed in the aqueous or gaseous phase. At

last, the corresponding cell types for each condition are given (for instance, the PEM will function in an acidic environment and NH_3 will form as a gas).

Table A.2: The standard redox potential for cathodic (E^0_{cat}) and anodic (E^0_{an}) reactions at STC, as well as the cell potential (E^0_{cell}), at different pH.

	NH3 (aq) - AEL, GDE	NH3(g) - MEA, SOEL
pH 0 - PEM	$E^0_{cat} = +0.06 \ V_{SHE}$ $E^0_{an} = +1.23 \ V_{SHE}$ $E^0_{cell} = -1.17 \ V_{SHE}$	$E^0_{cat} = +0.09 \ V_{SHE}$ $E^0_{an} = +1.23 \ V_{SHE}$ $E^0_{cell} = -1.14 \ V_{SHE}$
pH 14 - AEM, AEL, GDE	$E^0_{cat} = -0.77 \ V_{SHE}$ $E^0_{an} = +0.40 \ V_{SHE}$ $E^0_{cell} = -1.17 \ V_{SHE}$	$E^0_{cat} = -0.74 \ V_{SHE}$ $E^0_{an} = +0.40 \ V_{SHE}$ $E^0_{cell} = -1.14 \ V_{SHE}$

A.3 Thermodynamic Temperature Dependence

The thermodynamic temperature dependence of ΔG, ΔH, $T\Delta S$ and E^0_{cell} are shown in the following figures. The calculations were done via the provided Shomate equations (Equation 6.7) and corresponding NIST data [80] of H_2O, N_2, NH_3 and O_2.

$$H° - H°298.15 = A^\star t + B^\star t^2/2 + C^\star t^3/3 + D^\star t^4/4 - E/t + F - H$$

$$S° = A^\star \ln(t) + B^\star t + C^\star t^2/2 + D^\star t^3/3 - E/\left(2^\star t^2\right) + G$$

(6.7)

ΔG was calculated through $G \equiv H - TS$. The reversible cell potential (E^0_{cell}) was calculated through Faraday's law.
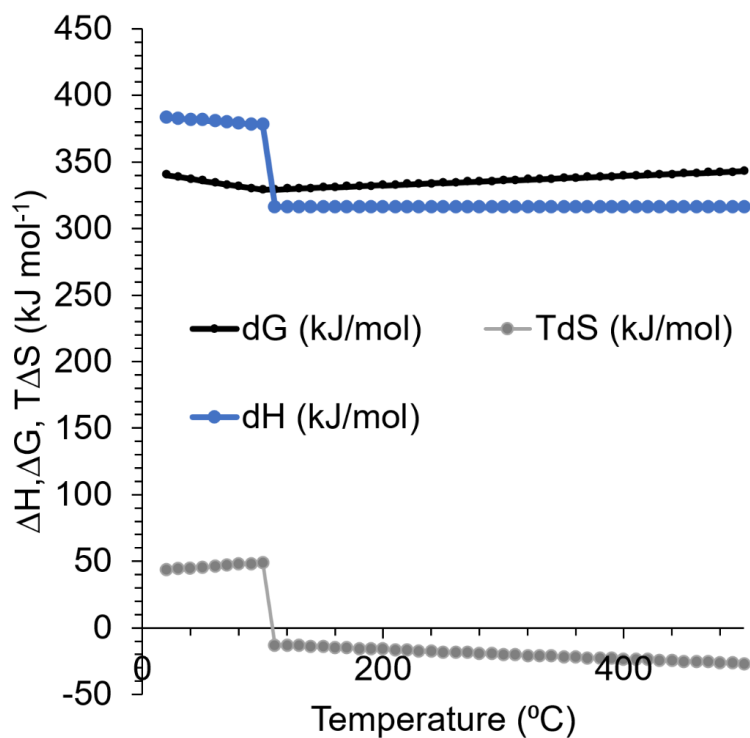
Figure A.1: Temperature dependence of ΔG (black), ΔH (blue) and $T\Delta S$ (grey) of direct e-NRR ($H_2O + N_2 \longrightarrow NH_3 + O_2$) at different temperatures.
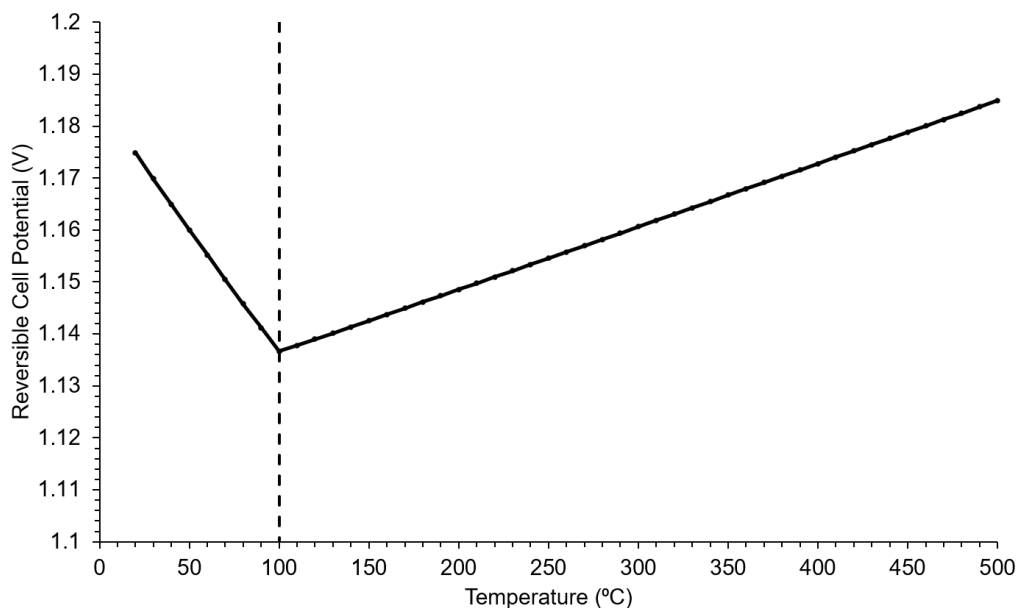
Figure A.2: Temperature dependence of reversible cell potential (E^0_{cell}).

B Supplementary Results

B.1 Energy Consumption and OPEX, per Source

The following figures contain information on the type of energy flow (Figure B.3) (i.e. imported steam and cooling water, and electricity); and different operational expenses (Figure B.4) (i.e. imported steam and cooling water, electricity, raw materials and miscellaneous (other)) for the different electrolyzer processes.
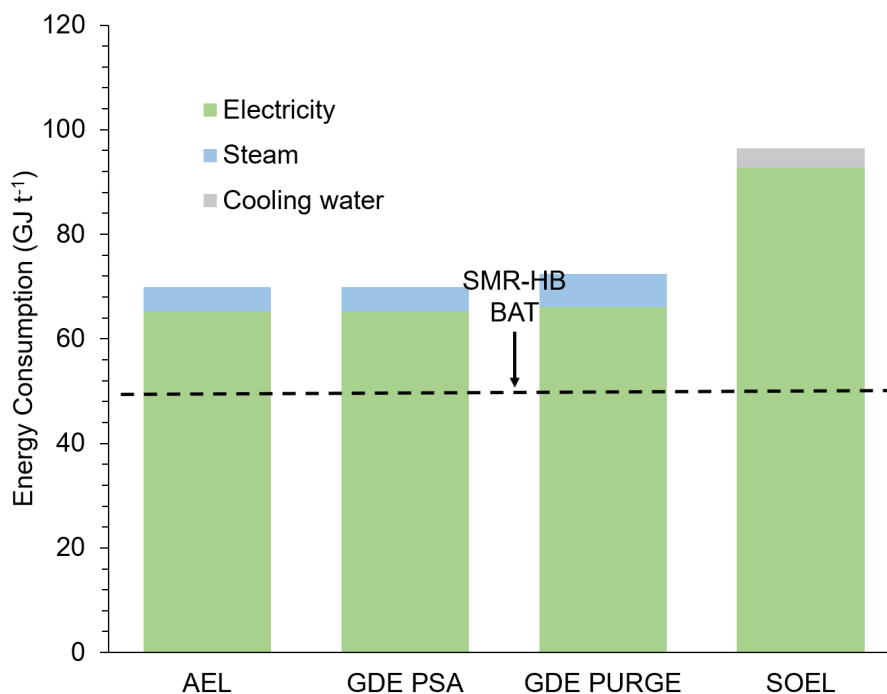
Figure B.3: Energy consumption per type (GJ t^{-1}), shown for the 2055 t d^{-1} scenario.
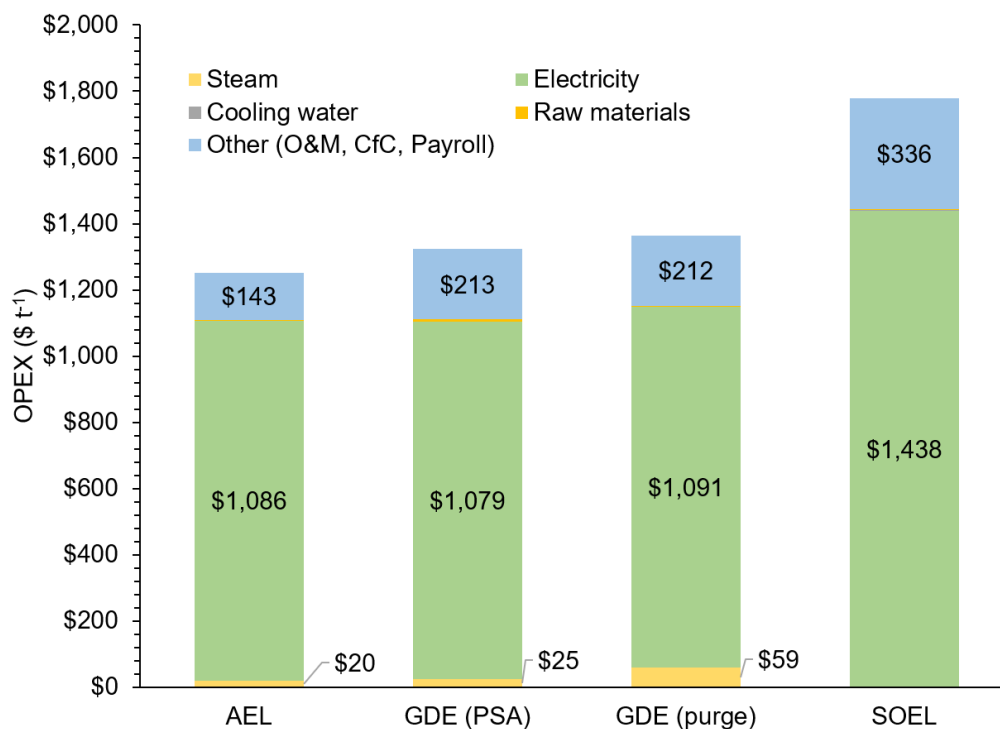
Figure B.4: Operational expenses per type($ t^{-1}), shown for the 2055 t d^{-1} scenario.

B.2 Capital Intensity

The following figures show the capital intensity contributions for all processes (AEL process, GDE PSA process, GDE purge process and SOEL process) for the 2055 t d^{-1} scale.
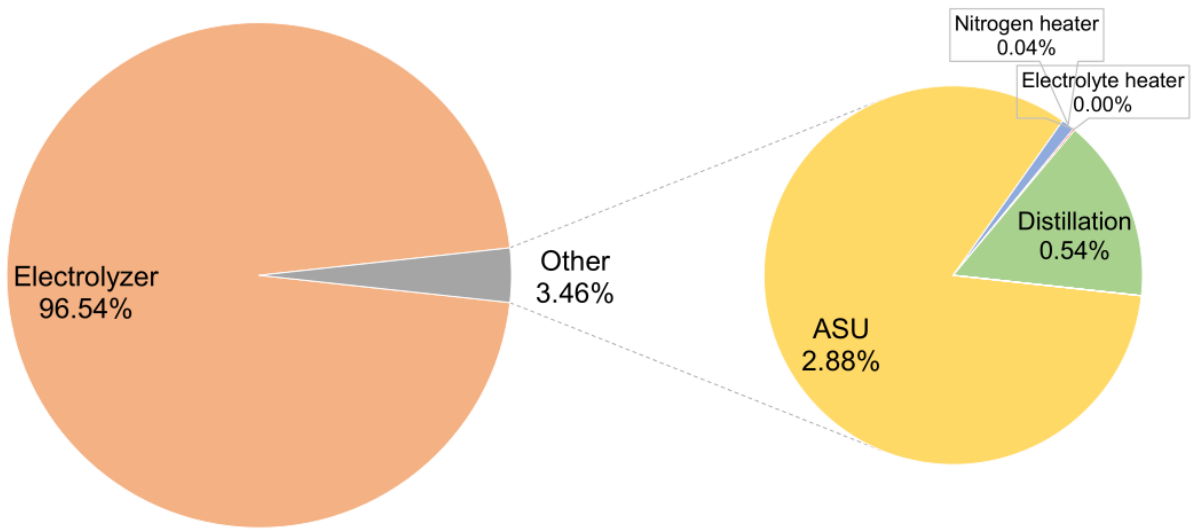
Figure B.5: AEL process capital intensity for 2055 t d^{-1}.
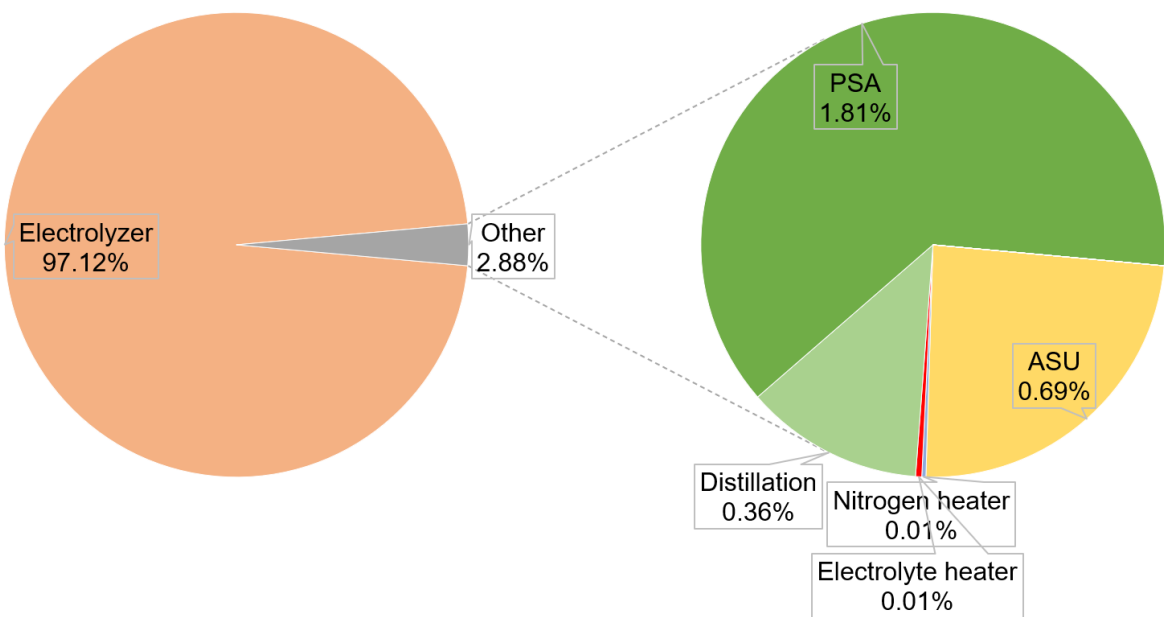
Figure B.6: GDE PSA process capital intensity for 2055 t d^{-1}.
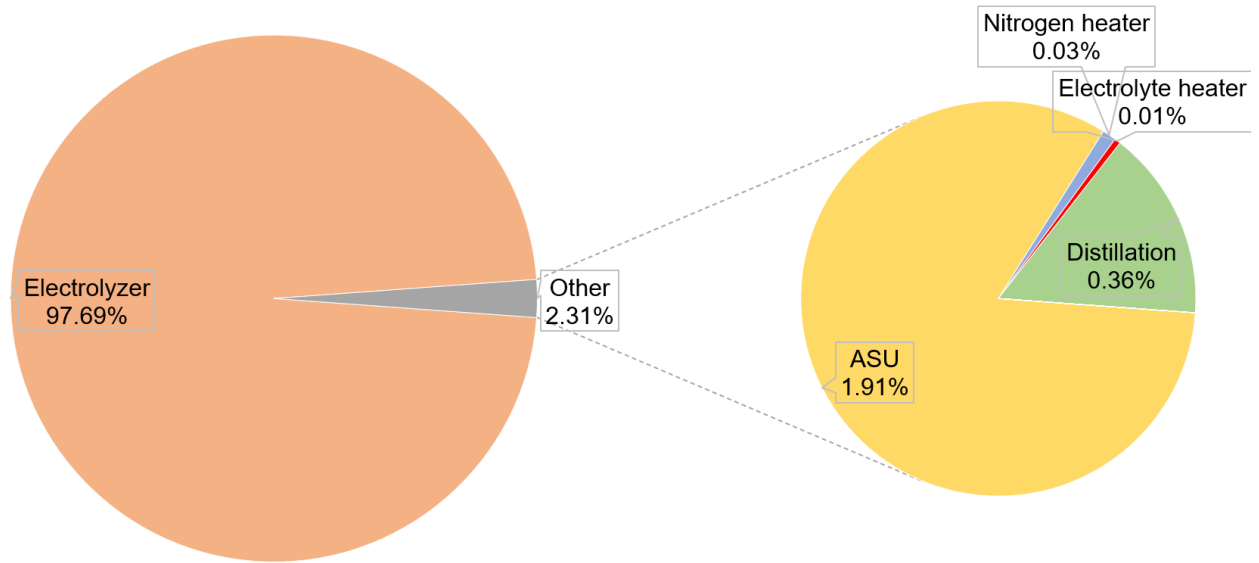
Figure B.7: GDE purge process capital intensity for 2055 t d^{-1}.
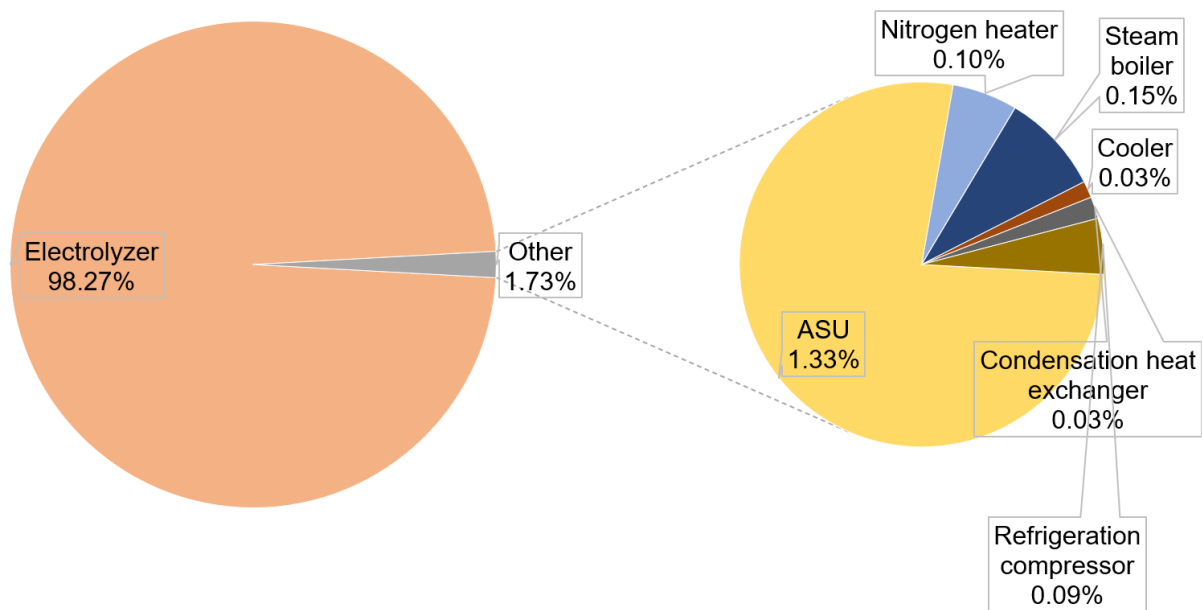
Figure B.8: SOEL process capital intensity for 2055 t d^{-1}.

B.3 Current-Voltage Characteristics
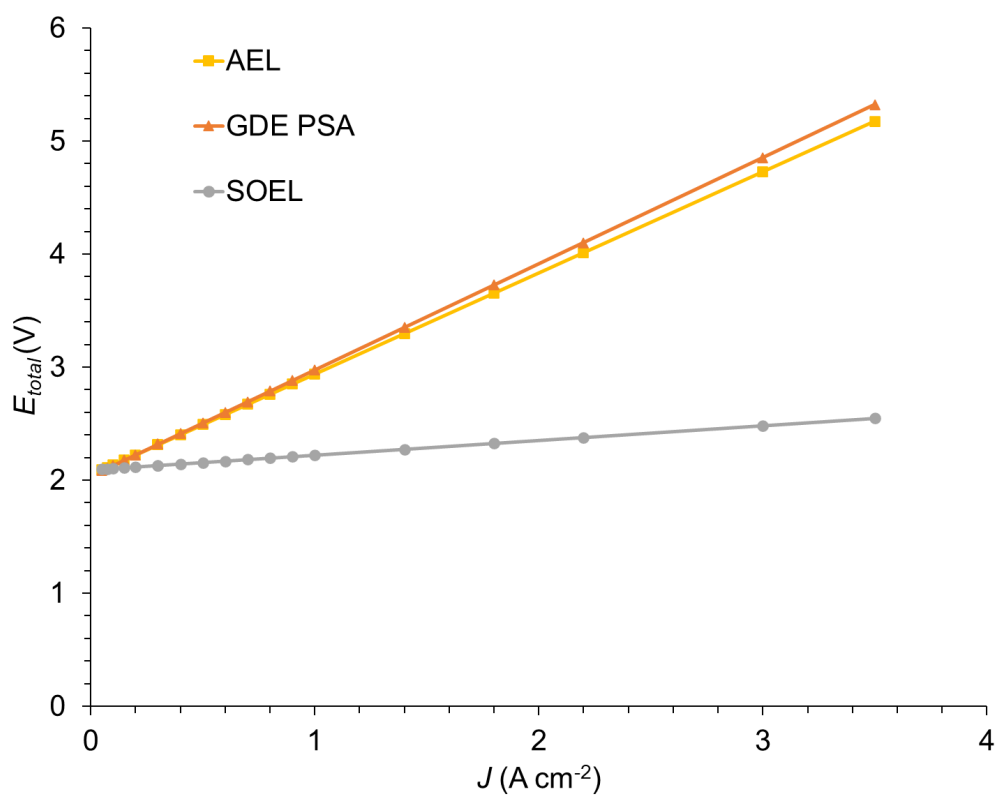
Figure B.9: Current-voltage characteristics of AEL, GDE and SOEL.

C Mass Balances

The following tables show the stream summaries of the presented conceptual processes. The stream-labelled PFD's can be found in Figure 3.8 on page 29.

C.1 AEL process

Table C.3: Mass balance (kg s^{-1}) of the AEL process at 2055 t d^{-1}.

Component	W1	K1	W2	W3	W4	W5	W6	W7	W8	A1	R1	N1	N2	N3	N4	C1	O1
NH3	0.0	0.0	0.0	0.0	0.0	168764.0	168787.9	23.9	23.8	168764.0	0.0	0.0	0.0	0.0	0.0	0.0	0.0
H2O	54.3	0.0	54.3	261.3	261.3	1462596.0	1462541.8	207.2	0.1	1462334.6	207.0	0.0	0.0	0.0	0.0	0.0	0.0
N2	0.0	0.0	0.0	0.0	0.0	0.0	0.0	0.0	0.0	0.0	0.0	280.8	84.3	196.6	196.6	176.9	0.0
H2	0.0	0.0	0.0	0.0	0.0	0.0	0.0	0.0	0.0	0.0	0.0	0.0	0.0	0.0	0.0	1.8	0.0
O2	0.0	0.0	0.0	0.0	0.0	0.0	0.0	0.0	0.0	0.0	0.0	85.3	85.1	0.2	0.2	0.0	48.3
KOH	0.0	0.0	0.0	67.5	67.5	476817.7	476817.7	67.5	0.0	476750.1	67.5	0.0	0.0	0.0	0.0	0.0	0.0
NH3 (inert)	0.0	0.0	0.0	0.1	0.1	0.1	0.1	0.1	0.0	0.0	0.1	0.0	0.0	0.0	0.0	0.0	0.0
TOTAL	54.3	0.0	54.4	329.1	329.1	2108177.8	2108147.5	298.7	24.0	2107848.7	274.8	366.1	169.3	196.8	196.8	178.8	48.3
T (°C)	25.0	25.0	25.0	-10.0	80.0	80.0	80.0	80.0	106.0	80.0	-33.5	25.0	-183.2	-183.2	80.0	80.0	80.0
P (bar)	1.0	1.0	1.0	1.0	1.0	1.0	1.0	1.0	1.0	1.0	1.0	1.0	1.0	1.0	1.0	1.0	1.0

Table C.4: Mass balance (kg s^{-1}) of the AEL process at 544 t d^{-1}.

Component	W1	K1	W2	W3	W4	W5	W6	W7	W8	A1	R1	N1	N2	N3	N4	C1	O1
NH3	0.0	0.0	0.0	0.0	0.0	44675.2	44681.6	6.3	6.3	44675.2	0.0	0.0	0.0	0.0	0.0	0.0	0.0
H2O	14.4	0.0	14.4	69.2	69.2	387178.7	387164.3	54.8	0.0	387109.5	54.8	0.0	0.0	0.0	0.0	0.0	0.0
N2	0.0	0.0	0.0	0.0	0.0	0.0	0.0	0.0	0.0	0.0	0.0	130.1	78.1	52.0	52.0	46.8	0.0
H2	0.0	0.0	0.0	0.0	0.0	0.0	0.0	0.0	0.0	0.0	0.0	0.0	0.0	0.0	0.0	0.5	0.0
O2	0.0	0.0	0.0	0.0	0.0	0.0	0.0	0.0	0.0	0.0	0.0	39.5	39.4	0.1	0.1	0.0	12.8
KOH	0.0	0.0	0.0	17.9	17.9	126223.3	126223.3	17.9	0.0	126205.4	17.9	0.0	0.0	0.0	0.0	0.0	0.0
NH3 (inert)	0.0	0.0	0.0	0.0	0.0	0.0	0.0	0.0	0.0	0.0	0.0	0.0	0.0	0.0	0.0	0.0	0.0
TOTAL	14.4	0.0	14.4	87.1	87.1	558077.2	558069.2	79.1	6.3	557990.1	72.7	169.6	117.5	52.1	52.1	47.3	12.8
T (°C)	25.0	25.0	25.0	-10.0	80.0	80.0	80.0	80.0	106.0	80.0	-33.5	25.0	-183.2	-183.2	80.0	80.0	80.0
P (bar)	1.0	1.0	1.0	1.0	1.0	1.0	1.0	1.0	1.0	1.0	1.0	1.0	1.0	1.0	1.0	1.0	1.0

Table C.5: Mass balance (kg s^{-1}) of the AEL process at 91 t d^{-1}.

Component	W1	K1	W2	W3	W4	W5	W6	W7	W8	A1	R1	N1	N2	N3	N4	C1	O1
NH3	0.0	0.0	0.0	0.0	0.0	7473.2	7474.3	1.1	1.1	7473.2	0.0	0.0	0.0	0.0	0.0	0.0	0.0
H2O	2.4	0.0	2.4	11.6	11.6	64767.0	64764.6	9.2	0.0	64755.4	9.2	0.0	0.0	0.0	0.0	0.0	0.0
N2	0.0	0.0	0.0	0.0	0.0	0.0	0.0	0.0	0.0	0.0	0.0	12.4	3.7	8.7	8.7	7.8	0.0
H2	0.0	0.0	0.0	0.0	0.0	0.0	0.0	0.0	0.0	0.0	0.0	0.0	0.0	0.0	0.0	0.1	0.0
O2	0.0	0.0	0.0	0.0	0.0	0.0	0.0	0.0	0.0	0.0	0.0	3.8	3.8	0.0	0.0	0.0	2.1
KOH	0.0	0.0	0.0	3.0	3.0	21114.6	21114.6	3.0	0.0	21111.6	3.0	0.0	0.0	0.0	0.0	0.0	0.0
NH3 (intert)	0.0	0.0	0.0	0.0	0.0	0.0	0.0	0.0	0.0	0.0	0.0	0.0	0.0	0.0	0.0	0.0	0.0
TOTAL	2.4	0.0	2.4	14.6	14.6	93354.8	93353.5	13.2	1.1	93340.3	12.2	16.2	7.5	8.7	8.7	7.9	2.1
T (°C)	25.0	25.0	25.0	-10.0	80.0	80.0	80.0	80.0	106.0	80.0	-33.5	25.0	-183.2	-183.2	80.0	80.0	80.0
P (bar)	1.0	1.0	1.0	1.0	1.0	1.0	1.0	1.0	1.0	1.0	1.0	1.0	1.0	1.0	1.0	1.0	1.0

C.2 GDE process with H$_2$ Isolation

Table C.6: Mass balance (kg s^{-1}) the of GDE PSA process at 2055 t d^{-1}.

Component	W1	K1	W2	W3	W4	W5	W6	R1	N1	N2	N3	N4	N5	C1	C2	C3	C4	A1	O1
NH3	0.0	0.0	0.0	0.0	0.0	23.9	23.8	0.0	0.0	0.0	0.0	0.0	0.0	0.0	0.0	0.0	0.0	0.0	0.0
H2O	54.2	0.0	54.2	280.5	280.5	226.4	0.1	226.3	0.0	0.0	0.0	0.0	0.0	0.0	0.0	0.0	0.0	0.0	0.0
N2	0.0	0.0	0.0	0.0	0.0	0.0	0.0	0.0	52.2	15.6	36.5	36.5	196.6	176.9	16.9	0.0	16.8	160.1	0.0
H2	0.0	0.0	0.0	0.0	0.0	0.0	0.0	0.0	0.0	0.0	0.0	0.0	17.3	19.1	1.8	1.0	0.8	17.3	0.0
O2	0.0	0.0	0.0	0.0	0.0	0.0	0.0	0.0	15.8	15.8	0.0	0.0	0.0	0.0	0.0	0.0	0.0	0.0	48.1
KOH	0.0	0.0	0.0	82.8	82.8	82.8	0.0	82.7	0.0	0.0	0.0	0.0	0.0	0.0	0.0			0.0	0.0
NH3 inert	0.0	0.0	0.0	0.1	0.1	0.1	0.0	0.1	0.0	0.0	0.0	0.0	0.0	0.0	0.0	0.0	0.0	0.0	0.0
Total	54.2	0.0	54.2	363.4	363.4	333.2	24.0	309.2	68.0	31.4	36.6	36.6	213.9	196.1	18.7	1.0	17.7	177.4	48.1
T (°C)	25.0	25.0	25.0	-10.0	80.0	80.0	106.0	-33.5	25.0	-183.2	-183.2	80.0	80.0	80.0	80.0	25.0	25.0	80.0	80.0
P (bar)	1.0	1.0	1.0	1.0	1.0	1.0	1.0	1.0	1.0	1.0	1.0	1.0	1.0	1.0	1.0	1.0	1.0	1.0	1.0

Table C.7: Mass balance (kg s^{-1}) of the GDE PSA process at 544 t d^{-1}.

Component	W1	K1	W2	W3	W4	W5	W6	R1	N1	N2	N3	N4	N5	C1	C2	C3	C4	A1	O1
NH3	0.0	0.0	0.0	0.0	0.0	6.3	6.3	0.0	0.0	0.0	0.0	0.0	0.0	0.0	0.0	0.0	0.0	0.0	0.0
H2O	14.3	0.0	14.3	74.3	74.3	59.9	0.0	59.9	0.0	0.0	0.0	0.0	0.0	0.0	0.0	0.0	0.0	0.0	0.0
N2	0.0	0.0	0.0	0.0	0.0	0.0	0.0	0.0	24.2	14.5	9.7	9.7	52.0	46.8	4.5	0.0	4.5	42.4	0.0
H2	0.0	0.0	0.0	0.0	0.0	0.0	0.0	0.0	0.0	0.0	0.0	0.0	17.3	5.1	0.5	0.3	0.2	4.6	0.0
O2	0.0	0.0	0.0	0.0	0.0	0.0	0.0	0.0	7.3	7.3	0.0	0.0	0.0	0.0	0.0	0.0	0.0	0.0	12.7
KOH	0.0	0.0	0.0	21.9	21.9	21.9	0.0	21.9	0.0	0.0	0.0	0.0	0.0	0.0	0.0	0.0		0.0	0.0
NH3 inert	0.0	0.0	0.0	0.0	0.0	0.0	0.0	0.0	0.0	0.0	0.0	0.0	0.0	0.0	0.0	0.0	0.0	0.0	0.0
Total	14.3	0.0	14.4	96.2	96.2	88.2	6.3	81.8	31.5	21.8	9.7	9.7	69.3	51.9	5.0	0.3	4.7	47.0	12.7
T (°C)	25.0	25.0	25.0	-10.0	80.0	80.0	106.0	-33.5	25.0	-183.2	-183.2	80.0	80.0	80.0	80.0	25.0	25.0	80.0	80.0
P (bar)	1.0	1.0	1.0	1.0	1.0	1.0	1.0	1.0	1.0	1.0	1.0	1.0	1.0	1.0	1.0	1.0	1.0	1.0	1.0

Table C.8: Mass balance (kg s^{-1}) of the GDE PSA process at 91 t d^{-1}.

Component	W1	K1	W2	W3	W4	W5	W6	R1	N1	N2	N3	N4	N5	C1	C2	C3	C5	A1	O1
NH3	0.0	0.0	0.0	0.0	0.0	1.1	1.1	0.0	0.0	0.0	0.0	0.0	0.0	0.0	0.0	0.0	0.0	0.0	0.0
H2O	2.4	0.0	2.4	12.4	12.4	10.0	0.0	10.0	0.0	0.0	0.0	0.0	0.0	0.0	0.0	0.0	0.0	0.0	0.0
N2	0.0	0.0	0.0	0.0	0.0	0.0	0.0	0.0	2.9	1.3	1.6	1.6	8.7	7.8	0.7	0.0	0.7	7.1	0.0
H2	0.0	0.0	0.0	0.0	0.0	0.0	0.0	0.0	0.0	0.0	0.0	0.0	17.3	0.8	0.1	0.0	0.0	0.8	0.0
O2	0.0	0.0	0.0	0.0	0.0	0.0	0.0	0.0	0.9	0.9	0.0	0.0	0.0	0.0	0.0	0.0	0.0	0.0	2.1
KOH	0.0	0.0	0.0	3.7	3.7	3.7	0.0	3.7	0.0	0.0	0.0	0.0	0.0	0.0	0.0	0.0		0.0	0.0
NH3 inert	0.0	0.0	0.0	0.0	0.0	0.0	0.0	0.0	0.0	0.0	0.0	0.0	0.0	0.0	0.0	0.0	0.0	0.0	0.0
Total	2.4	0.0	2.4	16.1	16.1	14.8	1.1	13.7	3.8	2.2	1.6	1.6	26.0	8.7	0.8	0.0	0.8	7.9	2.1
T (°C)	25.0	25.0	25.0	-10.0	80.0	80.0	106.0	-33.5	25.0	25.0	25.0	80.0	80.0	80.0	25.0	25.0	80.0	80.0	80.0
P (bar)	1.0	1.0	1.0	1.0	1.0	1.0	1.0	1.0	1.0	1.0	1.0	1.0	1.0	1.0	1.0	1.0	1.0	1.0	1.0

C.3   GDE process without H$_2$ Isolation

Table C.9: Mass balance (kg s^{-1}) of the GDE purge process at 2055 t d^{-1}.

Component	W1	K1	W2	W3	W4	W5	W6	R1	N1	N2	N3	N4	C1	O1
NH3	0.0	0.0	0.0	0.0	0.0	23.9	23.8	0.0	0.0	0.0	0.0	0.0	0.0	0.0
H2O	54.2	0.0	54.2	280.5	280.5	226.4	0.1	226.3	0.0	0.0	0.0	0.0	0.0	0.0
N2	0.0	0.0	0.0	0.0	0.0	0.0	0.0	0.0	280.8	84.3	196.6	196.6	176.9	0.0
H2	0.0	0.0	0.0	0.0	0.0	0.0	0.0	0.0	0.0	0.0	0.0	0.0	1.8	0.0
O2	0.0	0.0	0.0	0.0	0.0	0.0	0.0	0.0	85.3	85.1	0.2	0.2	0.2	48.1
KOH	0.0	0.0	0.0	82.8	82.8	82.8	0.0	82.7	0.0	0.0	0.0	0.0	0.0	0.0
NH3 inert	0.0	0.0	0.0	0.1	0.1	0.1	0.0	0.1	0.0	0.0	0.0	0.0	0.0	0.0
Total	54.2	0.0	54.2	363.4	363.4	333.2	24.0	309.2	366.1	169.3	196.8	196.8	179.0	48.1
T (°C)	25.0	25.0	25.0	-10.0	80.0	80.0	106.0	-33.5	25.0	-183.2	-183.2	80.0	80.0	80.0
P (bar)	1.0	1.0	1.0	1.0	1.0	1.0	1.0	1.0	1.0	1.0	1.0	1.0	1.0	1.0

Table C.10: Mass balance (kg s^{-1}) of the GDE purge process at 544 t d^{-1}.

Component	W1	K1	W2	W3	W4	W5	W6	R1	N1	N2	N3	N4	C1	O1
NH3	0.0	0.0	0.0	0.0	0.0	6.3	6.3	0.0	0.0	0.0	0.0	0.0	0.0	0.0
H2O	14.3	0.0	14.3	74.3	74.3	59.9	0.0	59.9	0.0	0.0	0.0	0.0	0.0	0.0
N2	0.0	0.0	0.0	0.0	0.0	0.0	0.0	0.0	74.3	22.3	52.0	52.0	46.8	0.0
H2	0.0	0.0	0.0	0.0	0.0	0.0	0.0	0.0	0.0	0.0	0.0	0.0	0.5	0.0
O2	0.0	0.0	0.0	0.0	0.0	0.0	0.0	0.0	22.6	22.5	0.1	0.1	0.1	12.7
KOH	0.0	0.0	0.0	21.9	21.9	21.9	0.0	21.9	0.0	0.0	0.0	0.0	0.0	0.0
NH3 inert	0.0	0.0	0.0	0.0	0.0	0.0	0.0	0.0	0.0	0.0	0.0	0.0	0.0	0.0
Total	14.3	0.0	14.4	96.2	96.2	88.2	6.3	81.9	96.9	44.8	52.1	52.1	47.4	12.7
T (°C)	25.0	25.0	25.0	-10.0	80.0	80.0	106.0	-33.5	25.0	-183.2	-183.2	80.0	80.0	80.0
P (bar)	1.0	1.0	1.0	1.0	1.0	1.0	1.0	1.0	1.0	1.0	1.0	1.0	1.0	1.0

Table C.11: Mass balance (kg s^{-1}) of the GDE purge process at 91 t d^{-1}.

Component	W1	K1	W2	W3	W4	W5	W6	R1	N1	N2	N3	N4	C1	O1
NH3	0.0	0.0	0.0	0.0	0.0	1.1	1.1	0.0	0.0	0.0	0.0	0.0	0.0	0.0
H2O	2.4	0.0	2.4	12.4	12.4	10.0	0.0	10.0	0.0	0.0	0.0	0.0	0.0	0.0
N2	0.0	0.0	0.0	0.0	0.0	0.0	0.0	0.0	15.8	7.1	8.7	8.7	7.8	0.0
H2	0.0	0.0	0.0	0.0	0.0	0.0	0.0	0.0	0.0	0.0	0.0	0.0	0.1	0.0
O2	0.0	0.0	0.0	0.0	0.0	0.0	0.0	0.0	4.8	4.8	0.0	0.0	0.0	2.1
KOH	0.0	0.0	0.0	3.7	3.7	3.7	0.0	3.7	0.0	0.0	0.0	0.0	0.0	0.0
NH3 inert	0.0	0.0	0.0	0.0	0.0	0.0	0.0	0.0	0.0	0.0	0.0	0.0	0.0	0.0
Total	2.4	0.0	2.4	16.1	16.1	14.8	1.1	13.7	20.6	11.9	8.7	8.7	7.9	2.1
T (°C)	25.0	25.0	25.0	-10.0	80.0	80.0	106.0	-33.5	25.0	-183.2	-183.2	80.0	80.0	80.0
P (bar)	1.0	1.0	1.0	1.0	1.0	1.0	1.0	1.0	1.0	1.0	1.0	1.0	1.0	1.0

C.4 SOEL process

Table C.12: Mass balance (kg s^{-1}) of the SOEL process at 2055 t d^{-1}.

Component	W1	W2	N1	N2	N3	N4	C1	C2	C3	C4	C5	O1
NH3	0.0	0.0	0.0	0.0	0.0	0.0	28.8	25.9	25.9	2.1	23.8	0.0
H2O	65.2	65.2	0.0	0.0	0.0	0.0	0.0	0.0	0.0	0.0	0.0	0.0
N2	0.0	0.0	338.0	101.4	236.6	236.6	212.9	215.3	215.3	215.2	0.1	0.0
H2	0.0	0.0	0.0	0.0	0.0	0.0	2.2	2.7	2.7	2.7	0.0	0.0
O2	0.0	0.0	102.6	102.4	0.3	0.3	0.3	0.3	0.3	0.1	0.1	57.9
Total	65.2	65.2	440.6	203.8	236.9	236.9	244.2	244.2	244.2	220.2	24.0	57.9
T (°C)	25.0	550.0	25.0	-183.2	-183.2	550.0	550.0	550.0	300.0	-92.0	-92.0	550.0
P (bar)	1.0	1.0	1.0	1.0	1.0	1.0	1.0	1.0	1.0	1.0	1.0	1.0

Table C.13: Mass balance (kg s^{-1}) of the SOEL process at 544 t d^{-1}.

Component	W1	W2	N1	N2	N3	N4	C1	C2	C3	C4	C5	O1
NH3	0.0	0.0	0.0	0.0	0.0	0.0	7.6	6.9	6.9	0.6	6.3	0.0
H2O	17.3	17.3	0.0	0.0	0.0	0.0	0.0	0.0	0.0	0.0	0.0	0.0
N2	0.0	0.0	89.5	26.8	62.6	62.6	56.4	57.0	57.0	57.0	0.0	0.0
H2	0.0	0.0	0.0	0.0	0.0	0.0	0.6	0.7	0.7	0.7	0.0	0.0
O2	0.0	0.0	27.2	27.1	0.1	0.1	0.1	0.1	0.1	0.0	0.0	15.3
Total	17.3	17.3	116.6	53.9	62.7	62.7	64.6	64.6	64.6	58.3	6.4	15.3
T (°C)	25.0	550.0	25.0	-183.2	-183.2	550.0	550.0	550.0	300.0	-92.0	-92.0	550.0
P (bar)	1.0	1.0	1.0	1.0	1.0	1.0	1.0	1.0	1.0	1.0	1.0	1.0

Table C.14: Mass balance (kg s^{-1}) of the SOEL process at 91 t d^{-1}.

Component	W1	W2	N1	N2	N3	N4	C1	C2	C3	C4	C5	O1
NH3	0.0	0.0	0.0	0.0	0.0	0.0	1.3	1.1	1.1	0.1	1.1	0.0
H2O	2.9	2.9	0.0	0.0	0.0	0.0	0.0	0.0	0.0	0.0	0.0	0.0
N2	0.0	0.0	26.2	15.7	10.5	10.5	9.4	9.5	9.5	9.5	0.0	0.0
H2	0.0	0.0	0.0	0.0	0.0	0.0	0.1	0.1	0.1	0.1	0.0	0.0
O2	0.0	0.0	8.0	7.9	0.0	0.0	0.0	0.0	0.0	0.0	0.0	2.6
Total	2.9	2.9	34.1	23.7	10.5	10.5	10.8	10.8	10.8	9.7	1.1	2.6
T (°C)	25.0	550.0	25.0	-183.2	-183.2	550.0	550.0	550.0	300.0	-92.0	-92.0	550.0
P (bar)	1.0	1.0	1.0	1.0	1.0	1.0	1.0	1.0	1.0	1.0	1.0	1.0